Electron Dynamics of TiN Thin Films and InGaN/GaN Dot-in-Nanowires

by

Heather J. George

A dissertation submitted in partial fulfillment
of the requirements for the degree of
Doctor of Philosophy
(Electrical Engineering)
in the University of Michigan
2018

Doctoral Committee:

Professor Ted Norris, Chair
Professor Parag Deotare
Professor Zetian Mi
Professor Max Shtein

Heather J. George
hthrfrg@umich.edu
ORCID iD: 0000-0001-7974-1917

ACKNOWLEDGEMENTS

My PhD experience at the University of Michigan has had many wonderful and challenging aspects. To those who have played a role in my time here, I thank you.

To begin, I would like to thank my advisor, Professor Ted Norris, for giving me the opportunity to complete this work. I am continually impressed by his approach to science; a mix of creative thinking and rigorous application. He works tirelessly to support his students; I appreciate the time that he has given to discussions and feedback. He gave me the freedom to make choices in the lab and make mistakes which have taught me more than just following a standard process. I would also like to thank the other members of my committee who have read this thesis and attended my defense: Dr. Mi, Dr. Deotare, and Dr. Shtein. They have taken time to discuss my work and ask about my plans and ambitions.

I would like to acknowledge my wonderful collaborators in the TiN project, the Shalaev and Boltasseva groups at Purdue University. Nathaniel Kinsey, who is now at Virginia Commonwealth University, grew the samples and has spent countless hours in discussion about the results. He did some initial characterization, including the ellipsometry used to extract the dielectric functions. He was the one who put the COMSOL model together and made the connection that the long lifetime in the differential transmission was heat transfer to the substrate. He also gave me his Matlab code for an initial two temperature model that was the starting point of the model for this work. Nathaniel is an all-around great guy; I appreciate his understanding of fundamental science and kind sincerity as a person.

My collaborators in the InGaN project were Dr. Mi and Dr. Ra; I am very grateful for the opportunity to be part of such an exciting project. Dr. Ra worked tirelessly to create good samples under the specifications that we requested for our experiment. This was not an easy task and I appreciate the time and skill that he devoted to it. He also performed the photoluminescence tests with a continuous wave excitation shown in this thesis.

My groupmates have also been a source of experience, knowledge, and encourage-

ment during my time in graduate school. Miao-Bin and You-Chia, I thank you for the time that you spent teaching me in the lab and for our conversations in the office. Jessica and Nooshin, I appreciate the help with random projects and the discussions over lunch or coffee. Moussa, having a conversation with you always made my day better and I wish you lots of luck at RPI. Zhen, I have enjoyed the experiments that we have done together and I hope that you have many exciting discoveries as you continue the InGaN work. When the laser in our lab was down, I appreciate Dr. Merlin allowing me to work in his lab; Meredith and Ibrahim graciously gave me space and laser time. Other people at the Engineering Research Building played a part in the successful completion of this work. Car Nosel, John Nees, and Steve Katnik provided me help when I needed it, and I appreciate each of you.

I would like to thank the cohort of friends who supported me during this time. Brandon and Cameron, you both helped me survive that first year, and I am grateful. Brandon, I appreciate you helping to keep me sane when it felt like things werent working. Liz, I admire your tenacity and start-up attitude; thank you for our writing sessions and your encouraging texts. Christina, our friendship and workouts made me a happier healthier person all-around; thanks for also being a great roommate. Nancy, we met the first day of graduate school and our friendship is the best thing that came out of quantum mechanics for me; you have continued to encourage me in all areas of my life. Jess, you are a constant and loving friend. Deanna, Joe, Chris, Ethan, and other GCF friends, thank you for good conversations and genuine friendships.

Finally, I would like to thank my family and husband, Bill. You have made me who I am, and this would not have been possible without your love, encouragement, and support.

TABLE OF CONTENTS

LIST OF FIGURES

FIGURE

LIST OF TABLES

TABLE

ABSTRACT

The invention of ultrafast lasers revolutionized our capacity to examine the fundamental physics of the materials used in optoelectronics on a femtosecond timescale. Pump-probe is a powerful optical technique which measures the changes in the absorption; the transient data can inform the theory of carrier-carrier scattering, phonon interaction, and state lifetimes in the sample. This work explores the ultrafast electron dynamics of two materials of emerging importance to optoelectronics: Titanium Nitride (TiN) and InGaN dot-in-nanowire structures.

TiN is a refractory conductive ceramic that has many uses in plasmonics, CMOS electronics, and hot carrier devices. Its optical properties as revealed by ellipsometry are very similar to those of noble metals, which are the most important traditional plasmonic materials; however, its thermal properties and electron-phonon coupling are quite different. Using pump-probe experiments, the transient carrier dynamics are explored. The results are interpreted using a two temperature model which reveals important contrasts to the noble metals; in particular, the electron-phonon coupling constant is on the order of 10^{18}, which approximately two orders of magnitude greater than the coupling in gold. This is significant because heat is efficiently transferred to the substrate, leading to a large substrate contribution to the measured signal.

Selective area samples of InGaN/GaN dot-in-nanowires grown on GaN/sapphire were investigated. This work shows the first time-resolved differential reflection measurements on *green InGaN/GaN quantum dots.* This type of growth is very controlled

and slow compared to self-assembled structures, but this also allows the wires to be more homogenous. Even with this type of growth, defects and trap states play a major role in determining the performance of optoelectronic devices such as LEDs, lasers, and detectors. The lifetimes captured give an understanding of the states in the interaction, as well as energy loss to phonons. Two decay times were extracted; a fast decay 20-35 ps, which is attributed to decay into non-radiative states and a slower decay 330-830 ps, which we believe is mostly radiative recombination. This work can inform future growth and optimization for nanowire LED and laser applications.

CHAPTER I

Introduction to electron relaxation in metals and semiconductors

Advances in understanding the physics of materials continue to revolutionize the world of electronics. Controlling the flow of carriers, understanding the lifetime of their current state, and predicting the probability of their available transitions are all vital parts of engineering opto-electronic devices, including semiconductor lasers, light-emitting diodes (LEDs), and solar cells. While it is easy to characterize the flow of electrons through a metal wire in the presence of an electric field, the problem becomes infinitely more complex as we move past the Drude model into more complex materials, including conducting nitrides and semiconductor heterostructures.

1.1 Carrier experiments

There are several different types of experiments that give information about the movement of carriers in a material. In the simplest Drude model, the carriers are free electrons. In semiconductors, the carriers can be electrons or holes; if it is an intrinsic semiconductor, then the number of holes and electrons is balanced, while a doped semiconductor will have a majority and minority carrier population. Each of the measurements described below gives slightly different information about the system,

which can include information such as carrier mobility, electron- phonon coupling, and carrier- carrier scattering.

Hall measurements, which even predate the discovery of the electron, are one of the most ubiquitous carrier measurements for both metals and semiconductors. By applying a voltage in one direction, and applying a perpendicular magnetic field, the resulting potential created in the direction orthogonal to those axes can be measured. The measured potential can give insight into carrier concentration and is proportional to mobility.

A Haynes- Shockley experiment was the first to show the mobility of the minority carrier. An external bias is applied to the semiconductor, then a pulse is sent in and the carriers are detected at a set distance; from this measurement the drift velocity can be calculated. Both optical and electrical set-ups have been used to study carrier diffusion, mobility and recombination lifetimes.

Pump- probe experiments do not directly measure the presence of carriers, instead the change in transmission (or reflection) due to a change in the carrier distribution induced by a pump pulse is measured. However, if the proper wavelengths are chosen, and knowledge of the system is used, the change in transmission $\Delta T/T$ ($\Delta R/R$)can be related to the dynamics of the carriers. This class of experiments has a lot of advantages; since it is all optical it can measure the intrinsic value of a material constant that is not hindered by other imperfect physical interfaces, such as the connection of electrodes to the material in a Hall measurement. Also, since the measurement is an interaction of two light pulses, the temporal resolution is only limited by the convolution of the pump and probe pulse widths, allowing for measurements not possible with comparatively slow electronics.

1.2 Pump-probe experiments

There are many variations of pump-probe experiments, but the common factor is that a pump is used to perturb the system, while a weak probe then samples the change in transmission (or reflection) made by the pump. In order to only measure the change in the system due to the pump, the pump beam is chopped and phased to a lock-in amplifier; however, the pump itself is not measured; the lock-in is connected to a photodetector which only measures the modulation the probe pulse. The pump pulse is blocked from entering the detector after interacting with the sample by some combination of filtering, including polarization, spectral, and spatial. These can be setup to measure the differential reflection, $\Delta R/R$, or the differential transmission, $\Delta T/T$. Since the light must either be reflected, transmitted or absorbed, the change in reflection or transmission signifies a change in the absorption.

1.3 Relaxation in metals

Even though the noble metals are the closest materials to a simple free electron model, it has taken a considerable amount of work to understand the electron dynamics[1,27–31]. In a linear isotropic material, the dielectric displacement field ($\mathbf{D}$) is proportional to the electric field ($\mathbf{E}$) through the equation:

$$\mathbf{D} = \epsilon_{\mathbf{0}}\epsilon\mathbf{E} \tag{1.1}$$

where $\epsilon = \epsilon_1 + i\epsilon_2$ is the complex permittivity of the material. The differential reflection can be related to a change in the permittivity through[31]:

$$\frac{\Delta R}{R} = \frac{1}{R}\Big[\frac{\partial R}{\partial \epsilon_1}\Delta\epsilon_1 + \frac{\partial R}{\partial \epsilon_2}\Delta\epsilon_2\Big] \tag{1.2}$$

For excitation from ultrafast pulses, there are several processes that take place on a very short timescale. They are summarized in Figure 1.1.

First the available conduction electrons absorb the energy from the incoming photons; in this state they are in a non-thermal distribution and do not have a defined temperature. This thermalization process has a timescale that is not currently resolved by transient pump-probe experiments. The second timescale is when the non-thermal electrons undergo electron-electron scattering to reach a state of equilibrium. These are labelled "hot electrons". These thermalized electrons are very energetic and have the ability to do work; the applications of hot electrons will be discussed in Chapter 2. During the initial two steps, the lattice has not absorbed any energy. The third timescale is when electron- phonon scattering brings the hot electrons and the lattice into equilibrium.

In the introduction to solid state physics, the idea is introduced that for a Fermi gas (or ideal metal) at T= 0 K, the occupancy probability $f(E)$ will be a step function: $f(E) = 1$ if $E \leq E_F$ or 0 if $E > E_F$. As the material is heated, this step function turns into a Fermi-Dirac distribution around E_F as some of the electrons below the fermi energy (E_F) get excited above E_F by the heat of the lattice. In this same way, the heat introduced by the laser pulse, will change the occupancy probability, $f(E)$, which will change the reflection of the metal; this is called Fermi smearing.

The reflection can also be changed by strain that is introduced to the metal as the lattice expands due to heating. Since this is a lattice effect, it is often ignored for transient pump-probe experiments of metals. The noble metals relax on a timescale of <5 ps, which is faster than the typical response of the lattice. However, for other more complex metals, such as the transition metal platinum, the lattice cannot be ignored[32].

In Chapter 2, titanium nitride (TiN) will be discussed as a material with great potential uses in optoelectronics. However, its electronic structure is very complex

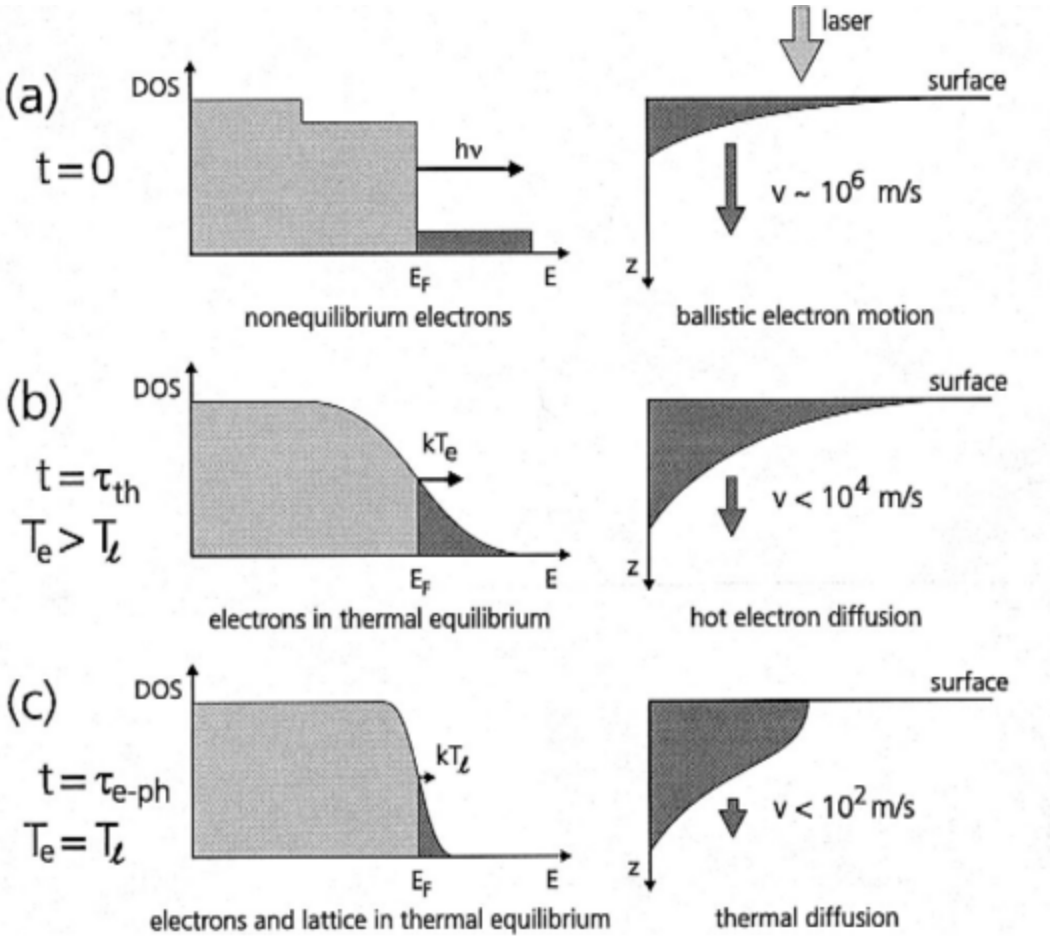

Figure 1.1: The three phases of electron relaxation in metals. (a)The electrons absorb the photons in the excitation pulse creating electrons in non-equilibrium state. (b)Through electron-electron scattering, the hot electrons come to an equilibrium within themselves at T_e. (c) The third phase shows electrons coming into equilibrium with the lattice through electron-phonon coupling[1].

and cannot be modeled with the simple free electron model. Despite that, it has a complex dielectric function which is very similar to gold. Due to the fact that gold has been the subject of many of these pump-probe experiments, it makes a good reference point.

The response described so far, is for the phonon assisted intraband relaxation, also described as the being in the "Drude tail", since this is the response expected for Drude metals. However, at higher excitation energies, interband transitions begin to occur; in gold these transitions start at around 1.8 eV[6]. These transitions do not

occur at the gamma point, so they are not radiative like traditional semiconductors. However, the other aspects of the interband relaxation will follow the same processes as electron relaxation in semiconductors, which will be discussed in the next section.

1.4 Relaxation in semiconductors

The initial response of semiconductors to an excitation by an ultrafast pulse is similar to metals. The electrons absorb the energy and are excited to a higher state where they are in a nonthermal distribution. This all occurs on the timescale of <200 fs. Carrier-carrier scattering and carrier-phonon interactions begin around 100 fs and continue to the ps timescale. Radiative and non-radiative recombination processes begin around a ps and can last for μs timescales[22].

The key difference is the radiative and non-radiative processes which are on a significantly longer timescale than intraband responses in metals; heat dissipation through the lattice can be on a longer timescale, but at that time, the energy has already transferred from the carriers. Not surprisingly, this goes back to the difference in the band structures when comparing a metal and a semiconductor. A metal will have a conduction band that crosses the Fermi level, while a semiconductor has a gap that spans the Fermi energy.

The semiconductor bandstructure for a typical direct bandgap material can be seen in Figure 1.2, which shows a pump-probe experiment examining the lifetimes of different states. Three different valence subbands are shown, the heavy-hole (HH), light-hole and the split-off-hole (SO). The pump (red arrow) is energetic enough to excite carriers across the bandgap. The probe wavelength (blue arrow) will determine which transitions are measured. The three regimes of interest are pictured: Photoexcitation, thermalization, and recombination. Pump-probe measurements give insight on the physics occurring in the thermalization and recombination regimes. Radiative and non-radiative processes, which determine the efficiency of solid-state devices, e.g.

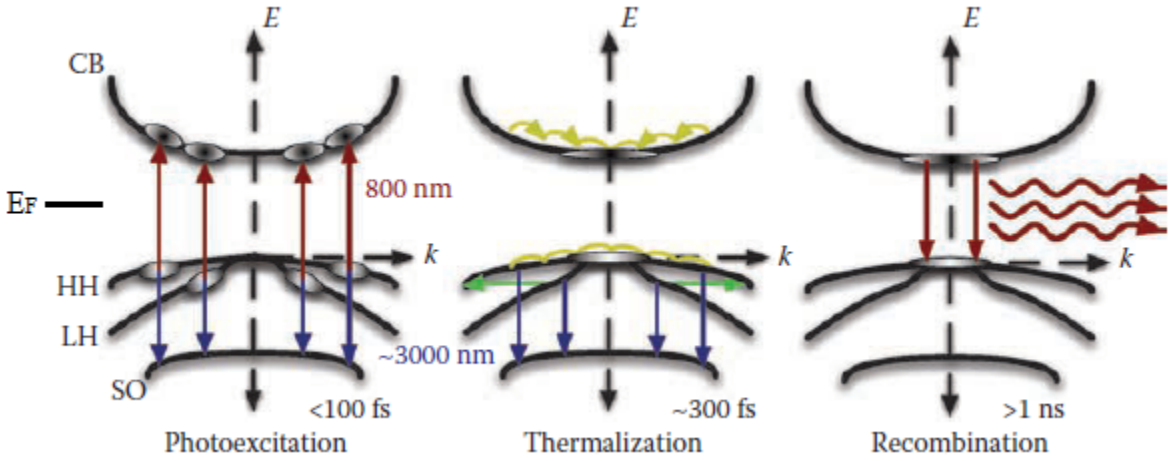

Figure 1.2: Optical pump, mid-infrared probe measurements on a III–V semiconductor (left). The mid-infrared probe pulse is used to isolate the hole subband dynamics from the conduction band dynamics. Initial photoexcitation is determined by the photon energies present in the pump pulse (red). Mid-infrared probe pulses (blue) promote holes from the upper valance subbands to the split-off subband. The wavelength of this probe pulse determines the region in k-space probed in this experiment. (middle) Energy thermalization is the result of interand intrasubband carrier–carrier scattering (yellow) and phonon scattering between subbands (green). (right) The system returns to equilibrium using electron–hole recombination, which results in the emission of a photon (red), carrier trapping (not shown), or thermal diffusion to the substrate (not shown). CB, conduction band; HH, heavy-hole subband; LH, light-hole subband; and SO, split-off–hole subband.[2].

light-emitting diodes, will be discussed in more detail in Chapter 4.

1.5 Summary of chapters

In **Chapter 2** the background and motivation of studying TiN is presented. In its traditional definition it is a ceramic, however TiN is conducting and has some optical properties that mimic that of a Drude metal which make it an attractive plasmonic material. From the bandstructure, it appears metallic, but it also has nearby bands at the gamma point which makes it appear semiconductor-like. Growth parameters and their effect on the dielectric permittivity will be discussed.

In **Chapter 3** results from time resolved pump-probe experiments are discussed.

The lifetimes, which are very different than that of a Drude metal, are examined in relationship to the traditional Two Temperature Model. The electron-phonon coupling constant, G, that is used to characterize electron relaxation in metals will be discussed and calculated from material parameters.

In **Chapter 4** the background and motivation of InGaN/GaN heterostructures in solid state lighting technologies is presented. The basic processes governing the efficiency of light-emitting diodes are discussed. The properties of selective-area growth dot- in- nanowire structures are discussed, as these samples are the focus of the optical measurements in Chapters 5 and 6.

In **Chapter 5** the photoluminescence (PL) of two InGaN/GaN nanowire samples are presented. The PL from a pulsed excitation source is compared to that from a continuous wave (CW) laser. This comparison gives insight into the states and composition of the two samples. One sample is a white light nanowire sample, and the other is a green dot-in-nanowire sample.

In **Chapter 6** transient pump-probe measurements are presented for the two InGaN/GaN nanowire samples. The carrier dynamics including, electron capture and relaxation lifetimes are discussed. Fast capture and short lifetimes in the white light nanowire sample indicates that this sample has localized states due to defects. The green dot-in-nanowire sample has longer capture times and lifetimes. These samples are compared with values from current literature.

In **Chapter 7** the work presented is summarized and future work for each project is discussed.

CHAPTER II

TiN background

From Chapter 1, we can see that the fundamental processes underlying many electronic and optoelectronic devices are governed by the presence of hot carriers and their relaxation. As a result, relaxation processes in many metal and semiconductor structures are now understood in great detail. A particular class of materials of great emerging interest is the transition metal nitrides such as TiN, ZrN, and HfN, which exhibit promise for applications in refractory plasmonics, hot carrier driven devices, and thermal applications.

2.1 Motivation

2.1.1 Plasmonics

The study of the interaction between electromagnetic waves and the free electrons in a metal is the field of plasmonics. Due to the fact that metals do not propagate light, this interaction is only seen at the dielectric/metal interface. The first type of plasmonic interaction is a propagating wave on the surface of the metal/dielectric interface called a surface plasmon polariton (SPP). When an electromagnetic wave travels along the interface between a dielectric and a metal, information can be carried at the speed of light in the material while being confined to an area that is much smaller than the conventional optical fiber. Surface plasmons are touted as a way

to marry the speed of optical communication with the size scalability of electronic devices. However, due to loss caused by the metal, plasmonic waves are a decaying exponential that can only propagate over short distances, usually hundreds of microns. Another obstacle is that there is an inherent tradeoff between the confinement of the field and the propagation length of the SPP. Despite these difficulties, efforts continue to create a viable plasmonic waveguides and other optical on-chip communication devices[33–40].

The second type of plasmonic interaction is a localized surface plasmon (LSP). This interaction occurs when the metallic structure has dimensions on the order of the wavelength used for excitation. The size of the particle and the surrounding dielectric will determine its localized surface plasmon resonance (LSPR). Like the SPP, there is strong field confinement at the surface which can be exploited for many applications, including surface-enhanced Raman scattering (SERS), non-diffraction limited waveguides, information storage, optical switches, photocatalysis, and high resolution microscopy[33,41–45].

Another area of applied plasmonics is metamaterials, a class of "materials" that are designed as hybrid structures that often include layers or patterns that can control the absorption, reflection, and propagation of the light. These structures have components which have at least one dimension that is on the order of a wavelength, so the light interacts with the structure as a whole. Instead of being characterized by their bulk properties, they are characterized by effective constants, such as an effective refractive index that is dependent on the complex permittivities of the individual component materials, their respective volume ratio, and the shape of the structure. Figure 2.1 shows several metamaterial structures made of gold and silver, including a planar structure in the bottom right which has a negative index of refraction. In order to have complete design control in creating metamaterials, there must be materials used in the construction that have both positive and negative real components

of the permittivity, ϵ_1. Otherwise, the index of refraction could only be tuned within the range of the individual positive indices. $\epsilon < 0$ and $\mu < 0$ is sufficient to produce a negative index of refraction[46]. Gold and silver are often used as the component material that has a negative real permittivity ϵ_1, because they also have a relatively low ϵ_2 which is directly related to the loss.

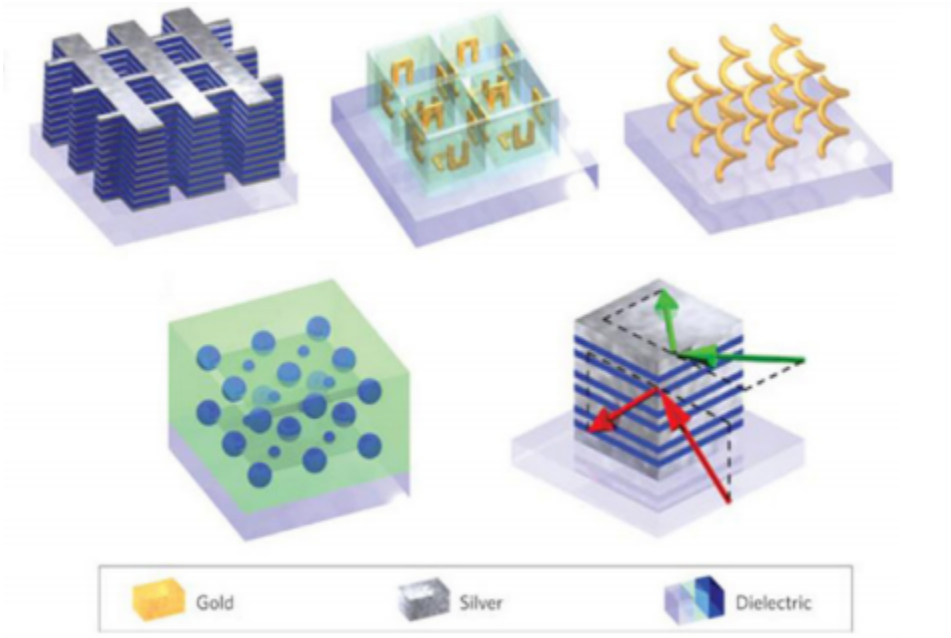

Figure 2.1: Modern metamaterial structures at optical frequencies, based on different materials and geometries. Typical examples include, from top left clockwise, a layered fishnet negative-index metamaterial; 3D arrangement of split-ring resonators; spiral-based chiral metamaterial; metal-dielectric layered metamaterial; metal–dielectric layered metamaterial composed of coupled plasmonic waveguides, enabling angle-independent negative n for particular frequencies[3].

2.1.2 Refractory plasmonics

Under the right growth conditions, the complex dielectric function of TiN mimics that of gold. While it still has the same issues with resistive losses, it is refractory which means that it is chemically stable at very high temperatures; the melting temperature of bulk TiN is 2950 °C. The noble metals, gold and silver, have melting points of 1064 °C and 962 °C, respectively. This is important for several reasons.

First, the loss in the plasmonic system is ohmic loss, which becomes residual heat in the metal of the system, so heat is an inherent part of the interaction. Second, many plasmonic systems are predicated on the size of the material, and as the structures get smaller the melting point also decreases. LSPR requires particles and patterns with dimensions on the order of a wavelength. Gold nanoparticles with a diameter of 38nm on the major axis were shown to melt and change shape at a temperature of 940 °C[47].

Since the shape of these systems plays a vital role in the light interaction, whether it is nanoparticles or patterns, melting will create a catastrophic failure of the device. TiN and gold were patterned to be used as a solar absorber, and TiN was able to withstand more than twice the intensity of the gold pattern[48]. Ultimately, a relatively higher damage threshold for these systems is very beneficial.

2.1.3 Hot carrier driven devices

In Chapter 1 the process of absorbing light in a metal, and the creation of hot electrons was described. Figure 2.2 shows the different effects of hot electrons in a metal, which can each be harnessed for different applications. Plasmonic hot carrier devices have many exciting applications including, catalysis, photothermal cancer treatment, photodetectors, and photovoltaics[4,49–51]. TiN, and other transitional metal nitrides have been proposed as the hot carrier absorbers in a hot carrier solar cell device[52,53]; using a metal-insulator-metal configuration, the photocurrent with TiN was an order of magnitude greater than that of the same device using gold. Gold is used as a plasmonic localized heat source for biological applications, however for most of the visible and NIR wavelengths, TiN shows a greater heating efficiency when compared to gold[54]. TiN has been demonstrated as an absorber and localized heat source for a thermophotovoltaic device[48]. In these experiments TiN was fabricated as a thin film, nanoparticles, and a patterned surface, respectively. Many of the plasmonic

applications use shape and size to control the field, so it is key that TiN is a cheap material that can be made into nanoparticles as well as patterned surfaces. While each of these applications uses hot carriers, Chapter 3 will show how the extremely strong electron-phonon coupling in TiN indicates that the increased efficiency is not because the carriers have longer lifetimes that in noble metals.

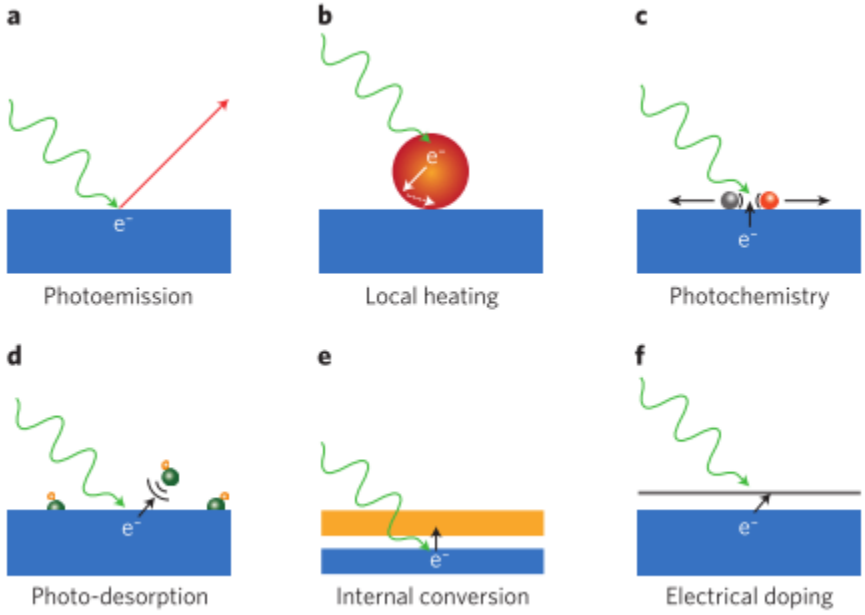

Figure 2.2: Effects that can be stimulated by the photoexcitation of hot electrons in a metal (blue). a, Photoemission of electrons from a metal surface into vacuum can occur when the electron energy exceeds the metal's work function. b, Photoexcited hot electrons can remain trapped inside a metallic nanostructure and cause local heating of a metal particle (red) and its surroundings. c, Hot electrons can interact with molecules on a surface and induce photochemistry. d, The energy of hot electrons can be used to photo-desorb small molecules from the surface. e, Photoejected electrons from a metal can be captured by a counter-electrode (orange) to generate useful current. f, Photoejected electrons can be captured by an ultrathin semiconductor layer or two-dimensional materials (grey) and electrically dope them. light[4]

2.2 TiN samples

TiN is not common in the natural world, but was developed along with other transition metal nitrides and carbides for their refractory properties, high hardness,

and chemical stability. Groups VI, V, and VI of the transition metals are the group of metals with a large enough atomic radius to form interstitial nitride compounds; these should not be confused with what are often referred to as III- V semiconductors whose label comes from the number of electrons the original elements have in their valence shell, not their group number on the periodic table. Of the interstitial nitride compounds, the refractory compounds are TiN, VN, ZrN, NbN, HfN, and TaN[55]. The periodic table shows these transition metals outlined in Figure 2.3.

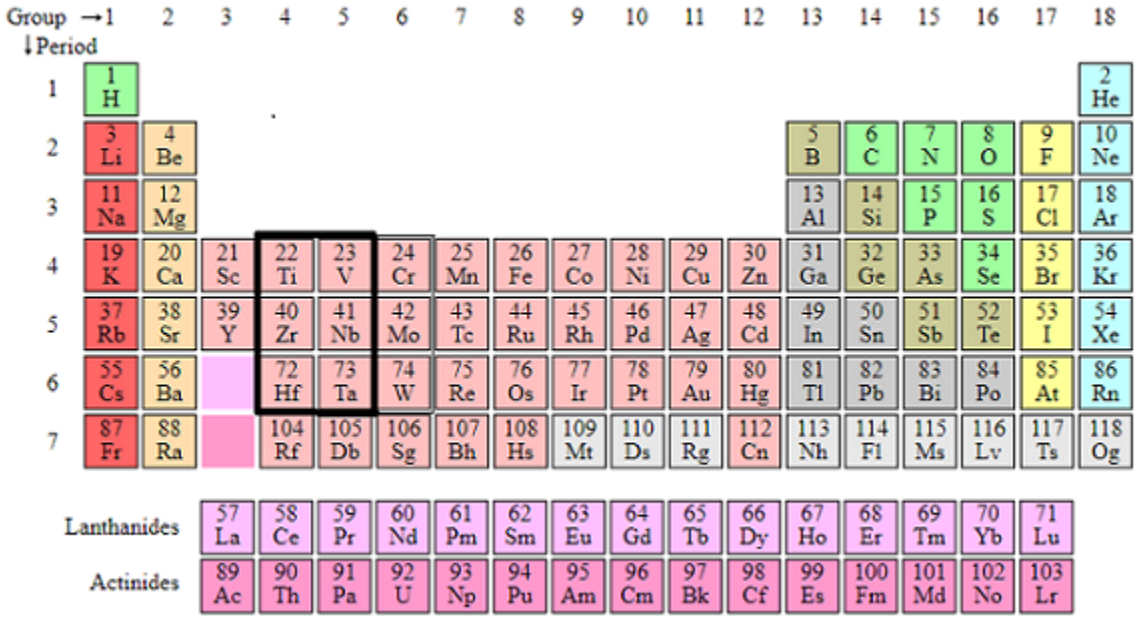

Figure 2.3: Periodic table with the transition metals that form interstitial nitride compounds outlined in red and the transition metals that form refractory nitrides outlined in bold black.

2.2.1 Growth

The samples characterized in this work are two 30nm thick TiN films: a "High Quality" epitaxial film grown at 800 ° C on c-plane sapphire, and a "Low Qualit" polycrystalline film grown at 350 ° C on fused silica. The films were deposited using magnetron sputtering by collaborators at Purdue University. They have been labeled as high quality and low quality partially due to the difference in the grain sizes and

their orientation, as can be seen in Figure 2.4. From the picture, it is not surprising that the low quality film is polycrystalline; the claim that the high quality film is epitaxial is based on previous work from the Purdue group that showed epitaxial TiN films grew on sapphire due to improved lattice matching[56]. The description of epitaxial growth is only referring to the orientation of the grains with the sapphire substrate and is not a claim on grain size or number of grains. It is obvious that both of these thin films are comprised of numerous grains, as opposed to what is normally thought of for a crystalline structure. The difference in the films is due to both the difference in temperature deposition and the choice of substrate.

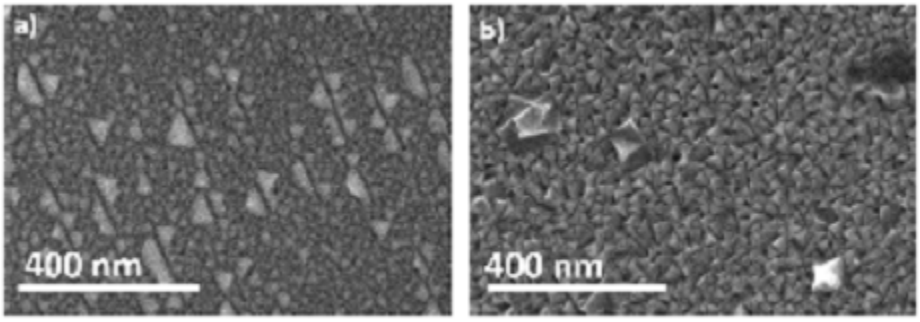

Figure 2.4: SEM pictures of the two 30nm TiN samples taken by Nathaniel Kinsey: a) the high quality sample grown at 800 °C on a sapphire substrate with ordered grains, b) the low quality sample grown at 350 °C on a fused silica substrate with more disorganized grains.[5]

2.2.2 Permittivity

The complex permittivity of the two samples was obtained by the Purdue group using ellipsometry and is shown plotted in Figure 2.4, with the permittivity of gold plotted for comparison. As was stated earlier, the negative real permittivity, ϵ_1, is what gives TiN metallic optical properties; it can be seen from the figure that the high quality film is more metallic than the low quality film. The ϵ_1 of the high quality TiN film crosses zero at 500 nm and the low quality film crosses at 620 nm. These two films are chosen to be compared since they show the tunable range of the

dielectric function for TiN. The ability to tune the material to have certain properties is potentially very useful, however, these properties are not tuned in isolation, and most likely the stoichiometry of the film is shifting with the "quality".

A summary of different TiN growths on different substrates shows a range of ϵ_1 zero crossings from 420 nm (2.95 eV) to 620 nm (2 eV)[57]. The energy at which ϵ_1 crosses zero is the screened plasma energy. In a free electron model, this would be the unscreened plasma energy E_{pu}, however in real metals this is shifted due to interband transitions; the shifted crossing occurs at the screened plasma energy E_{ps}. One experiment showed 468 nm (2.65 eV) as the ϵ_1 crossing[58], and another at 495nm (2.5 eV)[57]; both claimed to have stoichiometric films. While E_{ps} is related to stoichiometry, at this time it can only be used as an estimate, which is partially due to the error of the measurements determining the stoichiometry. While the zero crossing has been proposed as a way to estimate the stoichiometry of a sample, the exact value is not known; the high quality film zero crossing is much closer to the expected value than the zero crossing of the low quality film. It is reasonable to conclude that the high quality film is more stoichiometric than the low quality film.

2.2.3 Stoichiometry

The stoichiometry of the two films was measured using EDX. In Table 2.1 the weighted percentages of the composition can be seen. The first two columns show the TiN, while the rest of the columns are representing the substrates: sapphire (Al_2O_3) and fused silica (SiO_2). From this data we can see that the high quality film is very nearly stoichiometric, while the low quality film is not. This is supported by their respective values of E_{ps}. While these are both good indicators of the stoichiometry, the values in the table were measured from energy lines <5 keV, which are very susceptible to error (relative standard error ~12%)[59]. Due to that, these numbers are not presented as actual proof of stoichiometry, but presented in conjunction with the

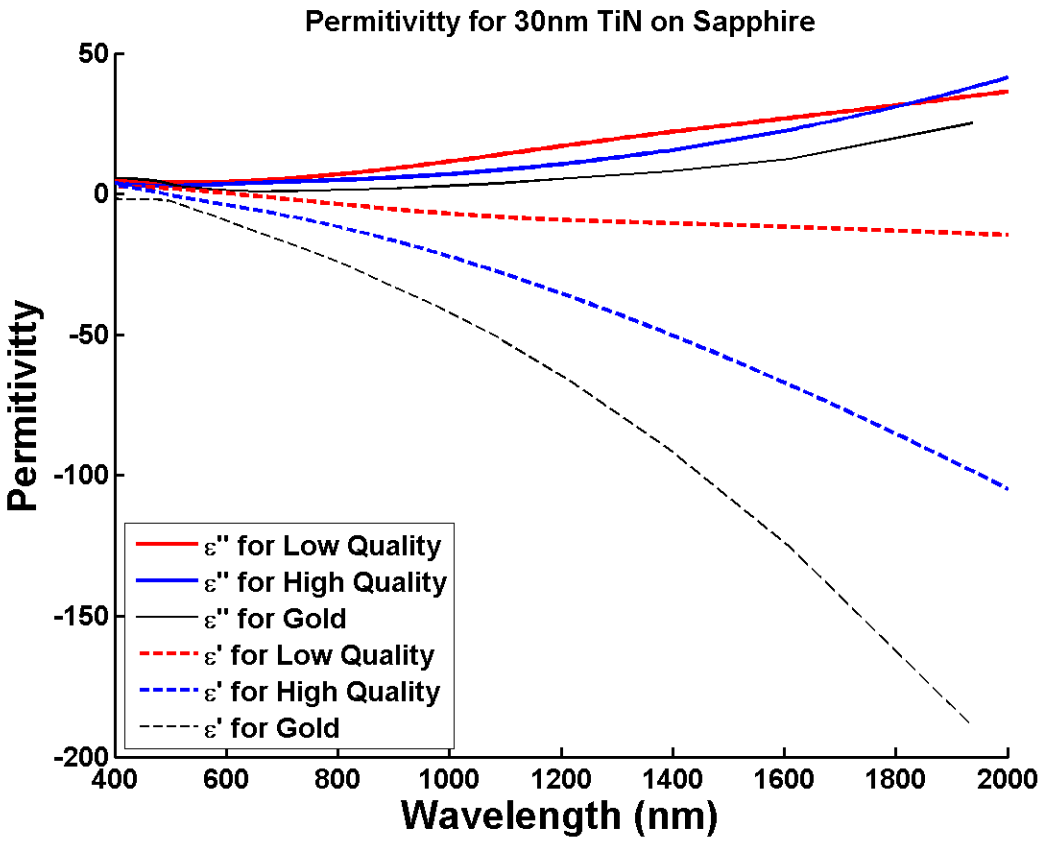

Figure 2.5: The measured real (dashed) and imaginary (solid) permitivitties of the 30nm High Quality TiN on double polished sapphire and the 30nm Low Quality TiN on Fused Silica measured by Nathaniel Kinsey using ellipsometry. The black lines are plotted from values for gold published by Johnson and Christy.[6]

E_{ps} as a comparison between the two samples. Other studies also confirm that growth at a higher deposition temperature leads to a more stoichiometric growth[56]. While several papers claim to have stoichiometric bulk or thin film TiN crystals, this claim should not be made lightly. Unlike the carbides, where extra nitrogen leaches out, TiN and the other nitrides can be overstoiciometric. This means that a film could have titanium and nitrogen vacancies, which in theory could average out to appear stoiciometric[55].

Table 2.1: The values presented here have a high relative standard error (~12%) and are only used to compared the relative stoichiometry of the two samples

Sample	Ti [wt %]	N [wt %]	O [wt %]	Al [wt %]	Si [wt %]
High-Quality TiN	26.4	24.9	5.8	41.8	0
Low-Quality TiN	23.6	26.2	8.3	0	40.7

2.2.4 Bandstructure

Typically, materials are classified as metals or semiconductors based on their bandstructure and other resulting characteristics. However, many materials do not have a clear distinct category, including TiN whose electronic bonding has metallic, covalent, and ionic components[7]. One of the distinguishing properties of metals is that their conduction band below the Fermi level gives them electrical conductivity. As can be seen in Figure 2.6, the conduction band of TiN dips below the Fermi level, just as you would see in the bandstructure of a metal. This bandstructure was achieved using the augmented-plane-wave (APW) method for purely stoichiometric, face-centered cubic (fcc) TiN[7] and is in fairly good agreement with other calculated bandstructures for TiN[8,9,60]. The actual values of the energy gaps vary slightly between the models and are depicted in Figure 2.7.

Many of TiN's electronic applications stem from its relatively high conductivity; however, the reported values of electrical conductivity/resistivity show as much variation as the other parameters of TiN. This is not surprising since the electrical conductivity will be very dependent on the number of free electrons and the electron mean free path. The number of free electrons is proportional to the stoichiometry, while the grain size, crystalline structure, and defects are variables in the length of the mean free path. The thickness of the film will also change the conductivity/ resistivity of the material as compared to bulk. A selection of literature values for the resistivity of TiN, including the thickness of the film is shown in Table 2.2 along with gold for comparison.

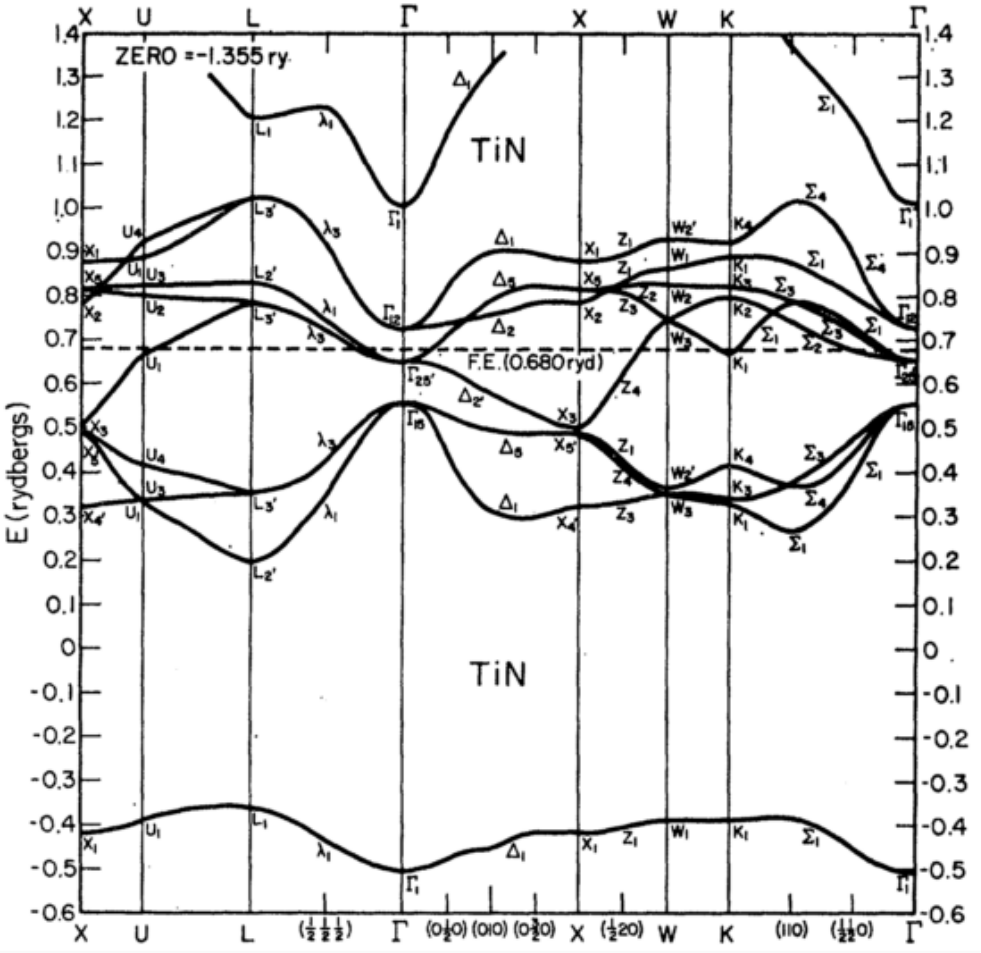

Figure 2.6: The band-structure of stoichiometric TiN[7].

Table 2.2: Values of resistivity for different thicknesses of TiN at 300K. Gold is included as a point of comparision.

TiN						gold
resistivity ($\mu\Omega - cm$)	20±10	13	12	43	104	2.44
thickness	bulk	bulk	260 nm	100 nm	2 nm	bulk
reference	[55]	[61]	[62]	[63]	[61]	[64]

It is not surprising that TiN has a resistivity approximately one order of magnitude larger than gold, because it has approximately one order of magnitude fewer free electrons. It is also clear that the resistivity can change by an order of magnitude based on the thickness of the material. This change is due to the available paths in one direction shrinking, as well as surface roughness and defects. While TiN is not a metal by definition, it is humorous that its conductivity is greater than the conductivity of Titanium, the metal element in the structure.

While TiN does have a band that crosses the Fermi level, it also has nearby valence bands which would allow for optically driven interband transitions like a semiconductor. A simplified picture of the energy bands around the Γ point are shown in 2.7. Interband transitions also occur in metals, that is what gives gold its color. However, the interband transitions in gold are not-semiconductor-like because they don't appear at the gamma point and are non-radiative. Traditionally, these types of of interband transitions, like the ones seen in TiN, are forbidden by selection rules. The difference here is that the bands in TiN are composed of mixed orbitals from the Ti and N atoms and the interband matrix elements are not yet calculated from theory. The orange arrow depicts the traditional metallic phonon assisted intraband relaxation. These potential interactions inform our understanding of the absorption processes that will be measured by pump-probe in Chapter 3.

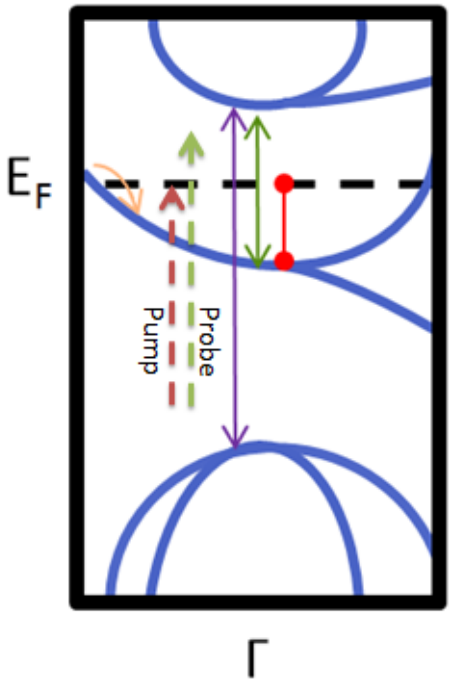

↕	↕	●
.171Ry	.075 Ry	.027 Ry
2.33 eV	1.02 eV 1.29 eV * 1.26 eV #	0.37eV
532nm	1.2um 961 nm * 984 nm #	3.35um

Figure 2.7: A simplified depiction of the band-stucture with energy gaps of interest labeled. The energy values were taken from[7], with additional values from[8*] and[9#], respectively. The vertical arrows depict interband transitions that may or may not be allowed. The small orange arrow depicts an intraband transition.The pump and probe phonon energies are shown as the dashed arrows.

CHAPTER III

TiN electron dynamics

Transient pump-probe experiments were conducted to measure the electron dynamics in TiN thin films. A brief overview of the setup will be given, but for a more detailed discussion on pump-probe setups and experimental choices, such a relative spot sizes of the pump and probe, appropriate laser choice, and types of configuration, please refer to *Optical Techniques for Solid State Material Characterization*[2].

It is useful to know for literature searches that the transient pump-probe measurement goes by a few different names and acronyms, including thermomodulation, time-resolved differential transmission (TRDT), and time domain thermoreflectance (TDTR). These all use a very similar setup to the one described in the following section. These measurements focus on two timescale regimes depending on the purpose of the measurement. Electron dynamics measurements are generally focused on the $<$20 ps timescale. Other measurements only consider the timescale $>$ 50 ps, which avoids the complicated hot electron regime and only measures thermal constants such as conductivity and interface conductance. Both the short and long timescales will be discussed in these measurements.

3.1 Experimental setup

The reason that transient pump-probe measurements are so precise in time is that they are not dependent on slow averaging electronics; even fast photodiodes do not exceed tens of GHz in bandwidth. Instead, pump-probe is only measuring the change in the system due to the perturbation of the pump. What is actually being measured is difference in the current across the photodiode when the pump pulse is present and when it is not:

$$I_{probe,pump\mathbf{on}} - I_{probe,pump\mathbf{off}} = I_{signal} \tag{3.1}$$

This gives a steady state solution for a fixed delay between the two pulses, and is averaged over many pulses. To measure relaxation dynamics, the scan is collected as the probe pulse is varied in time with respect to the pump pulse, using a delay stage. Other types of data, such as spectral dependence, may be collected by varying other parameters, such as scanning the wavelength of the pump or probe.

A picture of the pump-probe setup used is seen in Figure 3.1. The main source is an ultrafast Ti:Sapphire system from Coherent including a MIRA oscillator, RegA amplifier, and Optical Parametric Amplifier (OPA). The RegA has an output of 1.3 W, at 250 kHz, with pulsewidths $\sim$100 fs. Though this power exceeds what we would ever need for a pump or a probe beam, the high power is used in wavelength conversion processes in the OPA, that are very inefficient, to create a tunable beam. Some of the experiments described also used a BBO on the 800 nm path to produce a 400 nm beam.

A half-wave plate (HWP) is placed in the pump path so that the relative polarizations of the pump and probe are orthogonal on the sample. In degenerate pump-probe this is can be used as a filtering technique to separate the pump and probe before the detector. However, even in non-degenerate pump- probe where the two beams can be filtered spectrally, this is an important component of the setup to avoid

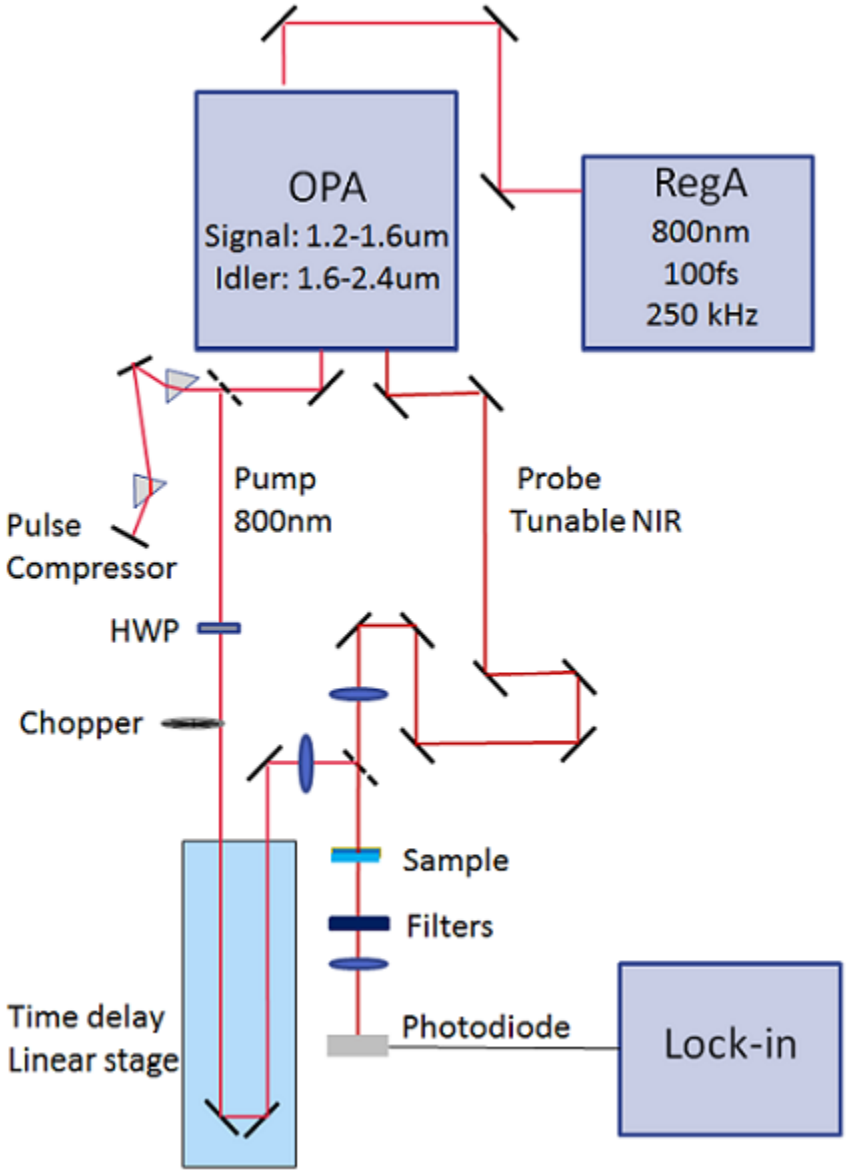

Figure 3.1: The pump-probe setup for the wavelengths of some of the experiments. Other configurations included a visible OPA, as well as a BBO in the 800 nm path to use second harmonic generation to create a 400 nm beam.

coherent artifacts. Coherent artifacts occur during the cross-correlation time of the two pulses and since it is a coherent interaction between the pump and probe, it is suppressed when the polarization of the two beams are orthogonal.

The chopper is placed on the pump path in the initial step of the experiment and the lock-in is phased with the pump pulse by blocking the probe pulse and scattering the pump pulse into the detector. This not only allows the phase to be set correctly, but also establishes a positive sign of signal with the arrival of the pump pulse. From this, the overall sign of the transmission data will be set. A positive change in transmission of the probe, due to the pump pulse, shows a saturable absorption. The states that the probe pulse would have occupied have already been occupied by the pump photons. By contrast, a negative differential transmission is an increase in absorption due to the opening of available transitions.

Pump-probe will measure the changes on a fs/ps regime. The fast limited is created by the resolution determined by the width of the pulses. The longer limit is created by the physical length of the motorized stage, which varies the time between the two pulses (and the ability to keep the beam aligned with the stage/ keep a constant spotsize). In this work, the pulses are 100- 200 fs, and the stage allows for approximately 550 ps of delay.

Since metals are highly reflective, and may have little to no transmission, they are usually measured in a reflective setup; however, in the low fluence regime, beneath the melting threshold, the differential reflection and differential transmission will show the same dynamics. The transmission setup is slightly easier to build, and the beams can be normal incidence. A transmission configuration was used since the TiN films were thin enough to have a detectable differential transmitted signal.

3.2 Time-resolved differential transmission experiments

As was described in Chapter 1, when the pump pulse is incident on the metal, electrons absorb the light and are excited to very hot temperatures; they then thermalize and eventually transfer the heat to the lattice. By measuring the change in the dielectric function due to this excitation, the timescale of the electron-phonon coupling can be evaluated as the electrons transfer their heat to the lattice. The choice of pump wavelength and probe wavelength, as well as the timescale evaluated will determine what information can be extracted from the data.

3.2.1 800 nm pump 650 nm probe

If the pump photon energy ($E = \hbar\omega$) is not sufficient to cross any direct bandgaps, then free carrier absorption is dominant. This is what is typically seen in a Drude metal. The probe photon energy will then determine the sign of the $\Delta T/T$, depending on whether there are other transitions made available by the probe. In gold, the sign flips at 2.46 eV[31] where interband transitions from the d-band electrons are probed. From Figure 2.7, it is apparent that an 800 nm pump (1.55 eV) would only be sufficiently energetic to move electrons from the lower conduction band, but not the valance band.

Figure 3.2 shows a representative scan for an 800 nm pump and 650 nm probe. The first obvious observation is the negative $\Delta T/T$, which shows an increased absorption. The pump is exciting electrons across the Fermi level which leads to an increase in available states for the probe photons. There is a peak on the 4 ps timescale, as well as a very slow decay over hundreds of picoseconds; these two timescales are shown separately in the two subplots of Figure 3.2, because the first peak is barely visible on the 550 ps timescale that captures most of the decay. These two timescales also represent the regimes where electron dynamics are important and where thermal conduction in the lattice is the only effect.

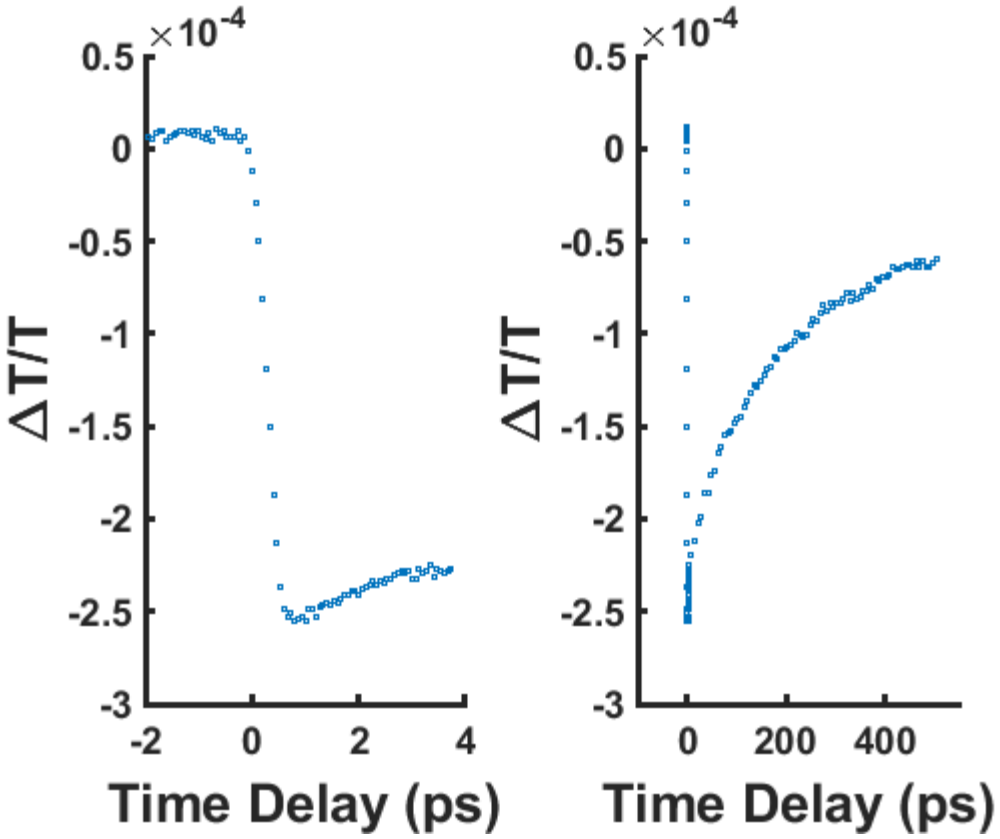

Figure 3.2: A representative scan of the high quality TiN using an 800 nm pump and 650 nm probe. Pulsewidths are < 150 fs, both have been recompressed after the OPA. Pump fluence is 6 μJ/cm^2, with a 10:1 power ratio between the pump and probe.

3.2.2 Comparison to gold

At first glance, the fast peak in TiN does not look similar to the relaxation dynamics measured in gold[29]. In these references, gold has almost completely relaxed to a small offset by 4-8 ps. The relaxation also appears more exponential, than the linear response seen in Figure 3.2a. However, this is misleading because the sample thickness plays a key role in the response, as demonstrated by Hohlfeld et al.[1].

Figure 3.3 shows several key ideas, first that the appearance of relaxation decay is very dependent on the sample thickness, particularly once the sample is thinner than 100 nm; the TiN samples are 30 nm. Secondly, as the samples get progressively thicker, it becomes more important to include ballistic transport into the model. With 30 nm samples, this does not need to be a consideration in the TiN model. The most

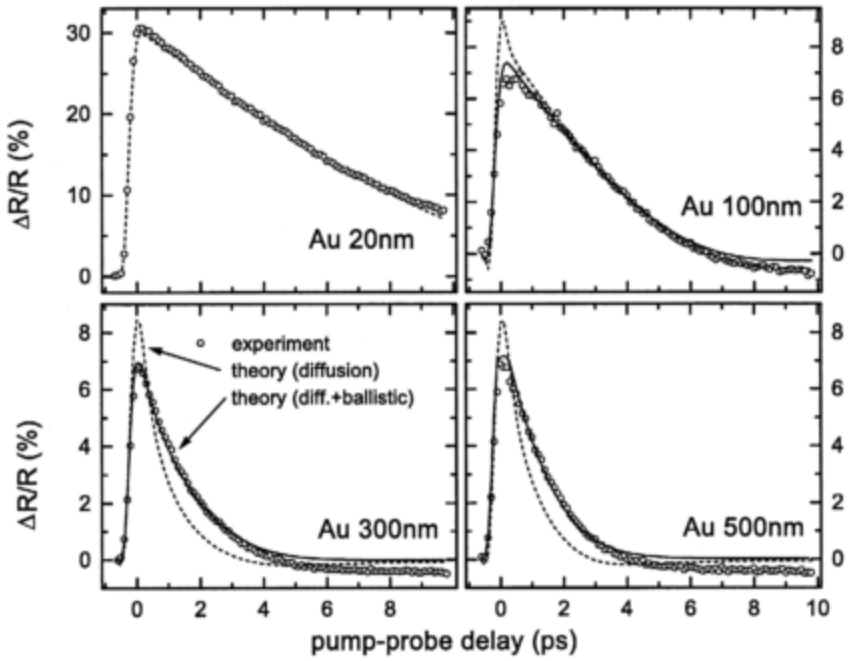

Figure 3.3: Measured ΔR from gold films of varying thickness. The dotted line represents a two temperature model (TTM) fit. The solid line includes ballistic energy transport, which doesn't play a role in the 20nm thick sample.[1].

significant difference is in the amplitude. Even for the thin sample, the $\Delta R/R$ signal has decayed by more than 70% of the $(\Delta R/R)_{max}$ in the 10 ps plot. However, the amplitude change of the TiN in the first initial peak changes less than 10%. TiN does show this small short timescale peak which can be attributed to Fermi smearing, the change in the occupation probability of the states. However unlike gold, this is not the main interaction giving the signal. The main contribution to the signal in TiN is a combination of other thermal processes, mainly strain in TiN and diffusion to the substrate.

3.2.3 400 nm pump 800 nm probe

While gold does have interband transitions, these do not occur at the gamma point and would not be considered semiconductor-like. In the simplified TiN bandstructure, Figure 2.7, it can be seen that TiN does have the potential for semiconductor-

like transitions that would create an electron and hole pair. However, this will be dependent not only on pumping at the right energy, but also on the relative strength of the electron-hole pair creation vs. the free carrier absorption by the conduction band crossing the Fermi level. These transitions are governed by the joint density of states (JDOS). The 400 nm pump should be sufficient to excite electrons to the upper conduction band.

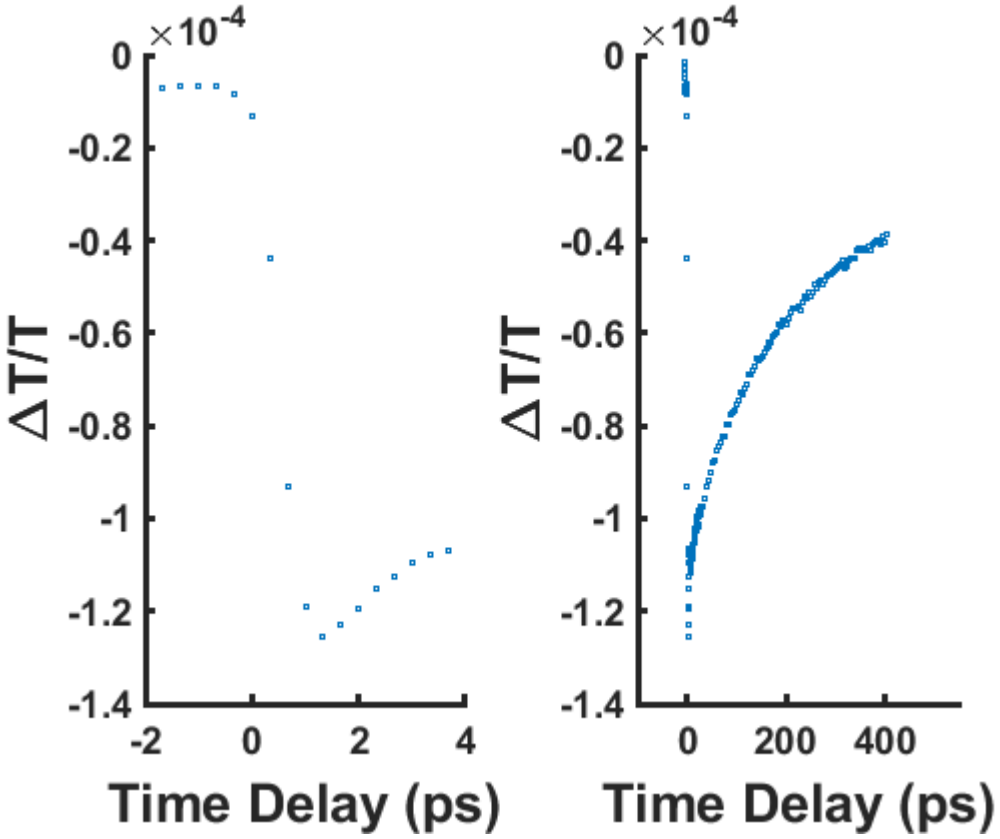

Figure 3.4: A representative scan of the high quality TiN using a 400 nm pump and 800 nm probe. Pulsewidths are $<$ 150 fs. The 800 nm is used to generate 400 nm in a BBO crystal. Neither is recompressed after the generation. Pump fluence is 3.8 μJ/cm^2, with a 10:1 power ratio between the pump and probe.

From Figure 3.4a it can be seen that the response is very similar to the response using an 800 nm pump. This would indicate that the free electron absorption overwhelms the interband transitions between the valence band and the upper conduction band. These wavelengths were chosen since they had the potential to give very dif-

ferent responses; however, at both wavelengths, TiN behaves like a Drude metal.

3.3 Two temperature model

Since TiN behaves like a Drude metal at the wavelengths investigated, it is appropriate that the two temperature model is used to fit the dynamics. The two temperature model (TTM) is the classic model that has been used to fit many metals including, Au, Au, Cu, Al, W, Ti, and others. The comparison to gold is important since gold is the plasmonic material we are using as standard, but since gold is a noble metal it would also have the response closest to the free electron model. Therefore, it is good to see that "less ideal" metals can also be fit using the TTM.

3.3.1 Background

Start with the well know heat conduction equation:

$$C\frac{\partial T}{\partial t} = \nabla \cdot (k\nabla T) + S \tag{3.2}$$

where C is the volumetric heat capacity [J/m^{3}K], T is the temperature [K], k, the thermal conductivity [W/mK], and S is the absorbed excitation source [W/m^{3}K]. If k is assumed to be temperature independent, which is only a good assumption over small temperature ranges, then the equation simplifies to a parabolic equation.

This equation is the basis of the two temperature model which was proposed by Anisimov, et al. (1974) .[65],

$$C_e\frac{\partial T_e(t)}{\partial t} = -g(T_e - T_l) + k_e(\nabla^2 T_e) + S(t) \tag{3.3}$$

$$C_l\frac{\partial T_l(t)}{\partial t} = g(T_e - T_l) \tag{3.4}$$

where the first equation describes the heat transfer of the electrons, and the second, the heat transfer of the lattice. C_e and C_l are the respective volumetric heat capacities, k is the thermal conductivity, and $S(z,t)$ is absorbed the energy per volume from an excitation pulse. G is the electron-phonon coupling constant that governs the transfer of energy from the electrons to the lattice. C_e is a temperature dependent variable which has different equations for different temperature regimes, however, this work stays in the linear regime:

$$C_e = \gamma T_e \tag{3.5}$$

where $\gamma\,[J/m^3K^2]$ is the electron contribution to the heat capacity. The conductivity of the lattice is often neglected because this model is typically only used to fit the decay of metals which occur on a timescale < 5 ps, and the lattice conductivity has a negligible contribution on that timescale. Refer to[66] for a review of some of the different models that have been used to capture this interaction over the last several decades.

The excitation equation commonly used is:

$$S(z,t) = -\sqrt{\frac{4ln2}{\pi}}\frac{(1-R-T)F}{\delta\tau_p}exp\left\{-\frac{z}{\delta} - 4ln2\left[\left(\frac{t-2\tau_p}{\tau_p}\right)^2\right]\right\} \tag{3.6}$$

R is the sample reflectivity, T is the transmission, F is the fluence, δ is the optical penetration depth, and τ_p is the pump pules duration. This source term frequently does not include T, because often the sample is optically opaque, so it is zero. However, in transmission setups it is necessary to account for the light passing through the sample. Adaptations of this source term include adding ballistic motion of the electrons[1] and internal thermalization propagation[67]. Including the thermalization, is one approach to accounting for the risetime, which will be discussed in a later section.

3.3.2 Model parameters

Using Equations 3.3 and 3.4, a TTM was established in Matlab using PDEPE, a parabolic differential equation solver. Many TTMs are solved using the finite element method (FEM). PDEPE is a Matlab function that creates ordinary differential equations (ODE) in time and uses FEM in one dimensional space. The space dimension, z, is perpendicular to the thin film surface, allowing the propagation of heat through the sample.

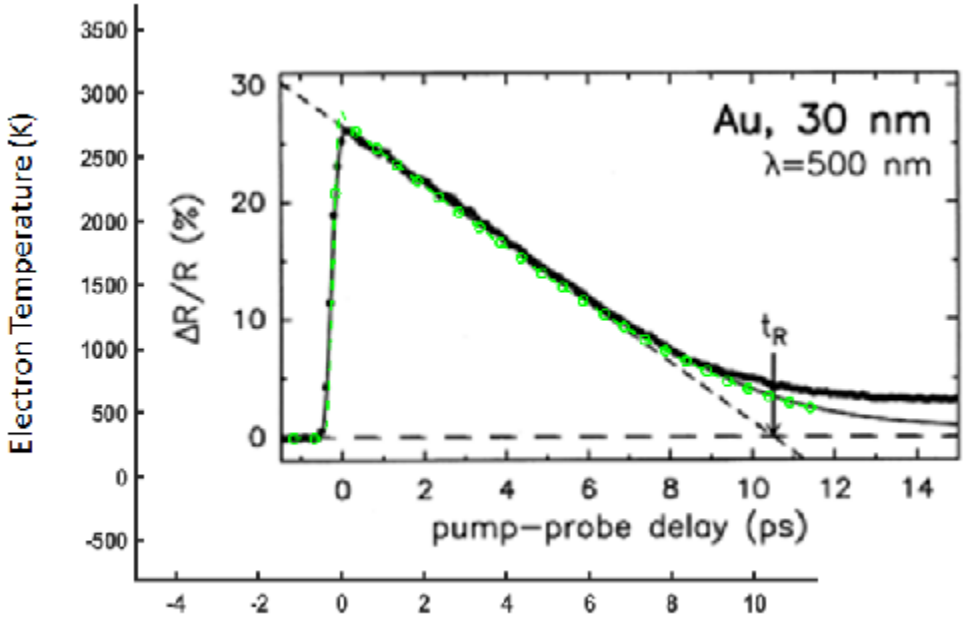

Figure 3.5: Matlab TTM (green dashed line) overlaid on a figure from Hohlfeld et al.[1]. Values from Hohlfeld, as well as other estimates from literature were used; except to achieve a good fit, the incident power used in the model was increased by a factor of two over what was quoted by Hohlfeld. This is a reasonable factor of error considering that some of the parameters were not sample specific and general values for gold were used.

In order to verify the model, parameters from Ref.[1,6] were used in the model and show up as the green dashed line in Figure 3.5. In order to achieve the fit overlaid on

Table 3.1: These are parameters used in the TTM model. Some of the values are wavelength specific, so the values in this table are for an 800 nm pump. Except for the densities, which are well known, if no reference is shown in the table then those parameters were measured; if the TiN values are the same, the reference is only listed for the first column.

Model Parameters	TiN High Quality	TiN Low Quality	Gold
$k[W/mK]$	15[68]	15	315[68]
γ [J/m^{3}K^2]	274[69]	274	71[70]
$C_l[J/m^3K]$	3.13 $x10^6$[71]	3.13 $x10^6$	2.5$x10^6$[70]
$\rho[kg/m^3]$	5210	5210	19300
$\epsilon_{1,pump}$	-11.7	-3.6	-24.1[6]
$\epsilon_{2,pump}$	4.9	6.9	1.5[6]

the figure, the absorbed fluence was increased by a factor of two. However, considering that many of the other parameters were not sample specific, or not detailed in the paper but assumed parameters for gold, this is deemed to be a reasonable factor of error.

In order to give intuition about the effects of certain parameters in the model, a few plots where specific parameters have been tuned, are shown. In Figure 3.6, the electron and lattice temperatures are plotted. The value of the electron-phonon coupling for both was set to the value for gold, G= 2.1x10^{16} [W/m^{3}K], but the other material parameters, γ, C_l, k, and absorption, are material specific to gold and TiN.

The thermal properties of TiN are significantly different than gold. The heat capacity for the electrons is an order of magnitude higher in TiN than in gold, while the thermal conductivity is an order of magnitude smaller. This is apparent in Figure 3.6a; the electrons in gold reach a much higher temperature, due to the lower C_e. They also get rid of that heat faster as evidenced by the steeper slope, due to the increased conductivity. The lattice parameters are also plotted in the left subplot, but since they have a much smaller change, they are barely visible on this plot. In

3.6b, T_e and T_l are plotted for both gold and TiN; in this plot the change in the temperatures is normalized so that both the T_e and T_l are visible.

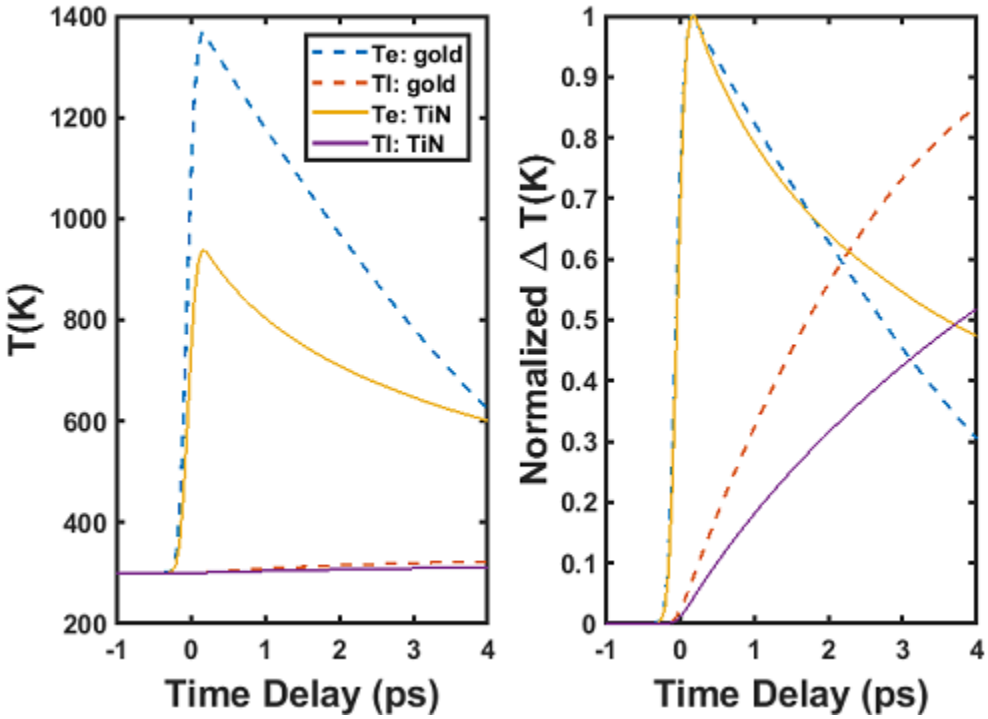

Figure 3.6: Results of the two temperature model, assuming the electron-phonon coupling of gold, G=2.1x10^{16} [W/m^{3}K], for both TiN and gold. The other parameters C, k, and absorption are material specific to TiN and gold. For details of parameters used, see Table 3.1. Left panel: the electron temperatures of TiN (solid lines) and gold (dashed lines) are the prominent peaks, with the lattice temperatures barely visible. Right: the same model as the right panel, only the temperatures have been normalized so that the lattice temperatures are visible and the rise times and delays can be compared.Fluence= 1 mJ/cm^2

3.3.3 Electron-phonon coupling G

The electron-phonon coupling constant is a material parameter that was established to quantify the electron-phonon interaction. It is a constant that is associated with metals, since the TTM was developed for metals. Several measurements have been made for gold and range from 1.1x10^{16}- 4x10^{16} [W/m^{3}K][1]. TiN is not a metal, even though its conductivity is high enough to be used in electronic applications.

Therefore, this model gives insight into the interaction in TiN, but has limitations that will be discussed.

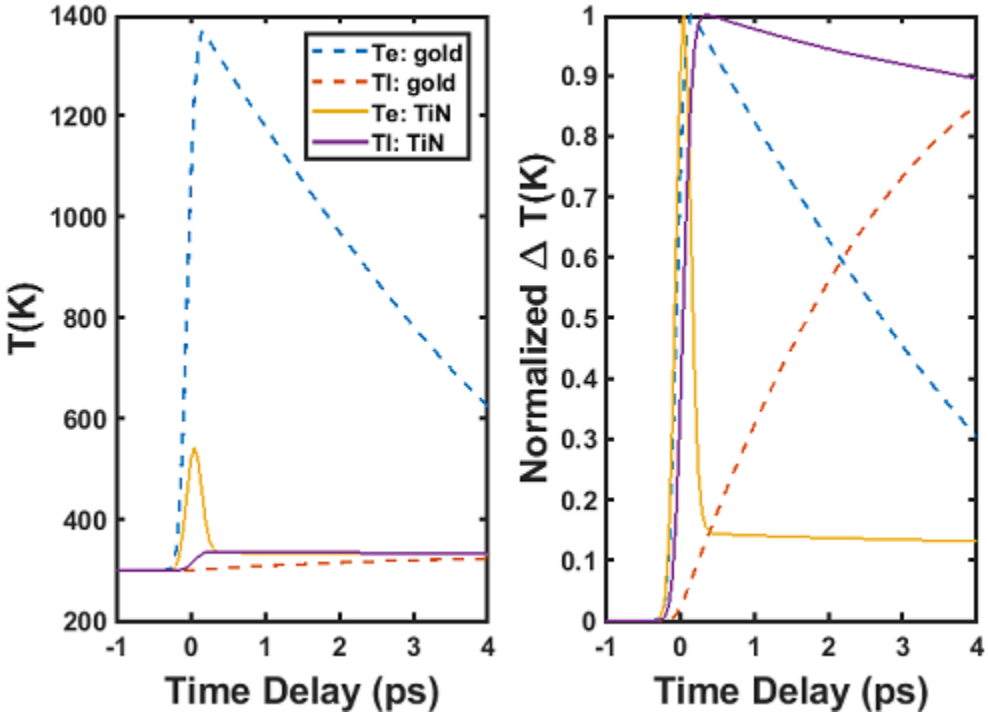

Figure 3.7: Results of the two temperature model, gold G=2.1x10^{16} [W/m^{3}K] and TiN G=2.1x10^{18} [W/m^{3}K]. The other parameters C, k, and absorption are material specific to TiN and gold. All parameters are the same as in Figure 3.6. Left panel: the electron temperatures of TiN (solid lines) and gold (dashed lines) are the prominent peaks, with the lattice temperatures barely visible. Right: the same model as the right panel, only the temperatures have been normalized so that the lattice temperatures are visible and the rise times and delays can be compared.

Figure 3.6 showed the effect of the material specific constants of TiN compared to gold when the electron-phonon coupling is set to be the same for both materials. Now the effect of G on the model output will be shown in Figure 3.7a. Here the dramatic effect of changing the G by three orders of magnitude is shown, G_{TiN} = 2.1x10^{18}. The first observation is that the electron temperature does not reach nearly the temperature of the hot electrons in gold. This can be seen because the lattice is rising much faster and to a higher temperature, than the gold lattice. Figure 3.7b clearly shows the difference in the risetimes of the respective lattices temperatures.

In many ways, this is an obvious result; if the coupling between the electrons and the phonons is strong, then the energy will quickly be transferred to the lattice. This is all the energy that was previously going to the hot electrons which can quickly move through the material. Once the energy is transferred to the lattice it moves slower. The lower thermal conductivity and the fast transfer of energy from the electrons to the lattice has a compounding effect to where the TiN electrons do not reach high temperatures, and the lattice goes to higher temperatures.

The other important effect demonstrated in Figure 3.7b is that the risetime of the electrons and the risetime of the lattice are very close. The timescale shown here makes then look almost indistinguishable, but our measurement has the resolution of ~ 0.15 ps, so there should be a measurable effect. Especially since the amplitudes are very different, as is seen in the first panel.

3.3.4 Inclusion of the lattice and substrate

The plots of the model and the long tail in the TRDT data make it obvious that the lattice is playing a huge role that cannot be neglected, even on a few ps timescale. However, at first it was not clear that the lattice was having this effect. Initially, it was thought that this long decay was very long lived hot electrons in the system. However, after COMSOL simulations showed that the entire longtime scale could be fit by a basic heat transfer model with just a delta input of heat, Q, equal to the absorbed energy of the pulse, it was determined that the substrate was playing a key role that could not be ignored.

The COMSOL model did not include any type of interface conductivity at the thin film/substrate boundary and bulk values of TiN were assumed. The thermal conductivity of thin films can vary from the bulk by an order of magnitude. Despite these assumptions, the curvature of the decay fit the data very well, as is seen in Figure 3.8. Since the $\Delta T/T$ does not directly give an exact temperature rise, the

amplitudes were normalized to each other. The rise in temperature of the lattice, (T_{max}), predicted by COMSOL was a few °C, which is a reasonable change. What is so compelling about this fit, is that it captured the long timescale difference between the two relaxations, based solely on the change in k and C of the two substrate materials. Since fused silica has a thermal conductivity that is an order of magnitude lower than that of sapphire, the heat diffuses slower throughout the material

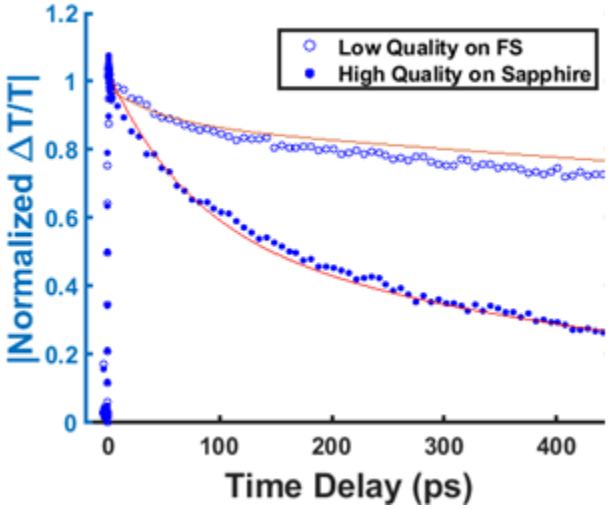

Figure 3.8: COMSOL model demonstrating that the long timescale can be fit with a basic heat transfer equation. The data are normalized with the absolute value taken so that the red lines showing the COMSOL model of the temperature could be shown with positive values.

The COMSOL model fit the long lifetimes of the decay, but it could not capture the < 4 ps timescale. Looking back at Figure 3.2b, the short timescale peak looks like a spike right after the time zero. The amplitude of the fast peak is significant, $\sim 10\%$ of the entire amplitude. This fast peak could not be explained through just heat transfer in the film and substrate, so it is attributed to the interaction of the electrons and the lattice. When the TTM is used to fit noble metals, only the electron temperature is used to fit the data; the lattice only appears in the coupling constant as a path for heat diffusion. This doesn't not work when the heat is being efficiently coupled to the lattice. In order to include the lattice in the two temperature model

response, we assume the electron and lattice contributions to the optical signal can be taken as:[32,72]

$$\Delta T = A\Delta T_e + B\Delta T_l \tag{3.7}$$

As was seen in the COMSOL simulation, at times greater than 4 ps, heat transfer to the substrate is the dominant effect. The substrate was included in the model as a composite wall, where T_l could propagate into the substrate. The thermal conductivity of the lattice was obviously not negligible, so the equations used in our model were:

$$C_e \frac{\partial T_e(t)}{\partial t} = -g(T_e - T_l) + k_e(\nabla^2 T_e) + S(t) \tag{3.8}$$

$$C_l \frac{\partial T_l(t)}{\partial t} = g(T_e - T_l) + k_l(\nabla^2 T_l) \tag{3.9}$$

The thermal conductivity of the lattice is assumed to be the thermal conductivity of TiN multiplied by 0.01; this value was chosen since the majority of the heat transfer should happen through the electrons, but if at least some heat isn't allowed to propagate through the lattice, then the model can't let the heat transfer to the substrate. Figure 3.9 shows the high quality sample fit with several values of G. While none fit perfectly, it seems that the G is on the order of 10^{18}.

3.3.5 Thermal conductivity and thermal interface conductance

After adding the heat diffusion equation into the model, it was still a struggle to fit the short and long timscale data for the low quality sample. The data from the high quality fit well. In the TTM model for TiN, the thermal conductivity had been assumed from bulk constants in the literature; the room temperature value was interpolated from the 200° C value and the 650° C[68]. However, as we have discussed, TiN has a lot of sample variation and the thickness could contribute to the bulk value not being a valid.

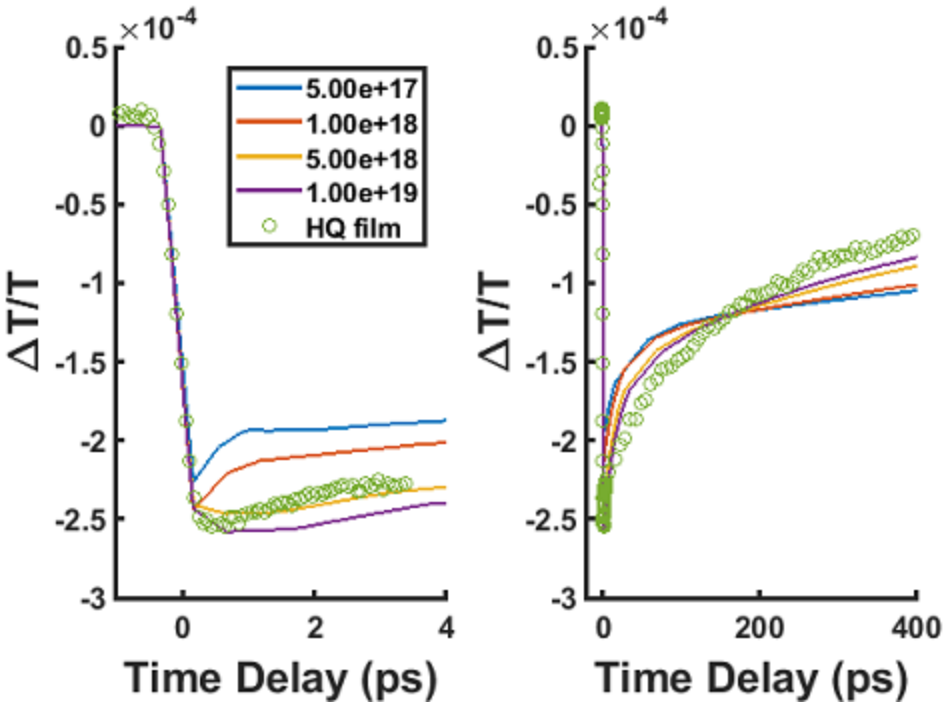

Figure 3.9: Pump probe measurements for the high quality film on sapphire with a two temperature model of a) the short timeframe and b) the long timeframe for different values of G.

Ironically, pump-probe measurements for timescales $>$ 50 ps, are often used to measure the thermal conductivity of materials. However, as the sample becomes very thin, the interface between the film and the substrate has its own conductance, which is also G [W/m^{2}K]. The thermal conductivity and the interface conductance cannot be measured simultaneously in a single experiment. For thin films, a reference measurement has to be made first.

3.3.6 Electron-phonon coupling λ

G is often determined from ultrafast optical experiments. However, the effect of electron-phonon coupling is also encountered in the phenomenon of superconductivity; in that literature, the parameter λ is usually used. For the sake of clarity, this variable will be referred to as the superconductivity electron- phonon coupling, or simply λ. It is a dimensionless parameter that is "subject to substantial error" [73]. Despite that,

we can used measurements of λ to provide constraints on our value of G.

Though the applications that have been presented so far do not exploit TiN's superconductiy, this is one of the main reasons that TiN is a material of interest for several investigators. Depending on its quality, TiN has a superconducting transition temperature (T_c) $\sim$ 5K for a stoichiometric sample[62,74]. Other superconductors have transition temperatures of 20K, while metals like gold and silver do not become superconducting at any temperature. While all of the experiments and applications discussed thus far are far above (T_c), the electronic properties that make TiN a superconductor also play a role in the room temperature operation.

This equation is the first order approximation by Allen, et al that connects the relaxation rate of the electron temperature to λ[75]:

$$\frac{\partial T_e}{\partial t} = \frac{3\gamma\lambda\langle\omega_2\rangle}{\hbar\pi k_B T_e}(T_l - T_e)^1 \tag{3.10}$$

γ is the electron constant for the heat capacity and $\langle\omega_2\rangle$ is the second moment of the phonon spectrum. The factor $\lambda\langle\omega_2\rangle$ is an important value in superconducting theory and they are often written together as one unit[2]. In 1990, Brorson applied this equation to the electron equation in the two temperature model where the heat conduction term is neglected due to uniform heating in optically thin samples[72].

$$C_e\frac{\partial T_e(t)}{\partial t} = -g(T_e - T_l) \tag{3.11}$$

[1]In Allen's orginal paper and in Brorson's paper, this equation has the $\hbar$ in the top of the fraction. However, this makes the units incorrect. Hohlfeld, in the caption of Table 1, moves the $\hbar$ to the denominator, but doesn't say anything about it[1]. This change makes the equations correct dimensionally.

[2]Holhfeld calls this the McMillan factor, and it was McMillan's theory[76] that popularized an important superconductivity equation that has them together. Other authors seem to shy away from calling it anything as a unit, but uses the symbols together ($\lambda\langle\omega_2\rangle$) throughout the text.

Table 3.2: TiN material constants used from literature to calculate G.

Constant	Value	Reference
γ [mJ/mol*K^2]	2.5-3.6	[69,78]
λ	0.59-0.64	[9,77,79,80]
Θ_∞ [K]	487-518	[77]
$\langle\omega_2\rangle$ [J^2]	4.5x10^{-41} - 5.1x10^{-41}	calculated
G [W/m^{3}K]	3.6x10^{18}-6.5x10^{18}	calculated

Combining these equations where $C_e = \gamma T_e$ gives the relationship:

$$G = \frac{3\gamma\lambda\langle\omega_2\rangle}{\hbar\pi k_B} \tag{3.12}$$

The only constant that has not already been given is $\langle\omega_2\rangle$. This parameter is not readily available in literature, however $\langle\omega_2\rangle$ can be estimated $\approx \Theta_\infty^2$ [77]. The values shown in Table 3.2 were used to calculate the range of values for G also shown in the table. The G for gold was also calculated using this equation and fell within the error of quoted values.

3.4 Discussion

Thermal conductivities and capacities are available for the substrate, however the interface thermal conductance G [W/m^{2}K] between the TiN and the substrates, the exact conductivity of the film, and G the electron phonon-coupling could not all simultaneously be extracted. Using bulk parameters and G within the range of values calculated from material constants, the model can fit the high quality TiN in the fast and long timescales. The low quality film can be fit in the short timescale, but not the long timescale. We attribute this to two things: (1) the high quality film has a

conductivity which is closer to the values from literature than the low quality film and (2) the thermal interface conductance between TiN and sapphire is much higher than the thermal interface conductance between TiN and fused silica[81,82]. From this, we conclude that the fitting of the TTM and the calculated values show that G is on the order of magnitude 10^{18}, which is significantly higher than previously thought. Also, the electrons in TiN do not rise to the high temperatures seen in gold.

These two conclusions give insight into which applications could benefit from TiN, and which are not appropriate. Hot electron driven process can be split into two general categories. First, there are applications where the hot electron lifetimes are critical (e.g. when the hot electron is acting as a catalyst). With longer lifetimes, the hot electrons are more likely to contribute to the interaction. The short lifetimes will cause TiN to be less efficient. However, it has a stronger absorption than gold, so that could outweigh the inefficiency of the hot electron's shorter lifetimes. While we are still calling them "hot electrons" since that makes it an easy comparison to the electron reactions in gold, the TiN electrons are not nearly as hot, which will also impact some applications. The second category of applications would be plasmonic applications which are not dependent on the lifetime. This could be used in photothermalvoltaic applications, or medical treatments, such as cancer treatments which use localized heat[83]. The strong electron-phonon coupling means that the temperature of the TiN and its surrounds is heated locally, as opposed to being distributed quickly like a metal; TiN would be a very efficient local heat source.

CHAPTER IV

Background and motivation for InGaN/GaN nanostructures

The III-nitrides have become ubiquitous in the modern world, and yet there are still many opportunities to explore and engineer. These materials have been used in a variety of optoelectronic applications including lighting, lasers, detectors, single-photon sources, solar cells, and water oxidation. This chapter will provide a brief overview of the impact these materials are making in solid-state lighting and then move into the motivation for InGaN/GaN heterostructures in nanowires. The growth, photoluminescence, and band-structure will be discussed for selective area growth InGaN/GaN dot-in-nanowires.

4.1 Solid state lighting and displays

Light-emitting diodes (LEDs) revolutionized the energy consumed in creating light. Scientific work does not always have an immediate and measurable impact, but this has not been the case for efficient blue LEDs, which were first demonstrated by Nakamura in 1993. The Nobel committee stated in 2014 that the LED has the potential to improve the quality of life for 1.5 billion people who do not have access to the electric grid. It is also estimated that by switching to LED light sources, by

2030, the environment will be spared 180 million metric tons of CO_2 pollution in just the United States, due to energy savings[84]. Despite this dramatic success, there is still a lot of opportunity to improve solid-state lighting.

The three ways that white light emission LEDs are currently manufactured are shown in Figure 4.1. The advent of high efficiency InGaN blue and UV LEDs made white LEDs a reality. Most white LEDs are produced using phosphor down conversion; this is inherently an inefficient process, with an associated loss of 20-30%. In this context "white light" references an emission that is broad. However, as can be seen in Figure 4.1b, the spectra produced by the two phosphor conversion technologies discussed are weighted quite differently than the top line, which marks the relative spectrum of sunlight. Most notably, the blue LED has a strong blue peak that can affect people's circadian rhythm[85]. The combined RGB LED does not have a spectrum shown, since in principle, its emission could be tailored to a specific spectrum.

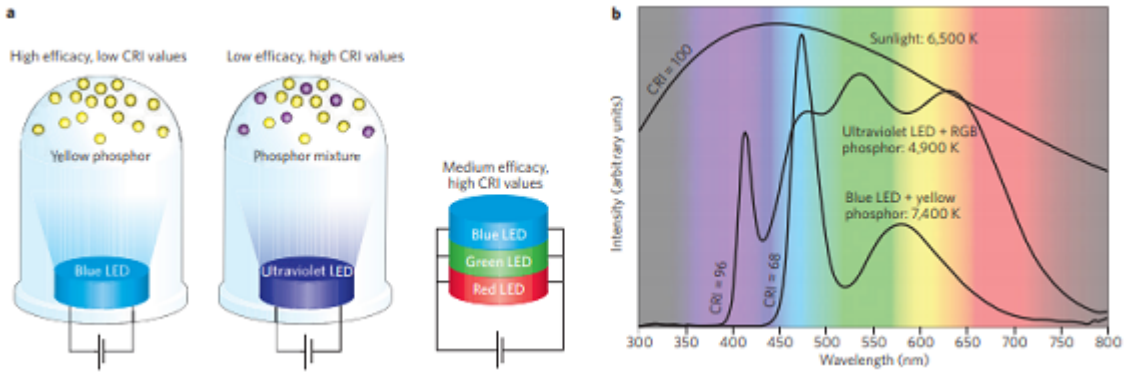

Figure 4.1: (a) Schematic of three white light LEDs designs. The first two designs use an LED and phosphor -conversion. A blue LED is paired with yellow phosphor and an ultraviolet LED is paired with red, blue, and green phosphor. The red, green, and blue LEDs can be combined to emit the light directly. (b) The color rendering index of the two phosphor- conversion devices. The spectrums are normalized to the weighting of the spectrum from sunlight.[10]

4.2 InGaN LEDs

Using InGaN as the active material in a combined RGB LED is a natural choice since both GaN and InN have direct bandgaps and the ternary compound can be tuned across the entire visible spectrum by changing the ratio of the In and Ga concentrations. In practice, GaN is the foundation for efficient blue LEDS, while efficient red LEDs are typically phosphide LEDs; this is due to a lower efficiency of nitride LEDs at longer wavelengths. The lack of efficient green LEDs has been called the *green gap*[11]. This makes the work on the samples studied in this thesis very exciting, because they emit in the green. While InGaN emission can span the

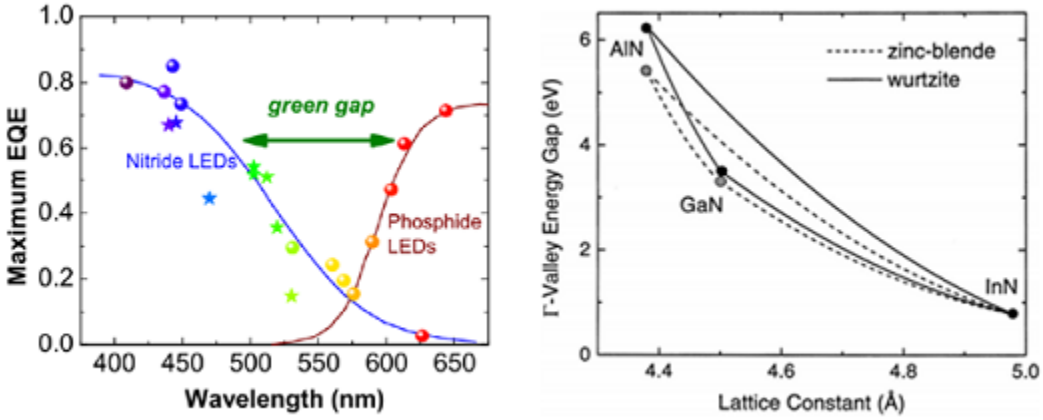

Figure 4.2: a)The green gap is used to describe the lack of efficient LEDs in the green/yellow region of the spectrum[11]. b)The alloys of the III-nitrides have the capability to span the visible spectrum. The realization of this tunability is limited by material issues created by alloying materials which have disparate lattice constants[12].

visible wavelengths (1.65 eV- 3.26 eV), this is not a trivial thing in practice; lattice mismatch, strain, and dislocations prevent a straightforward continuum of $In_xGa_{1-x}N$ alloys. The sweeping of the energy gap between GaN and InN is shown on the y-axis in Figure 4.2, with the lattice constant for the alloys shown on the x-axis. The InGaN structures discussed have a wurtzite crystal structure, shown as the solid line.

4.2.1 Quantum efficiency

One of the main reasons that LEDs have become universal is their efficiency in converting electricity to light. There are three main recombination processes; the first is a radiative recombination where an electron- hole pair recombine and emit a photon. However, not all energy that is input can be extracted as light; two non-radiative recombination processes limit the efficiency. Shockley-Read- Hall (SRH) recombinations are defect-related recombinations, where the electron or hole is trapped in a localized state in the bandgap, which is created by a defect in the crystal structure. The electron, or hole, eventually relaxes through phonon mediation. Auger recombination involves three carriers, where one of the carriers in an electron-hole pair gives its energy to excite another carrier. With two electrons and one hole (eeh), the first electron excites the second electron to a higher conduction band when it recombines with the hole. Likewise, with two holes and one electron (hhe), the first hole recombines with the electron and the second hole is excited lower in the valence band. The ABC model is used to characterize the internal quantum efficiency (IQE), η_{IQE}.

$$\eta_{IQE} = \frac{Bn^2}{An + Bn^2 + Cn^3} \tag{4.1}$$

The recombination processes, SHR, radiative, and Auger, are represented by A, B, and C, respectively. The processes are each multiplied by the carrier concentration, n, to the power of the number of carriers involved in the interaction. The radiative recombination, Bn^2, is divided by all of the recombination processes. Understanding SHR and Auger recombination, with the goal of reducing them to improve efficiency, has been the focus much research. The role of Auger recombination in our samples will be discussed in a later chapter.

4.2.2 LED structure

In Figure 4.3, the active region is depicted by light and dark layers sandwiched between a n-GaN layer and a p-GaN layer. A positive bias, denoted by the arrow, sends electrons into the depletion regime where they recombine to emit a photon, with an energy hv. Non-radiative effects have been discussed as material-related effects that reduce emission. Other obstacles include device-related effects such as carrier injection efficiency, electron leakage, and the quantum-confined Stark effect.

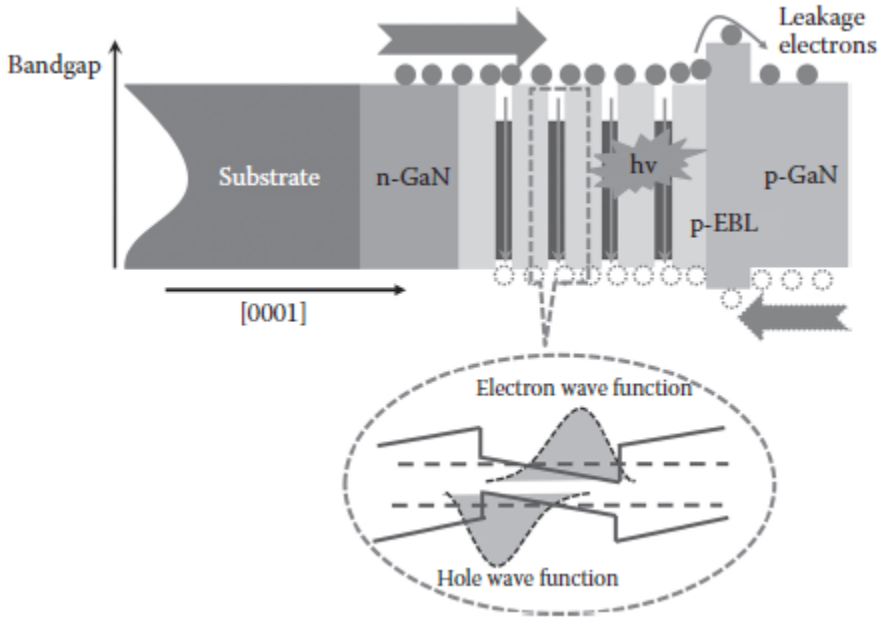

Figure 4.3: Schematic of a multi-quantum well (MQW) InGaN/GaN LED grown on the c-plane. The active region is flanked by n-GaN and p-GaN. The arrow depicts the applied electrical bias. A p-type electron blocking layer is on the right to deter electron leakage. The wurzite crystal structure has a strong quantum-confined Stark Effect which leads to the displaced electron and hole wave functions[13] .

4.2.3 Quantum-confined Stark effect

The growth plane directly influences the properties of InGaN. The most common type is c-plane (0001) growth, which is grown vertically with respect to a c-plane GaN base. This is also called the polar plane and exhibits the strongest piezoelectric

polarization due to charges at the interface. Due to the strong piezoelectric field (PZE), the wave functions of the electrons and holes can be separated in space. This separation is one of the main restraints on radiative recombination and is known as the quantum-confined Stark Effect (QCSE) This is illustrated in Figure 4.3 where the PZE field modifies the bands from being flat to creating a lower electron potential on the right and a lower hole potential on the left. This causes a spatial separation of carriers across the quantum well. The overlap of the electron wave function and hole wave function will increase their probability of radiative recombination. In the diagram, the c-plane (0001) is along the horizontal axis.

Quantum wells can be formed in the radial direction of a nanowire, which is the non-polar plane of a wurzite crystal nanowire grown on a c-plane substrate. These heterostructures have a significantly lower QCSE, but these devices have suffered from other issues that limit their performance. Currently, they have an IQE of 20-40%, which is significantly lower than their c-plane counterparts[86].

4.2.4 Density of states

A quantum heterostructure is the general term that refers to the cladding of one type of semiconductor material by a larger bandgap material with a dimension that is small enough to create quantum confinement. If the interface between the materials is flat (2D) this forms a quantum well. If there is strong confinement in more than one direction, then you have quantum wires, or quantum dots (QDs). The word heterostructure encompasses quantum wells (2D), wires(1D), and dots(0D). In an InGaN/GaN heterostructure, InGaN is the material that is clad by GaN. The cladding material has the larger bandgap. As can be seen in Figure 4.4, the level of confinement determines the density of states (DOS) for the system.

Due to the increased confinement, quantum dots (QD) have greater overlap of the electron and hole wave functions. They also have increased strain relaxation, because

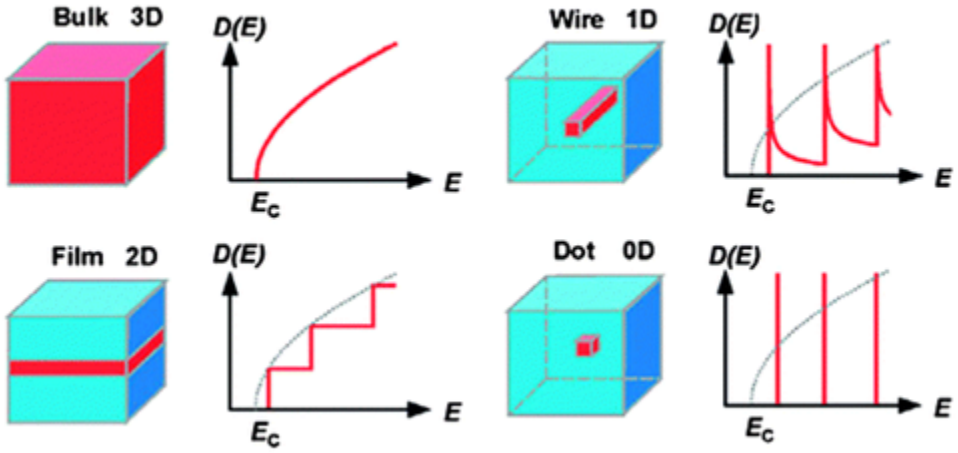

Figure 4.4: The density of states (DOS) as the degrees of freedom are decreased.[14]

their formation is dependent on atoms seeking to create a structure with the lowest strain. For these reasons, QDs are explored for their potential high IQE. However, their active area is small, so the throughput is also small. Current LEDs are typically quantum wells (QW) or multi-quantum wells (MQW) because they have a larger active region, and thus a higher output power.

4.2.5 Nanowires

Currently, most LEDs are planar MQW structures, however they suffer from a large density of defects. III-nitride nanowires can be nearly defect-free with a significantly reduced PZE field [86]. The wires can be grown on a variety of substrates, including silicon and sapphire, with minimal threading defects. These substrates are much cheaper than GaN. The lateral structure allows for strain relaxation due to the high surface to volume ratio. This is very important because it reduces the QCSE leading to a higher efficiency.

4.3 Phosphor-free solid state lighting using InGaN/GaN nanowires

Since InGaN LEDs with emission in red, green, and blue have all been demonstrated, the next step is to incorporate them together on a single chip; they can be arranged side by side in a pixel-like grouping. Since they require different growth conditions, this is a multistep process. Monolithically grown nanowires with InGaN dots representing full spectrum control, were demonstrated by Wang et al.[15]. First, a nanowire set with blue emission is grown; then it is protected in order to grow the next set. This approach has the advantages of offering complete color control, but it is a multistep process.

Other designs incorporate emission from the entire spectrum in single wires. White light emission was demonstrated in InGaN/GaN disk-in-nanowires [16,87]. The different emission wavelengths were achieved by varying the temperature while the InGaN disks were being formed. As the temperature is raises, the indium incorporation also increases leading to a red shift in the emission. Another similar dot-in-wire structure used a tunnel junction, and was able to run the white LED from an AC source [88].

A third strategy is a single step process for monolithically grown single InGaN/GaN dot-in-nanowire LEDs capable of creating an RGB pixel with only 3 nanowires[17]. The wires are grown using selective area growth, which determines the diameter of the wires. The diameter of the wire determines the diffusion of In, and therefore the spectral emission. Sekiguchi et al. demonstrated this technique in 2010[89]. Ra et al. was the first to achieve emission in the entire spectral range with a single growth step[17]. These wires will be discussed further in the next section, as samples grown with a similar structure are the focus of the next two chapters.

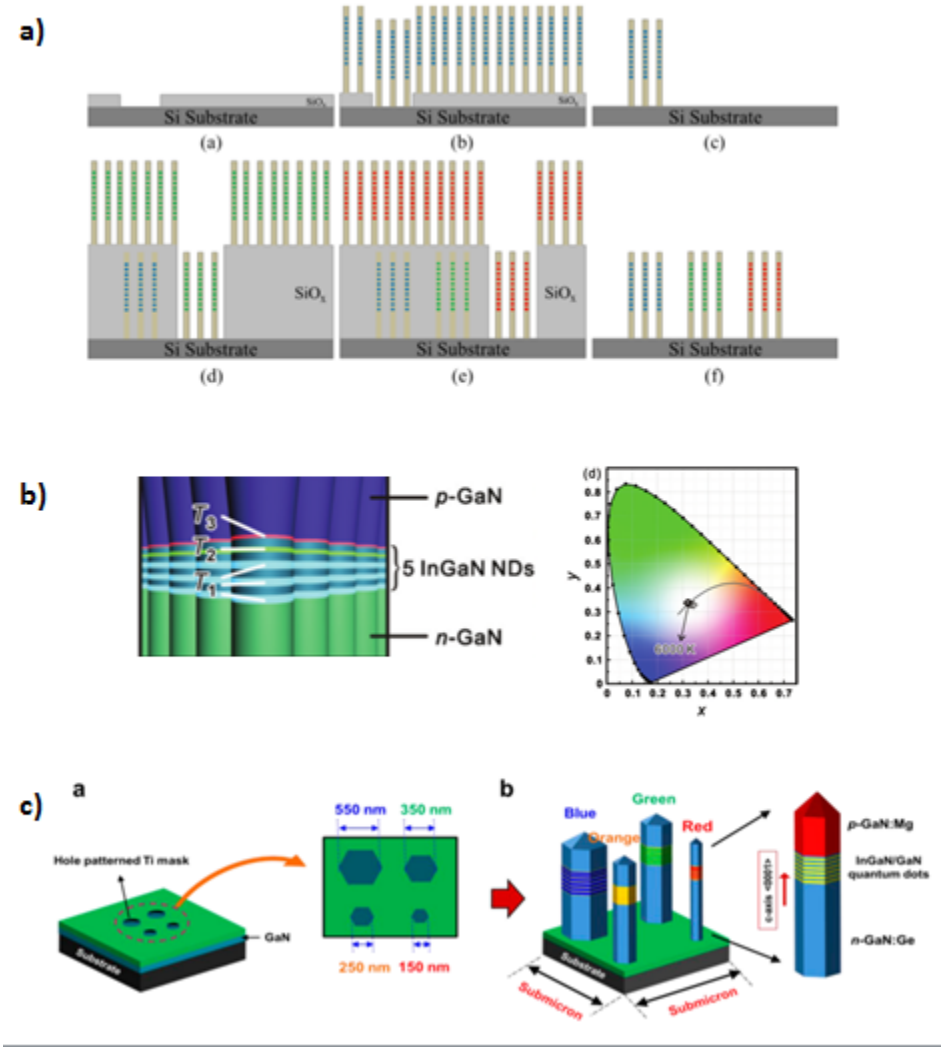

Figure 4.5: Three processes to create monolithically integrated white LEDS. (a) the multistep process of growing nanowire sets with emission in the blue, the red and the green[15]. (b) Axial growth of disks- in- nanowires which have a broad emission created by changing the temperature during the growth to form disks with emission peaks across the visible spectrum[16]. (c) Selective- area growth nanowires that are monolithically integrated and grown in a single step process. The diameters of the wire dictate the emission peak[17].

4.4 InGaN Dot-in-nanowire samples

The samples explored in this thesis were grown using similar growth parameters as those in Ref[15,17]. The samples investigated in this thesis were grown by the same grower, Dr. Ra in the Zetian Mi research group.

4.4.1 Selective area growth nanowires

The growth techniques and parameters for InGaN NWs vary considerably, and so do the resulting samples. In contrast to self-organized wires, which form randomly on the substrate at a nucleation site, selective area growth utilizes a set pattern etched into a mask. For our samples, e-beam lithography was used to etch a pattern in a thin layer of Ti. The wires were then grown in a molecular beam epitaxy (MBE) system. As can be seen in the SEM images, the NWs are quite uniform and can be grown with a variety of diameters.

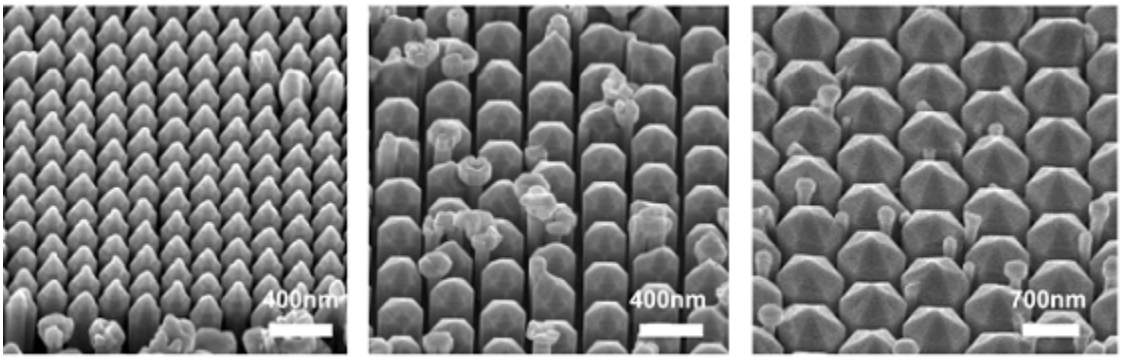

Figure 4.6: SEM images of the selective area growth nanowires with approximate diameters of 195 nm, 300 nm, and 700 nm, from left to right. Images captured by Yong-Ho Ra.

The indium concentration in the ternary composition is what determines the bandgap, and hence the wavelength output of the LED. In self-assembled growth the diffusion of In is mainly controlled through the substrate temperature; the nanowires with blue emission and a lower In concentration are grown at a higher temperature,

and as the temperature is lowered, the emission of the nanowires shifts to red. With the selective area growth, there are two different parameters which can be controlled: the diameter of the nanowire and the spacing between the nanowires. The temperature is still key to the growth, but since the nanowires are all grown at the same time, it is not a control used to shift the emission.

4.4.2 Top-down methods

Samples with similar characteristics have been demonstrated using top-down methods of creating nanocolumns or nanopillars by etching a planar multi-quantum well [18,90]. This process also uses a mask and has complete control over the diameters and spacing to the columns. They can be patterned to have diameters of 110 nm and larger. For comparison, the selective area growth samples investigated here have diameters ranging from 195-700 nm.

Just like in bottom-up growth, the nanocolumn demonstrates an increased PL efficiency when compared to the planar structure. This is credited to a decreased QCSE, as the strain is relaxed, and an increased confinement. Both top-down and bottom-up processes have their advantages and they provide an important point of comparison for the other. The PL emission of these structures will be compared to the PL of the InGaN dot-in-nanowire samples in the next chapter.

4.4.3 Dot-in-nanowires

A schematic of the growth is shown in Figure 4.8; the substrate is a commercially available GaN-on-sapphire substrate. The GaN selective area wires are then grown. Then the heterostructure is created with fifteen layers of InGaN/GaN. This is an important point of discussion, because as the schematic is drawn, it appears that there is only one dimension of confinement, the vertical direction, and that would create quantum wells, also sometimes referred to as disks. However, studies into the

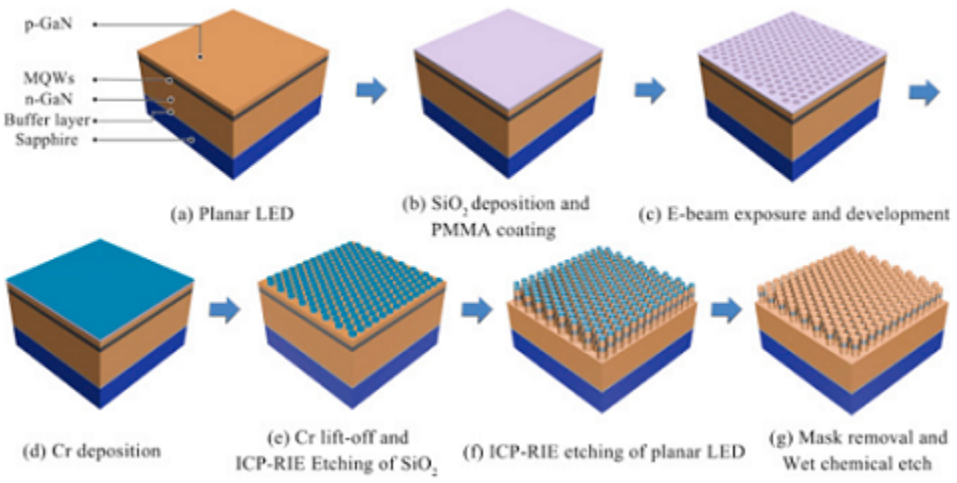

Figure 4.7: Flowchart showing processing steps for the fabrication of InGaN/GaN MQW-based NP LED array structure using the top-down method[18].

growth formation have revealed that quantum disks actually form multiple dot-like structures within each "layer" of InGaN [17,87]. These dots have also been referred to in literature as In-rich clusters and quasi-quantum dots[20].

Figure 4.9a shows the high-angle annular dark-field (HAADF) atomic-number contrast images. It is clear that the indium, which shows up as the light color in the image, does not extend to the full width of the wire, but instead is in a small area that does not come close to extending to the NW surface. This is also visible in Figure 4.9b, which is an elemental map from electron energy- loss spectroscopy (EELS). The red arrows show the direction of growth. For the two smaller diameter wires, the growth is axial, along the c-plane. As the wire diameters increase, the dots begin to form on the semi-polar planes. As was discussed, this should lead to a reduction of the QCSE shift due to polarization fields for the larger diameter wires.

4.4.4 Substrate

The nanowires can be grown on a variety of surfaces; however, the growth parameters must be optimized for each substrate material. Ideally, the optical pump-probe measurements would be done in transmission simply because it avoids the possible

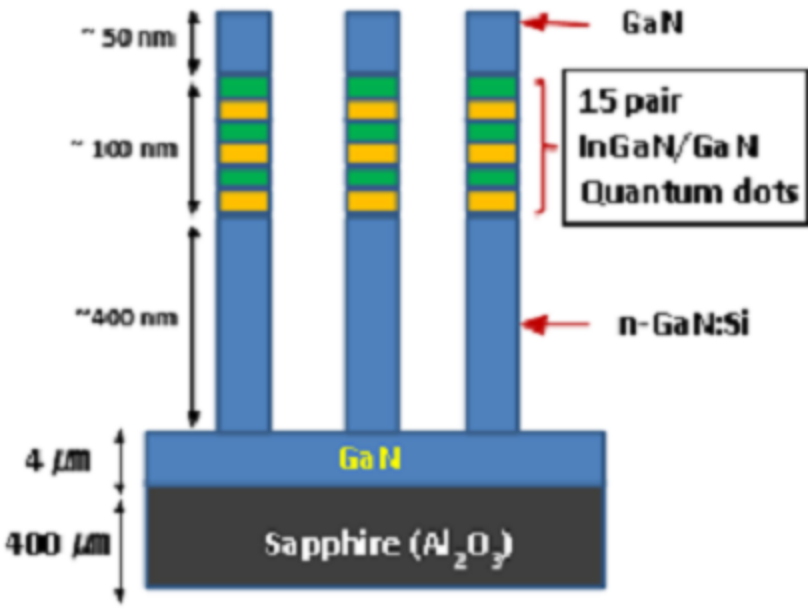

Figure 4.8: Schematic of the dot-in-nanowire growth created by Yong-Ho Ra

interference of multiple reflections. The sample growth process was initially optimized on single polished sapphire. For this work, double polished sapphire substrates were requested in order to perform transmission experiments. This would seem like a trivial exchange, since the growth surface is the same, but the temperature of the growth in the MBE is monitored by a laser incident on the backside of the substrate. When the double polished sapphire was used, it changed the calibration necessary for the temperature sensor. Due to this, the double polished sapphire samples never achieved the same emission efficiency as the samples in the previous work [15,17] and exhibited considerably broader PL spectra. However, they still are good samples that are representative of this type of growth, even if their emission is lower.

Two samples will be explored in this work. The first are patterns grown on a double polished substrate. These samples showed a fairly broad photoluminescence (PL) when compared to previous single polished sapphire growths. The transient absorption measurements on the first sample were taken in transmission. The second

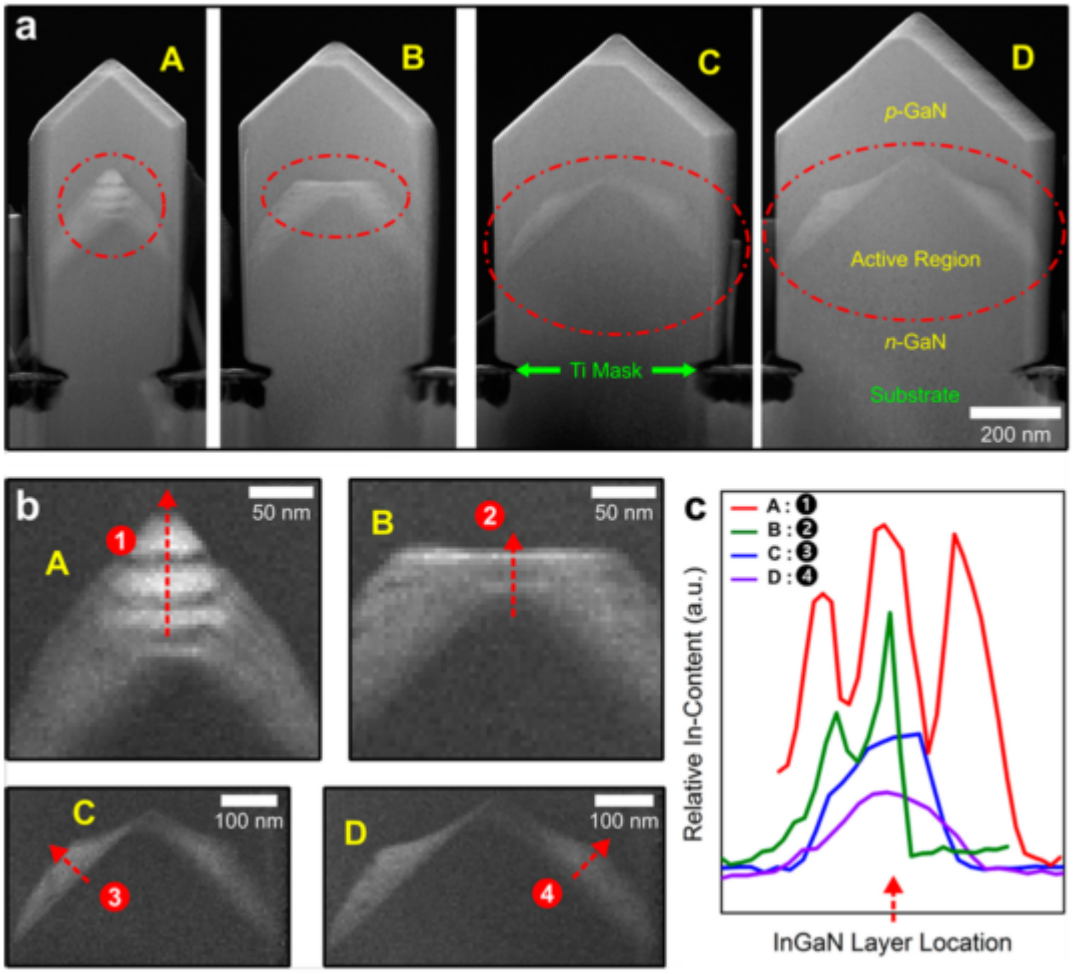

Figure 4.9: (a) A STEM-HAADF image for InGaN/GaN dot-in-nanowire structures with different diameters grown on GaN template on sapphire substrate along the $< 11\bar{2}0 >$ zone-axis. The active region of nanowires with diameters of ˜320 nm, ˜420 nm, ˜500 nm, and ˜595 nm are labeled as A, B, C, and D, respectively. (b) High-resolution STEM-EELS maps of the In-distribution of active regions A, B, C, and D normalized to the sample thickness. Line profiles were integrated along areas as marked by the dashed red line in each active region. (c) Elemental profiles of relative In- content derived from EELS analysis along line 1 in active region A, line 2 in active region B, line 3 in active region C, and line 4 in active region D, showing higher In-content in smaller diameter wires.[17]

sample is on a single polished sapphire substrate and so the transient absorption measurements were collected in reflection. The PL of the two samples, and their implications, will be discussed in the next chapter.

CHAPTER V

Photoluminescence of InGaN/GaN dot-in-nanowires

From the structural characterization presented in the previous chapter, is is apparent that the InGaN nanostructures considered here cannot be thought of as simple QWs of QDs. Instead, the structures consist of nonuniform QD regions embedded in the NWs. As a result, the PL emission does not have the simple spectra expected for idealized QWs or QDs. In order to explain the PL of our samples, a framework of recent literature will first be discussed.

5.1 Phase separation

In 2005, Park et al. demonstrated that self-assembled QDs would form on a roughened GaN substrate due to an increased phase separation of the InGaN layer[19]. This was due to the indium forming clusters to reduce the strain due to the lattice mismatch between the GaN substrate and the InGaN layer. This is the same effect that creates QDs in the dot-in-nanowire structure instead of disks.

The PL from the phase separated structures typically shows multiple peaks; an example is shown in, Figure 5.1. The lowest energy peak is attributed to emission from the dot and the higher energy peaks are due to a surrounding matrix of InGaN

with lower indium concentrations that the QD. Both of these are redshifted from the PL that would be emitted by the InGaN if it formed a uniform flat layer. This is not surprising since the flat layer would have the indium distributed in a lower concentration. A multi-peak PL has been reported for top-down MQW InGaN nanowire structures[18,90] and InGaN MQWs on a planar surface[18–20].

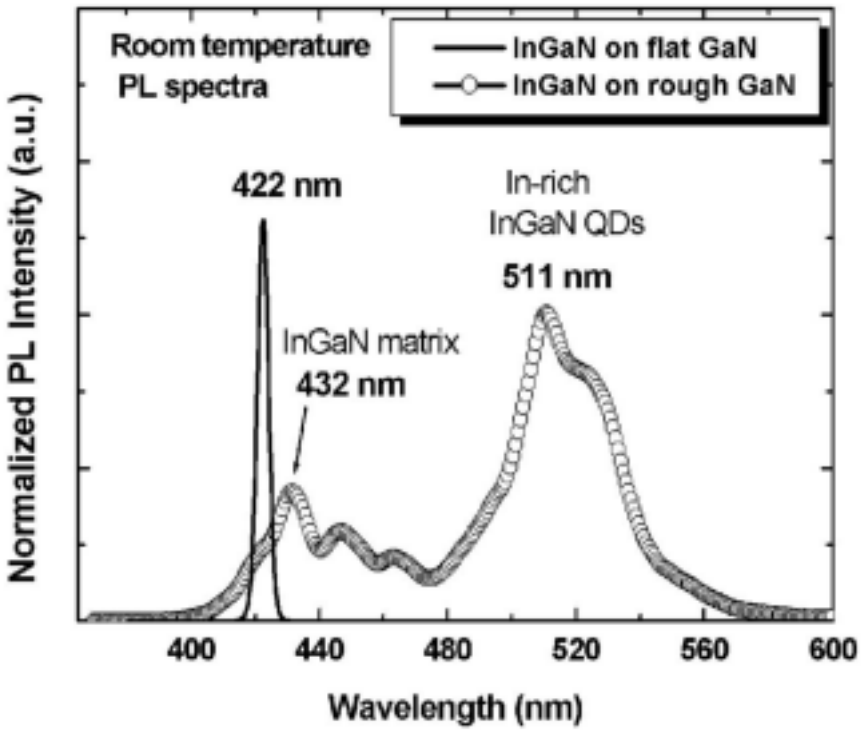

Figure 5.1: The room temperature PL of a flat InGaN film, peaked at 422nm, and the two peaks from phase separated InGaN dots which formed on a roughened surface. The higher energy peak is due to the lower In-concentration InGaN matrix. The higher energy peak is from the strain relaxed In-rich QDs. A CW source was used for excitation[19].

5.1.1 Temperature dependence

The relative strengths of the peaks will shift with temperature and excitation intensity, as can be seen in Figure 5.2. The PL measurements are for InGaN MQWs on a sapphire substrate. The peaks due to the QDs and the matrix are designated P_D and P_M, respectively. At low temperature, the P_M peak is large because the

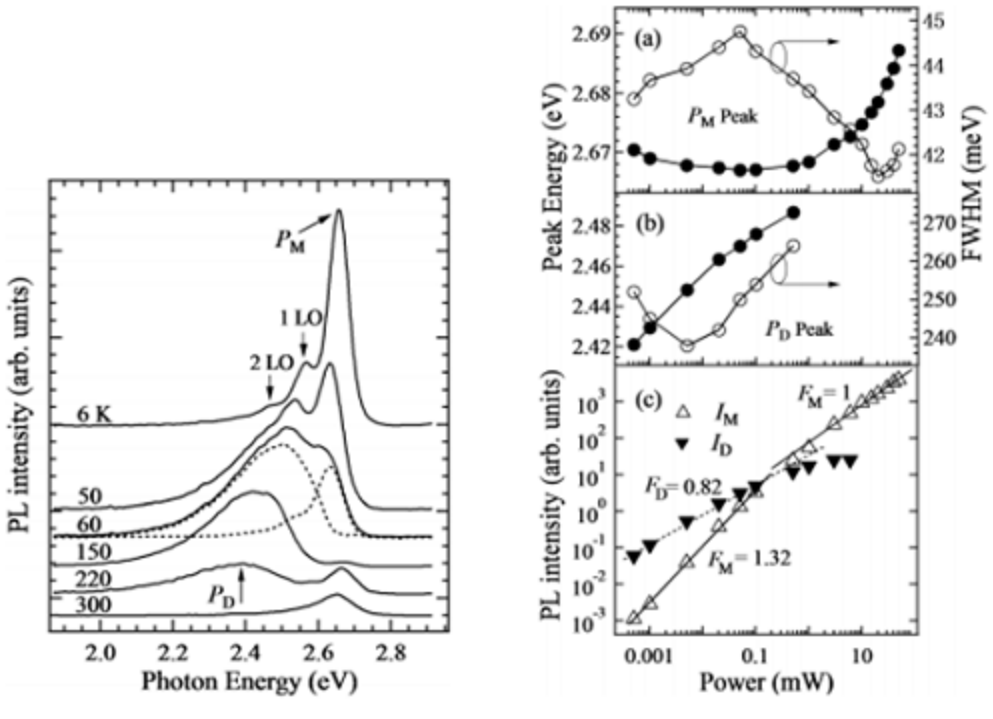

Figure 5.2: (a) the temperature dependent PL from MOCVD grown InGaN/GaN MQWs. The peak from the dot emission is labelled P_D. The peak from the matrix emission is labelled P_M. (b) the emitted energy of the peak and FWHM, for both the dot and the matrix as a function of the incident power. The PL intensity for the dot and matrix peaks as a function of incident power. The source was a CW 405 nm laser with a spotsize of 170 um[20].

electrons are all trapped in the matrix states and radiatively recombine before they can relax into the deep QD potential well. As the temperature rises, the electrons relax into the dot states via phonon interactions, so the PL shifts to the dot peak. As the temperature rises past 100K, nonradiative processes begin to dominate and both peaks are severely suppressed[20].

5.1.2 Intensity dependence

The PL spectra from ref.[20] shown in Figure 5.2b were taken with a CW source at 150K, to reduce the non-radiative processes that suppress the PL at room temperature. With increasing intensity, both P_M AND P_D are blueshifted in wavelength.

This is due to the screening of the PZE as the number of carriers increases. They both also start to saturate at increased powers; the dots saturate first as the dot states fill, and the QD DOS is lower than the DOS of the surrounding matrix.

5.2 PL from broadband emitters

Shimosako et al. investigated the localized states for selective area nanowires grown using the process described earlier that was developed by Sekiguchi[21]. This is the same process of growth for our samples. Shimosako specified that two types of growth are possible; one with a conical tip on the end of the nanowire, as seen in Figure 4.9, and one that has a flat top. The conical cap shows emission at two PL peaks, one attributed to the well-like regions, and one attributed to the dot-like structures; the flat top only shows emission from the well-like structures. Shimosako does not specify the reason behind this. The PL in Figure 5.3 is due to nanowires only exhibiting the well-like emission with a pulsed source. The structure includes InGaN/GaN MQWs as well as a InGaN/GaN superlattice.

The PL from the Shimosako samples looks distinct from the other samples referenced so far. One key difference is that the emission is at a much lower energy than other nanocolumns or films cited; the emission extends to orange wavelengths. Also, the peak emission at room temperature does not shift with increasing incident power (instead of power, the vertical lines are designated by the number of carriers). The FWHM is also broader than that from a QD. This supports the idea that the PL shown is not due to dot-like states, but instead MQWs. Shimosako refers to them as localized states; instead of having a defined peak, the emission is very braod, so the electrons are captured by the localized fluctuations of In concentration/ The PL is even broader than the matrix states discussed in the last section.

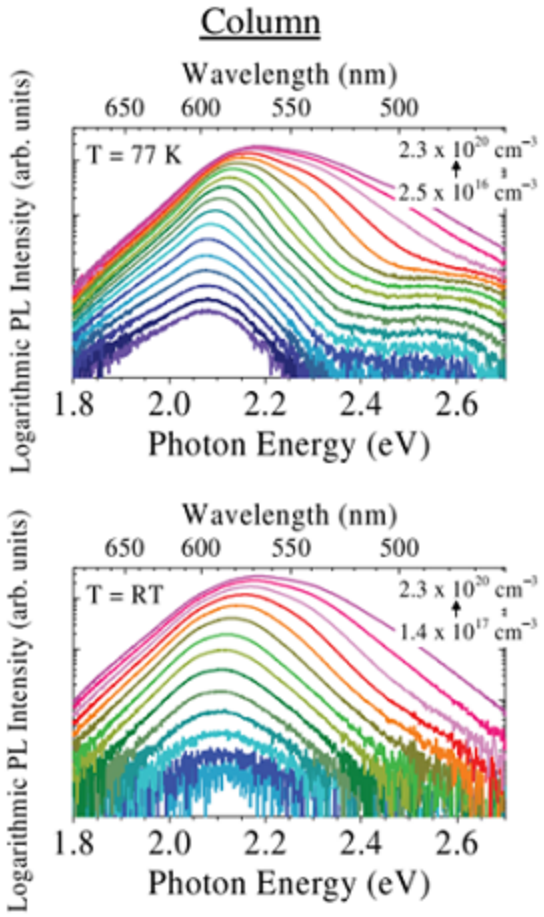

Figure 5.3: The carrier density dependence of the PL spectra for flat top selective area growth InGaN/GaN MQWs under pulse excitation at 77K and RT. The vertical axis is plotted on a logarithmic scale[21].

5.3 Photoluminescence for InGaN/GaN dot-in-nanowires

In our work, PL was collected using both CW and pulsed sources. The CW source was a 405 nm diode laser. The CW PL measurement was collected at McGill University, while the time-integrated pulsed PL was collected at the University of Michigan; this is important because the absolute value of the measurements cannot be compared between the CW and pulsed since the excitation densities were different. However, the shapes of the spectra as well as the relative emissions between the samples are important points of comparison. The PL emission for pulsed excitation

is shown in counts per second on the left axis, and the CW PL is shown in arbitrary units on the right axis. The pulsed source is the 400 nm second harmonic generation (SHG) from the RegA (250 kHz) and unless otherwise specified the incident intensity is 36 uJ/cm^2. If we assume that the nanowires absorb 1% of the incident light, then the approximate carrier density generated is 7x10^{11} photons/cm^2 per pulse.

5.3.1 Summary of sample parameters

- Selective area growth: a mask and e-beam lithography were used to predetermine the size of the wires. In SEM photos, the wires are very uniform.

- Single growth: the two samples, one on single polished sapphire and one on double polished sapphire, each had different patterns of nanowire diameter sizes that were grown simultaneously under the same conditions.

- Dot-in- nanowires: the MBE growth conditions were such that dot-like indium structures were formed in the green emitting sample, the other white light sample shows an inhomogeneous PL, so it is unclear if there are dots, but they are washed out by other factors.

- Ensembles: In order to have a strong signal for transient pump-probe measurements, many emitters were required. Each pattern has more than 10^5 wires, and each wire has many dots. This changes the nanowire growth, so they may not be directly comparable to the single wires studied by HAADF[17]. The indium diffusion into an individual wire be influenced by the presence of the neighboring wires and the ensemble will have variations. Both of these will lead to a broadened PL.

5.4 White light nanowire sample

Figure 5.4 shows the pulsed and CW PL for patterns of wires with diameters 195 nm, 300 nm, and 700 nm, respectively. The first observation from the PL is that emission from all three samples is broad, which is not what you would expect from a quantum dot. From a single dot, the DOS dictates that there should be a distinct transition, leading to a delta-like emission. However, this is only true for a single dot. For a broad PL spectrum there are two possible explanations. First, it is possible that this sample growth is not as dot-like as the growths analyzed by HAADF, and instead they have a wider emission since the DOS has spread to something more like what would be expected from a well. The other explanation is that the broader PL is due to the large ensemble of dots; each dot can individually have emission at a narrower wavelength, but this narrow-emission behavior is washed out by the inhomogeneity of the ensemble. While there are many dots involved, it is most likely that the broad emission is due to QW-like states. The emission is very similar to that of the selective area growth nanocolumns in the previous section. The emission could also be broadened by localization of states caused by defects. Therefore, since this sample doesn't seem to display QD-like behavior, this sample will be called the white light (WL) nanowire (NW) sample

The second observation is that the pulsed PL has a strong oscillation in the spectra. Similar oscillations have been seen due to Fabry-Perot effects in InGaN/GaN heterostructures[91]. However, this should not be the case in this instance, since the oscillations don't appear under CW excitation, and the period is not consistent with the length of the structure. At this time, we don't have a good explanation for the structure on the spectra.

Typically in multi-quantum wells (MQWs), the pulsed PL is blueshifted when compared with the CW PL, often by 10 nm or more[25]. This shift is attributed to the screening of the PZE field in conjunction with the QCSE. The expectation

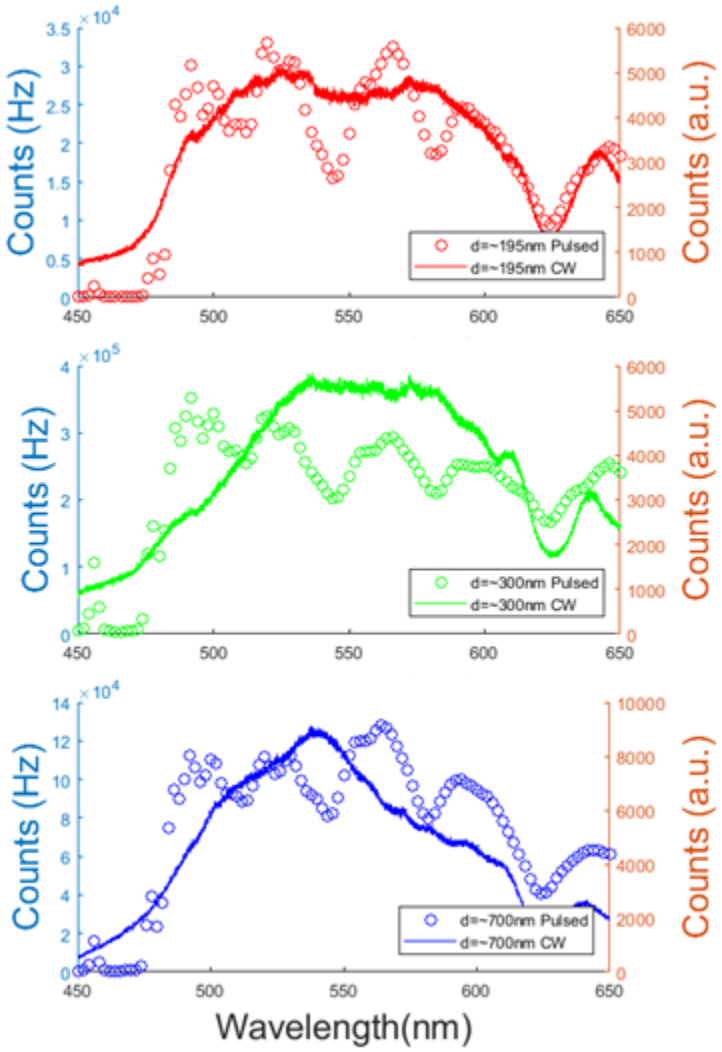

Figure 5.4: PL spectra of the WL NWs sample, with selective area grown nanowires with diameters of 195 nm, 300 nm, and 700 nm. The spectra were collected with pulsed excitation (left axis) and CW excitation (right axis). The relative amplitudes between the pulsed and CW intensities are not comparable, because different detection systems were used.

is that the shift would be smaller in the case of a QD, since the confinement in three dimensions maintains a larger wave function overlap, as compared to single-dimension confinement in wells. Even though the PL from the CW and pulsed sources overlaps very well, this cannot be directly ascribed to QD behavior, since the PL is much broader than the PL of QDs. Instead, we ascribe the lack of a blueshift to inhomogenous broadening which can be caused by defects. The lack of shift is even more surprising considering that the emission is in the 490-650nm range where the PZE field would be greater. As was discussed earlier, it is particularly difficult to get strong emission at green and yellow wavelengths, because the higher In concentration leads to strain which increases the PZE.

When comparing the three samples with different diameters, a spectral shift is expected. The diameter should influence the indium concentration of the growth, however the mechanisms are still being studied. Ra et al. showed that for a single wire growth with a dot-in-wire structure, the spectrum should be blueshifted as the diameter increased[17]. This was attributed to the longer diffusion length of Ga compared to In, leading to a lower concentration of In. This same shift was demonstrated for arrays. However, ensembles of InGaN nanowires also grown by selective area growth were shown to exhibit a redshift as the nanowire diameters increased[89?] . The sample measured in Figure 5.4 has ensembles of selective area growth dot-in-nanowires with diameters of 195 nm, 300 nm, and 700 nm. However there is not a notable shift in the spectrum. This emission peak and FWHM are similar to PL of the nanocolumns in Ref[21], which also had a well-like response from the InGaN matrix. Their explanation is that the PL measured is originating from the well-like structures of the matrix; this would account for the broad spectrum, but it does not account for the lack of a spectral shift.

The peak at 492 nm in Figure 5.4 is visible, not distinct from the rest of the spectrum. However, as shown in Figure 5.5 increasing the incident power shows

that the peak does not scale with the rest of the spectrum. The entire spectrum is not shifting to wavelengths that are not present at lower powers, but the relative weighting of the emission changes. The maximum intensity of the PL at 494 nm and 566 nm both show saturation at higher powers, but the 566 nm saturates much faster. This saturation is expected as it occurs for all LED structures. It is termed the efficiency droop and has been the focus of many research projects.

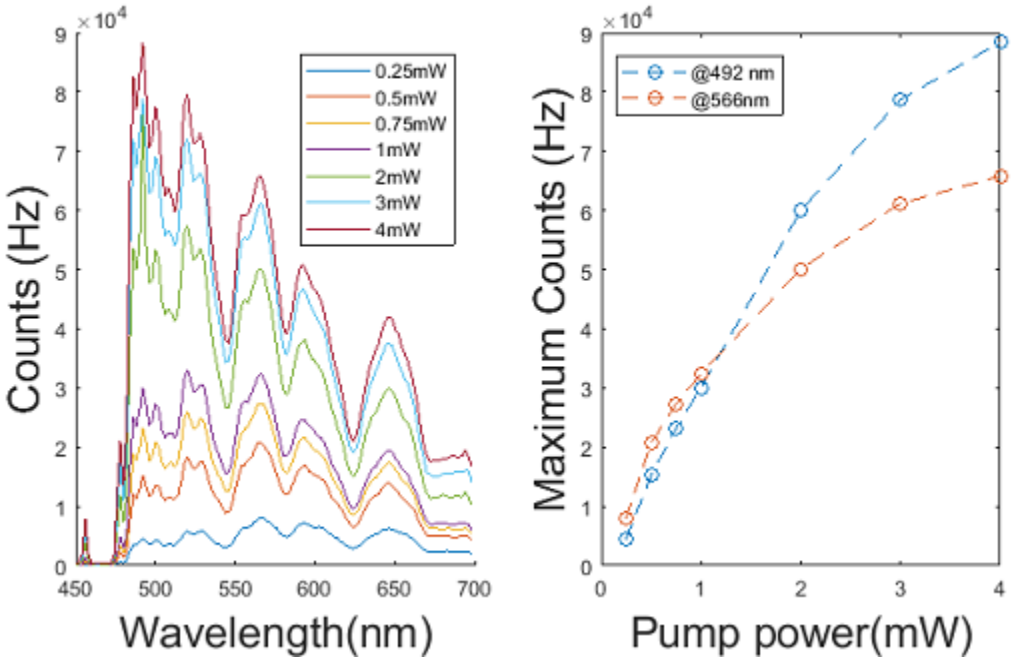

Figure 5.5: (a)The power dependent spectra for the WL NWs sample with a pulsed excitation. (b) The power dependent peaks at 492 nm and 566 nm.

5.5 Green dot-in-nanowire sample

From the PL, it is immediately obvious that this sample is quite different from the WL NW sample. The emission is much narrower with a FWHM of 15-20 nm for the CW spectra. This sample was grown to emit around 500 nm; two patterns were used to create wires with approximate diameters of 225 nm and 235 nm. The PL for the green dot-in-nanowire sample was taken under the same conditions as the PL for the WL NWs sample.

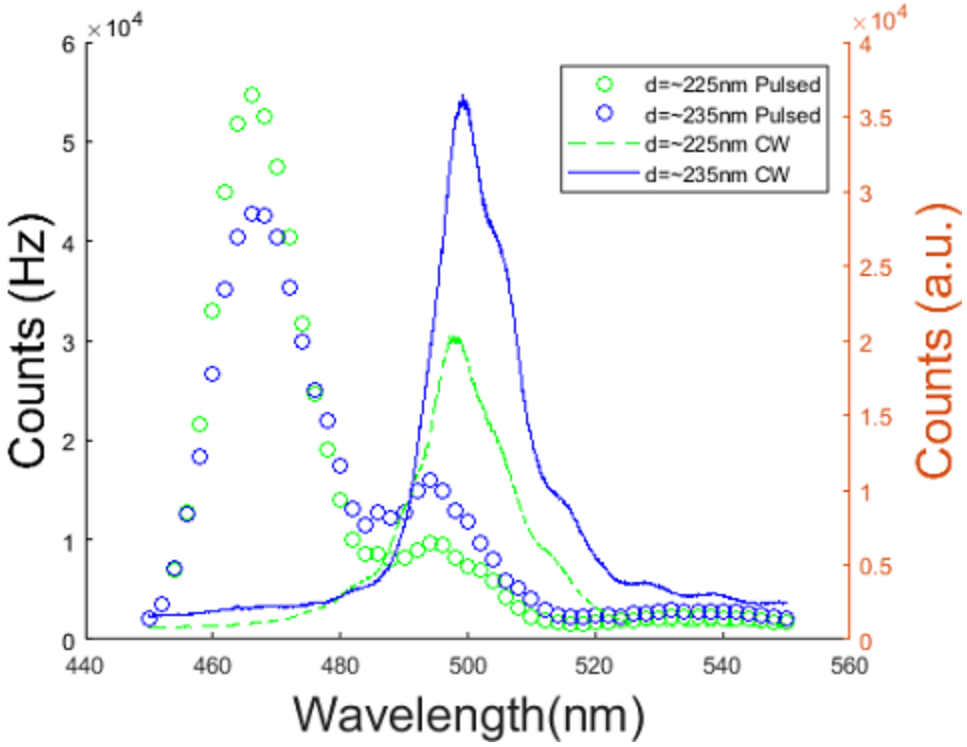

Figure 5.6: PL spectra of the green dot-in-nanowire sample, with selective area grown nanowires with diameters of 225 nm and 235 nm. The spectra were collected with pulsed excitation (left axis) and CW excitation (right axis). The relative amplitudes between the pulsed and CW intensities are not comparable, because different detection systems were used, and the excitation densities were different.

At first glance it may seem like the whole spectrum for the pulsed excitation is severely blueshifted with a peak at approximately 466 nm. However, this shift is too large to be accounted for by the PZE field. There are two separate peaks with separate origins; the 494 nm peak is the PL emission that is only slightly blueshifted from the 500 nm response, while the 466 nm peak is due to the InGaN matrix. It is interesting to note that the relative amplitude between the two samples is matched for the pulsed PL at 494 nm and the CW, but then switched for the 466 nm peak. It is important to remember that the scaling of the pulsed PL and the CW PL have no relationship; they are normalized for this plot.

A 450 nm long pass filter was used to filter out the 400 nm pump from the spectrometer; this was not a precautionary choice. Without it, even in reflection,

the 400 nm light is strong enough to overpower the signal by an order of magnitude. However, this should not impact the shape of the spectrum since at 452 nm (the second data point in the scan), the filter is still passing 80% of the light, but the signal is near zero.

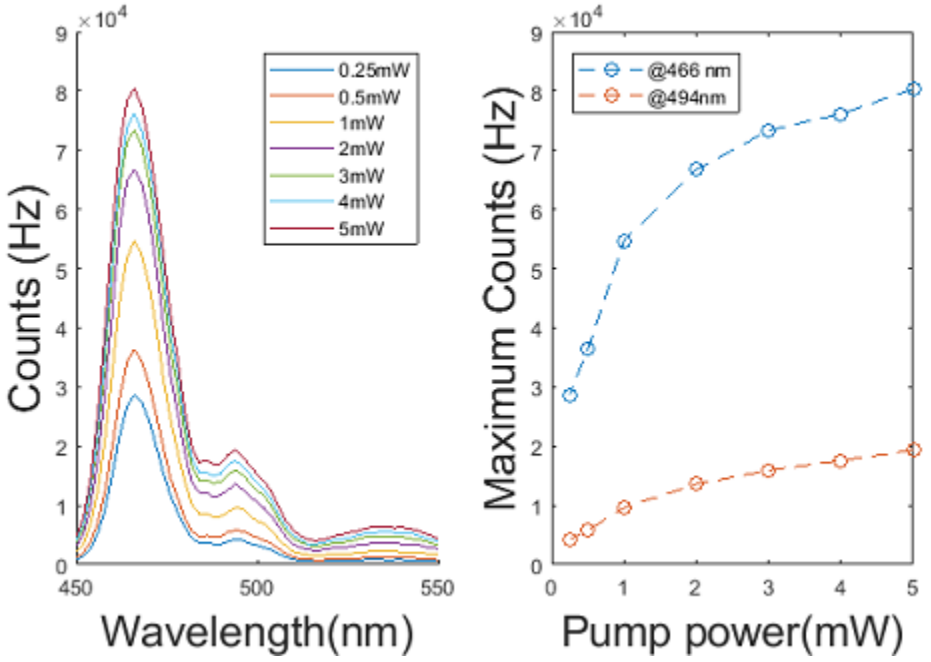

Figure 5.7: (a)The power dependent spectra for the green dot-in-nanowire sample with 225 nm diameter nanowires for a pulsed excitation. (b) The power dependent peaks at 466 nm and 494 nm

Power scaling measurements were also taken for these two samples, with both similarities and differences when compared to the WL NWs. There is clear saturation for both peaks as the power is increased. The initial scaling appears to be linear with saturation beginning to occur around 1mW. The saturation is very similar to what was observed with the WL NWs.

Scans were taken with a maximum incident power of 5 mW, 180 uJ/cm^2. After the maximum intensity of 5 mW, the power was then decreased and a recoverable bleaching effect was observed. The count rate at 1mW, was significantly lower than it had been before increasing the power. However, after an hour without any pumping, it had regained the original signal.

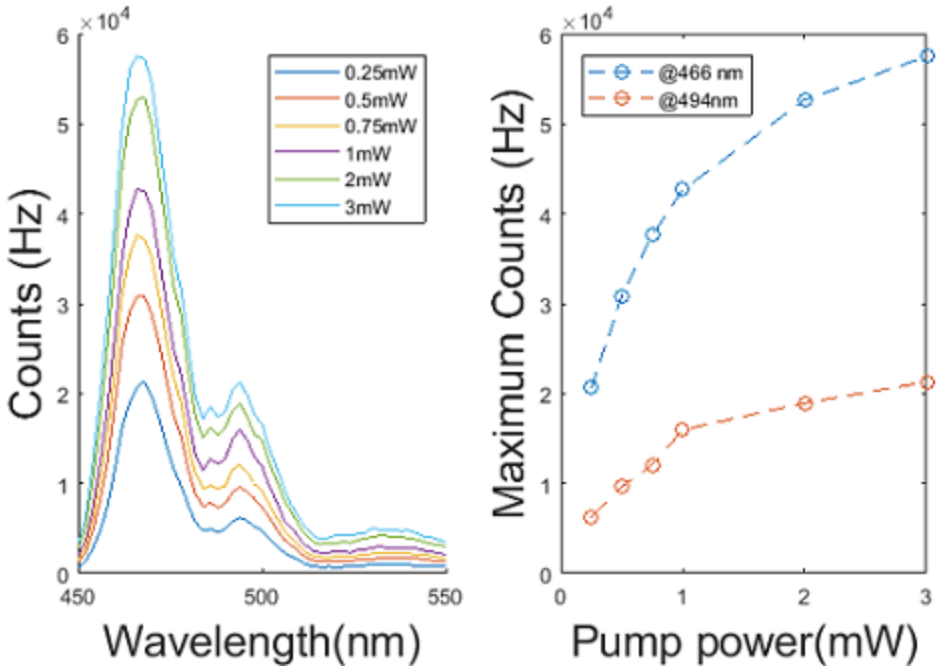

Figure 5.8: (a)The power dependent spectra for the single polished sapphire sample with 235 nm diameter nanowires for a pulsed excitation. (b) The power dependent peaks at 466 nm and 494 nm

5.6 Discussion

The high concentration of carriers produced by the pulsed source revealed the matrix states in the green dot-in-nanowire sample. This can be illustrated by Figure 5.9. There are two possible causes, or they could both contribute to the effect. The first reason is that in the pulsed case, the PZE may be screened. The carriers in the matrix wells recombine and emit at 466 nm, instead of scattering to the dot states. The dot states are already well overlapped, so they only exhibit a small shift due to screening. The second possibility is that the QD states are filled and reaching saturation due to the large number of carriers.

In the room temperature CW case, Figure 5.9b, the electrons in the matrix states have enough energy that they quickly relax to the QD states. This process is so efficient, that only the QD emission is detectable. This supports the assertion that the green emitter does have dot-in-nanowires.

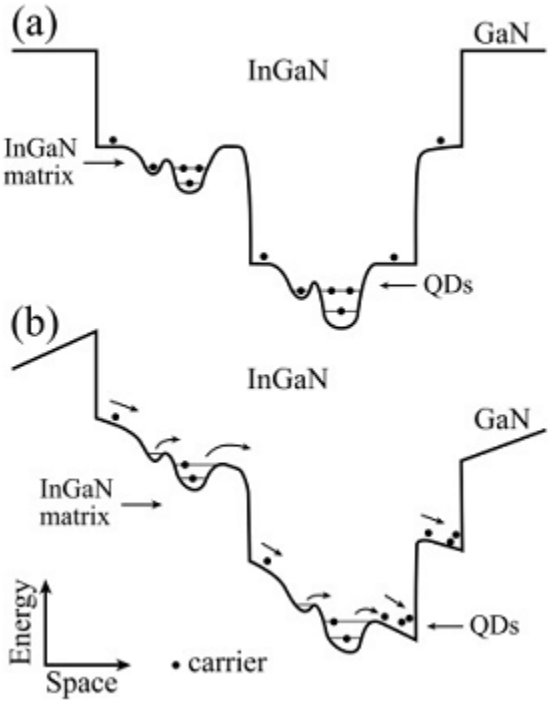

Figure 5.9: Diagram of the bandstructure and recombination processes for the dot and matrix states (a) without and (b) with the piezoelectric field[18].

CHAPTER VI

Electron capture and relaxation in InGaN/GaN dot-in-nanowires

Tunability across the entire visible spectrum has made InGaN/GaN heterostructures an essential component to applications in light emitting diodes (LEDs), lasers, displays, and sensing. Significant progress has been made in controlling the light emission through size and structure, including the use of quantum wells, quantum dots, and core-shell structures. As was discussed in Chapter 4, the InGaN selective area grown dot-in-nanowires have very exciting potential applications.

While these devices are bright and have good electrical properties, characterization of the carrier dynamics will help understand and optimize the device physics. The capture time and relaxation times are two key parameters for calculations of IQE droop[92]. Ozgur et al. used TRDT measurements to compared the capture and relaxation of electrons in an InGaN epilayer and an InGaN MQW; the relaxation in the MQW was much faster because the QWs captured electrons and removed them from the InGaN barrier faster than the recombination time[25]. The competing radiative and non-radiative lifetimes will determine the overall efficiency of LEDs and information about state lifetimes and relaxation processes can be useful for informing future laser devices. In this chapter, we present pump-probe measurements on the double polished sapphire substrate and the single polished sapphire substrate, each

with dot-in-nanowire patterns, with varied diameter and spacing.

6.1 Transient pump- probe measurements for semiconductors

Chapter 1 gave a brief overview of the differences in relaxation dynamics for metals and semiconductors. This was predicated on the idea that metals typically show Fermi smearing in response to excitation. In contrast, semiconductors have a bandgap that separates the conduction band from the valence band with the Fermi level in between. If the pump has sufficient energy to generate electron- hole pairs, then these will populate specific electronic states determined by the band structure and the DOS. The following derivation was adapted from Ref.[93] As a result of pumping, the absorption coefficient will change and can be equated to the change in the population of the electronic states.

$$\alpha(\hbar\omega, t) = \alpha_0(\hbar\omega)[1 - f_e(E_e, t) - f_h(E_h, t)] \tag{6.1}$$

Pump-probe measures the difference in the transmission with the pump

$$T = exp - \alpha(\hbar\omega, t)L \tag{6.2}$$

and the steady state transmission without the pump.

$$T = exp - \alpha_0(\hbar\omega)L \tag{6.3}$$

When combined the $\Delta T/T$ can be expressed as

$$\frac{\Delta T}{T} = exp[\alpha_0 L(f_e - f_h)] - 1 \tag{6.4}$$

The DOS of holes is much larger than the DOS of the electrons so the probability function f h, will be much smaller than the electron probability function. The hole's capture time is three orders of magnitude faster than the electrons[94]. In addition, the pump source is keep to a low enough fluence that $\alpha_0 L f_e$ is much less than 1.

$$\frac{\Delta T(\hbar\omega, t)}{T} \approx oLf_e(E_e, t) \tag{6.5}$$

From this equation we can see that the transmission is directly proportional to f_e as a function of time.

6.2 Experimental setup

This experimental setup, shown in Figure reffig:NWSetup shares many key components with the transmission set-up for TiN shown in Figure reffig:Pumpprobesetup, however it also has some differences to discuss. For the double polished substrate, measurements were taken in transmission, but the single polished substrate requires signal collected in reflection. When combining or splitting the beams, the dashed mirror lines represent dichroic mirrors; however the dashed line before the lens and sample is a pellicle used to split off a percentage of the signal for measurement. This does mean that a significant portion of the signal is lost as it continues down the pump path and the overall power available for the pump is lower (45% is reflected off the pellicle on the first pass and does not reach the sample), but this allows for collinear normal incidence measurements. The reflection mode is shown, but the transmission would simply take the signal going into the beam pump and direct it into the monochromator.

6.2.1 400 nm pump

Using 400 nm as the pump wavelength is convenient because it is:

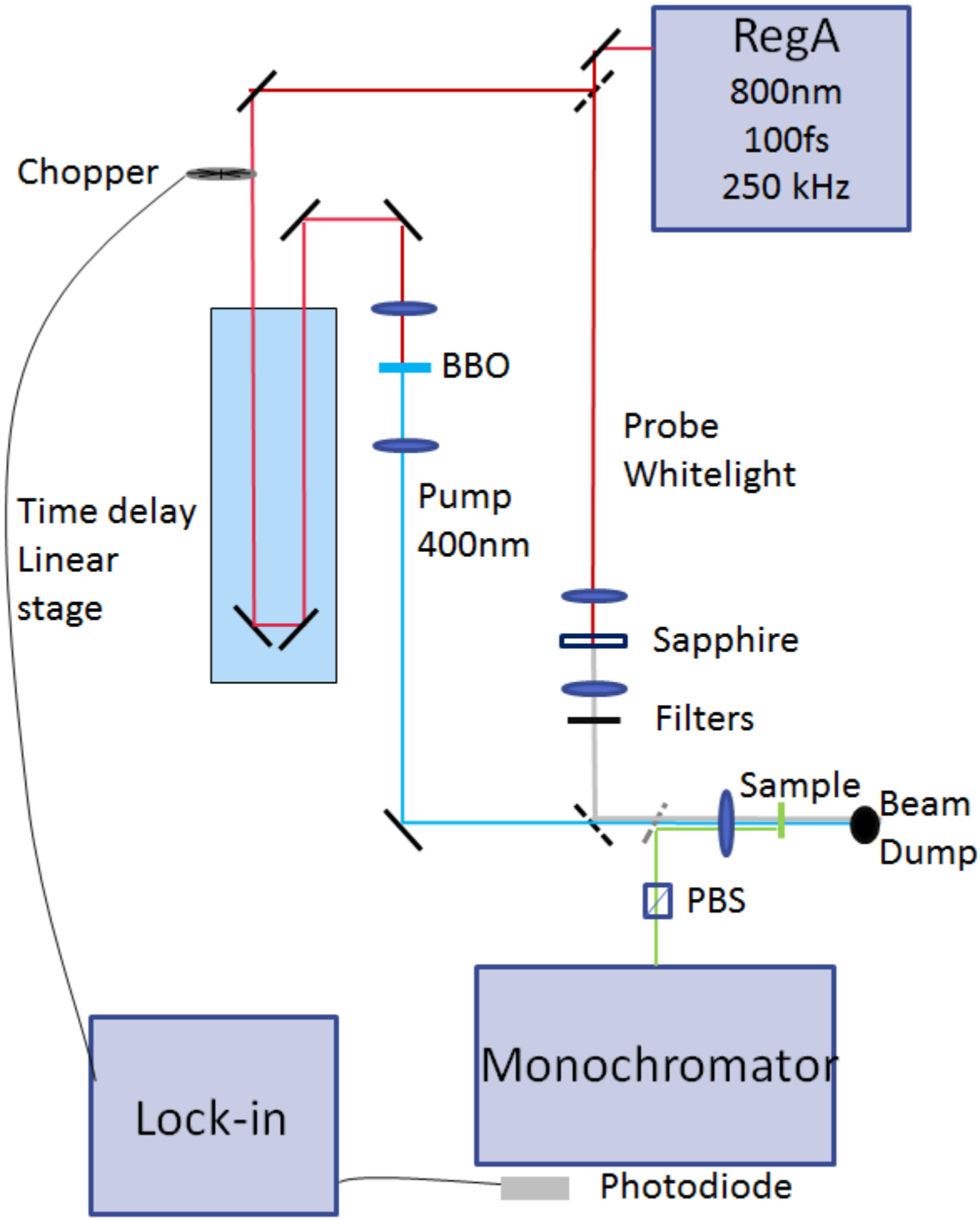

Figure 6.1: The experimental set-up for 400 nm pump and white light probe. This is also the setup used for the pulsed PL experiments.

- above the InGaN bandgap. The exact bandgap is a function of the confinement of the dots, as well as their indium concentration. This is not fully known for the samples studied, but their PL emissions show that the band edge is approximately 490 nm in the double polished sapphire sample(DPPS) and 495 nm for the single polished sapphire sample (SPSS).

- below the GaN bandgap. Just being below the GaN bandgap is not sufficient to avoid seeing a response from photoexcited carriers. Signals due to the AC Stark effect have been observed even 159 meV below the excitonic resonance at room temperature[25]. The excitation for GaN is 365 nm, but hot electron effects could persist for excitation up to 382 nm. Even when accounting for the FWHM of the pump, there should be no response from the GaN. Also, the strongest effects would still be higher energy than our detection range.

- easy to generate from a high power short pulsed 800 nm fundamental beam using second harmonic generation (SHG). Using a beta barium borate (BBO) crystal allows us to easily generate 30 mW of 400 nm light, measured after two color filters (BG 39) used to block unconverted 800 nm pump. The dichroic mirror that combines the pump and the probe paths is a 425 nm short pass, so it also acts as a filter. These filters are important because the fundamental beam is still quite strong after the generation. No two photon effects were observed in an initial trial, but blocking the residual 800 nm removes the possibility of parasitic effects.

Since the BBO crystal used follows Type I generation, the 400 nm beam polarization is rotated 90 degrees with respect to the fundamental. In the previous set-up, using an 800 nm source, a HWP was used to ensure that the pump and probe had orthogonal polarizations; it is no longer needed in the setup. A polarizing beam-splitter (PBS) is placed before the monochromator to block residual pump. Technically, the

monochromator should be able to filter out this based on wavelength, but since the measured signal is so small compared to the pump, this does help prevent background noise. A representative spectrum for the 400 nm pump is shown in Figure 6.2.

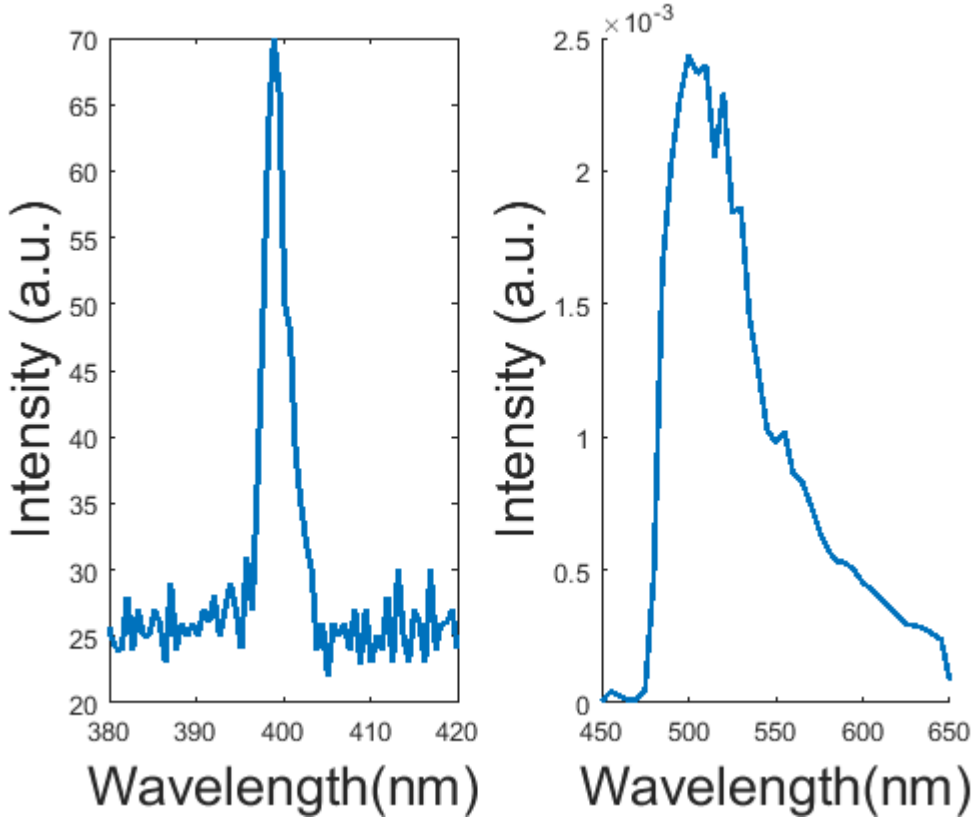

Figure 6.2: (a) spectrum of the second harmonic 400nm pump (b) spectrum of the white light probe after passing through a 450nm longpass filter and 650nm shortpass filter

6.2.2 White light probe

A small percentage of the fundamental 800nm beam is split off to create a white light (WL) probe. The 800nm is focused into a sapphire crystal and through combined self-phase modulation and self-focussing, generates a spectrum of light spanning from 400nm to 800nm. The generation is far from uniform and creates fluctuating intensity levels across the spectrum. The spectrum measured directly is shown in Figure 6.2b. This spectrum is collected after a 450nm long pass and a 650nm short pass filter, as

it is in the setup. It is not pictured in the set-up schematic, but there is also an iris immediately after the lens and before the sapphire; this iris is closed down if needed to create a stable WL continuum. This is recognized when there is a red corona around a WL spot. This is an important marker of stability because WL generation is dependent on many factors and easily will begin fluctuating or flickering if not set-up correctly. Both the WL and the SHG are very dependent on the pulse width and therefore the position of the compressor for the RegA.

Bandpass filters are placed on the WL path after the sapphire, to restrict this to the probe spectrum being investigated. In this case the filters only pass 450nm-650nm. This is in part because the intensity of the WL spectrum is much stronger at wavelengths longer than 650nm as the wavelength shifts towards the 800nm fundamental beam, and this would just put unnecessary heat into the sample. The intensity of the WL incident on the sample is set using a power meter, though this is only an estimate since the power meter is wavelength sensitive and the intensity of spectrum is varied. This is not very critical though since the power of the probe should be low enough so that it is not "pumping" the sample itself, but is only measuring it. Also, the critical information is the overall reflected power, R, of each wavelength, which is measured by the photodiode after the monochromator and recorded for each wavelength that will be used for a temporal ΔR scan. While the WL spectrum is peaked at 500nm, there is enough power in the entire spectrum to take differential reflectivity and transmission measurements, but the as the probe power is lower, the signal-to noise ratio is also decreased.

The samples also have spectral dependent reflection and transmission; Figure 6.3 shows the normalized spectra from the WL reflected from a mirror, the WL reflected by the SPSS, and the WL transmitted through the DPSS. While these do mimic the characteristics of the PL generated by the individual sample, the actual PL influence should be minimized since there is no pumping. The reflected and transmitted spectra

have been normalized to the WL spectrum.

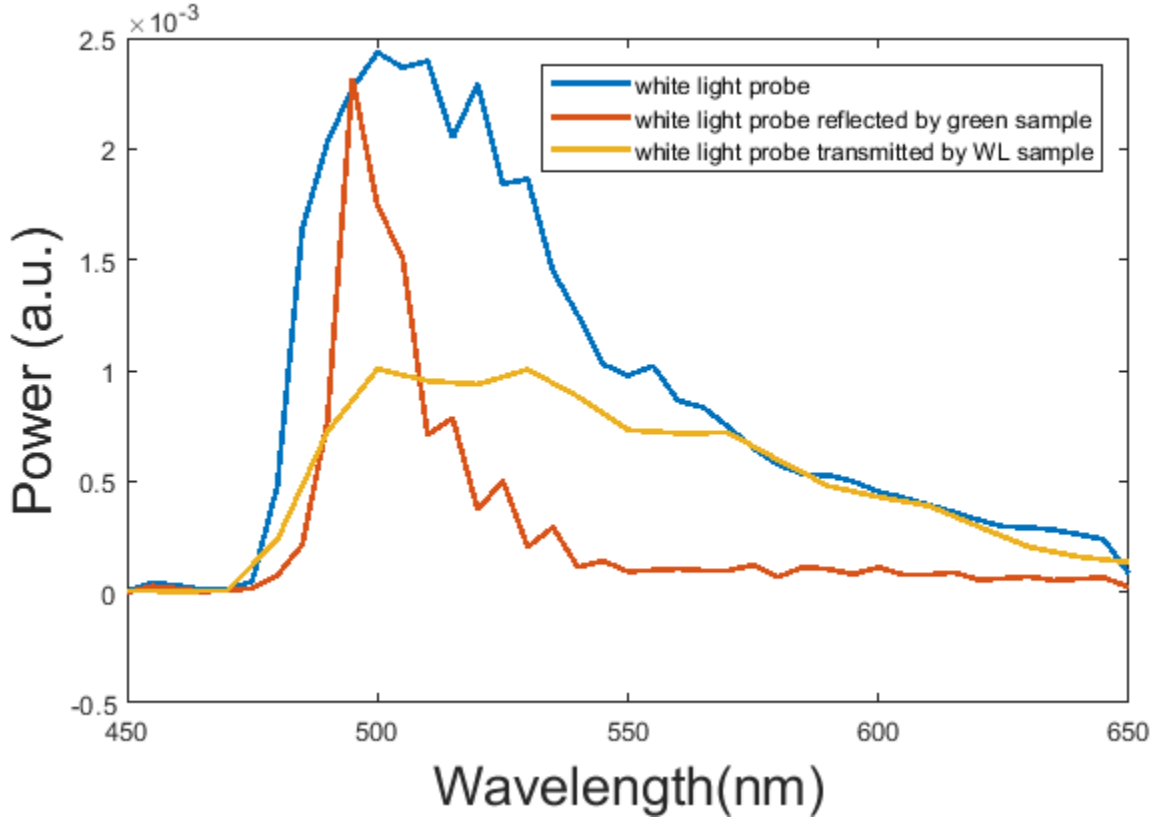

Figure 6.3: The transmission spectrum of the white light nanowire sample and the reflection spectrum for the green dot-in-nanowire sample are plotted normalized to the spectrum of the white light probe.

6.2.3 Monochromator

During these experiments the entire WL continuum is incident on the sample, but the monochromator selects out the wavelength measured as the probe. For the majority of these experiments, the slitwidths of the monochromator were set to a resolution of 2.5nm. This is fairly wide and allows for more signal. Even the fine wavelength scans are stepped at 5nms, so this is very reasonable.

6.3 Time-resolved differential transmission of white light InGaN/GaN nanowires

The PL of these three samples is plotted in Figure 5.4; the WL NW emission ranged from 490 to 650 nm, so this is the range that we initial took data in for the TRDT measurements. The WL probe is by no means constant in this regime; however, it is strong enough to have a reasonable signal to noise. The TRDT data for the three NW patterns, with probe wavelengths of 500nm, 550nm, and 600nm are shown in Figure 6.4. It might appear that the shape of the WL probe spectrum influences the amplitude of the signal, because the signal decreases with longer probe wavelengths for most cases. However, it is important to remember that the y-axis is the differential transmission divided by the transmission at that wavelength. Therefore, the amplitudes are real and not an artifact of the probe spectrum.

The most important observation about these scans is the fast decay. Regardless of the pump wavelength, the signal decays in nearly captured in a 15ps plot window. This means that the response being measured does not correspond to radiative recombinations. Typical radiative states are 500ps to several nanoseconds. The fourth panel of Figure 6.4 shows a slightly closer look at the risetime of the peaks with a 500nm probe. The risetimes in $\Delta T/T$ represent the capture rate; 0.33ps and 0.42ps are very fast. The implications of this will be discussed shortly.

6.3.1 Capture times

The first feature in the dynamics that will be discussed is the risetime, which shows the carrier capture time at the probe wavelength. The capture is a complex process that is not fully understood and has yet to be studied in different heterostructures or alloy concentrations in the InGaN dot-in-nanowire system. Electron capture can occur through electron-electron scattering, relaxation through localization caused by

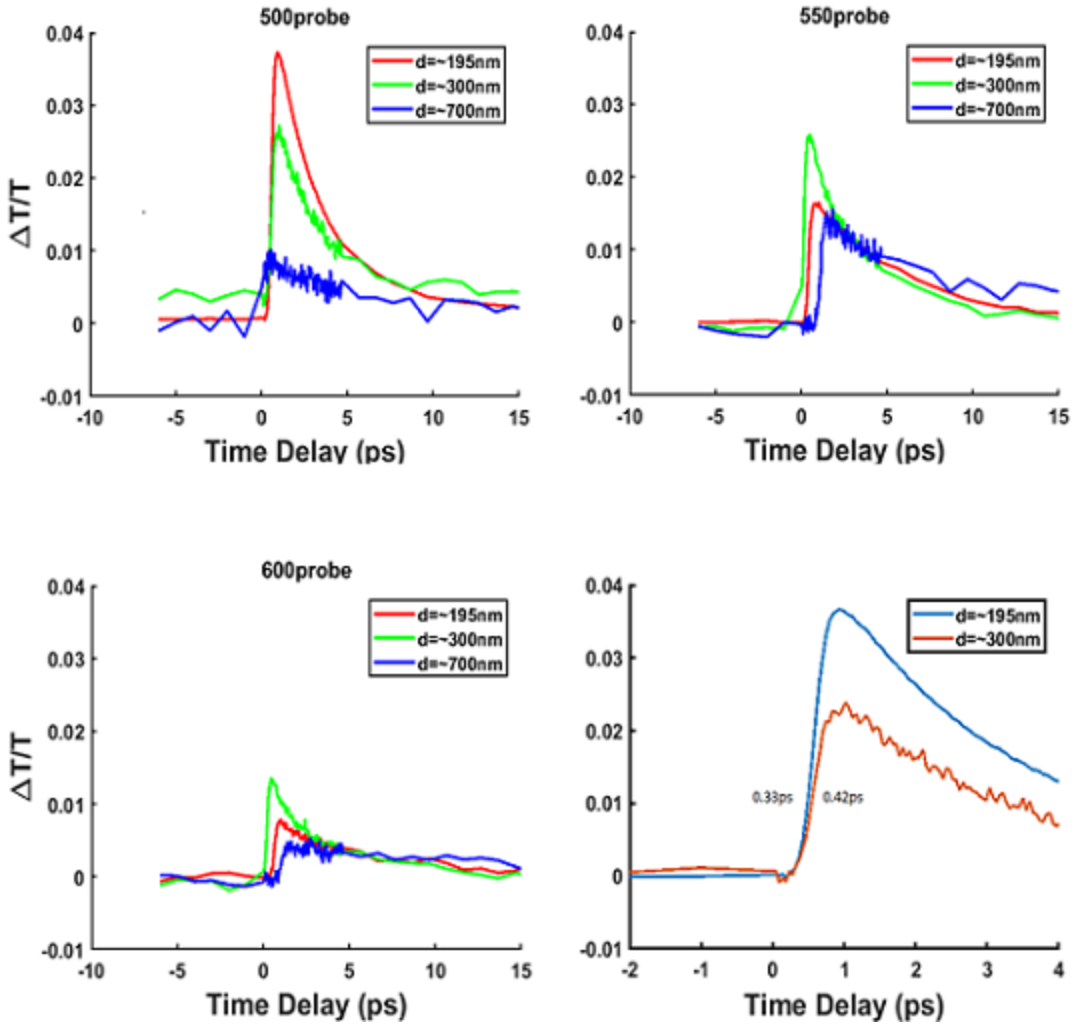

Figure 6.4: The TRDT scans for three diameter patterns on the white light nanowire sample at three different probe wavelengths, (a) 500 nm, (b) 550 nm, and (c) 600 nm. Quadrant (d) shows a close up of the risetime with the 500nm probe. The pump is 400nm and the fluence = 30 μJ/cm^2.

defects, and phonon emission[92,95]. Fast capture to radiative states is desirable to make efficient devices[96]. Even though the probe photon energy is far below the pump energy, the rise time of the DT signal is fast (0.33- 0.42ps). Here the capture time is defined as the time it takes the normalized signal to go from 10% to 90%.

Typically in the radiative recombination process, the pump energy excites electrons above the bandgap, and they relax to the gamma point where the electron and hole recombine. Figure 6.5 shows the phonon scattering processes that will take

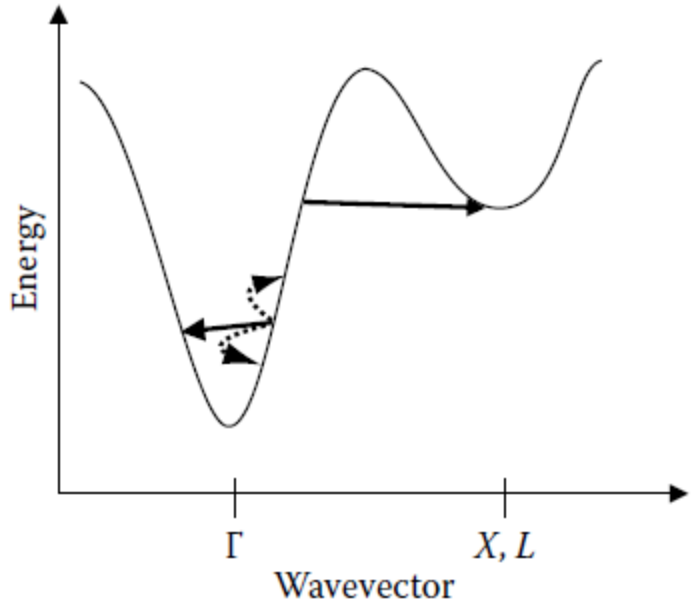

Figure 6.5: Schematic of a semiconductor conduction band. Phonon scattering events are shown as arrows. The solid line arrows are acoustic phonons with small energy transfer. The dashed arrows are optical phonons with much larger energy transfer[22].

an electron that is energized above the bandgap to the lowest state in theconduction band where it can radiatively recombine. The phonon allows for conservation of momentum, but this constraint can be relaxed when there is a high degree of disorder. Since phonon-mediated relaxation from the bands into the emitting states is not expected to be this fast, the risetime provides strong evidence that disorder (likely due to In composition fluctuations) relaxes k-selection and results in direct optical excitation of the emitting states even though the pump is nonresonant.

Capture times for InGaN/ GaN MQWs have been studied, but they vary and are dependent on temperature, carrier density, and size of the QWs[24,97]. In GaN QW lasers, the capture time of 1.2 ps was shown to vary significantly with injected carrier density and the PZE[94]. Capture times in InGaN/ GaN MQWs with a CW PL of 400nm were shown to be 0.4-0.8 ps[24]. However, it should be noted that the fast capture times observed in this system were for a degenerate 390 nm pump/probe, which is very close to the PL. The longer capture times were for a 260 nm pump

/390 nm probe. There is at 100-200 nm difference in the pump and probe for the capture times we measured, which is a difference of approximately 600 meV. This is much larger than the energy of the LO phonon, which is approximately 90 meV[98], so multiple phonon scattering events would need to occur. However, in GaN the electron- LO scattering rate is an order of magnitude larger than in GaAs; GaN is a polar system, so the carrier interaction with LO phonons dominates the carrier relaxation[99]. Another InGaN/ GaN MQWs with a CW PL of 400nm was shown to have carrier capture times of 0.31 -0.54 ps[97]. Longer capture times, 3.3-2.0 ps have been demonstrated in single GaN/InGaN nonpolar MQW core-shell NWs[26]. They claim that the longer capture time is governed by carrier-carrier scattering, not Auger scattering. Auger is not a direct measure of disorder, or localization, but disorder does enhance Auger recombination[100].

6.3.2 Relaxation lifetimes

Second, the observed relaxation times are much faster than would be expected for a radiative lifetime (due to the high PL efficiency); the decay times range from 3-5 ps for the initial decay and 20-60 ps for the longer decay component. This is much faster than lifetimes observed for InGaN quantum wells[101]. If the decay were simply a fast non-radiative process, then the PL emission would be very low. In contrast to the samples in Ra et al. [17], the quantum dots for this sample appear to exhibit disorder that leads to localization of states below the gap. This conclusion is supported by the inhomogenous broadening seen in the PL, approximately 100 nm for this sample, twice the FWHM of the dot-in-nanowire samples presented by Ra. The TRDT can be fit well with a bi-exponential decay.

$$y = a1\ \exp(-t/\tau 1) + a2\ \exp(-t/\tau 2) \tag{6.6}$$

Table 6.1: The lifetimes of the white light selective area growth nanowire samples, with different patterned diameters. Tau 1 is the fast decays and tau 2 is the slower decay. A1 and A2 are their respective amplitude ratios shown as a percentage.

Sample diameter	Probe (nm)	tau 1 (ps)	tau 2 (ps)	A1	A2	max $\Delta T/T$
d=∼195	500probe	2.62	25.50	0.96	0.04	3.72E-02
	550probe	5.34	34.93	0.98	0.02	1.64E-02
	600probe	3.13	14.25	0.67	0.33	7.80E-03
d=∼300	500probe	2.44	37.73	0.97	0.03	2.72E-02
	550probe	1.02	5.39	0.42	0.58	2.58E-02
	600probe	1.47	10.07	0.64	0.36	1.35E-02
d=∼700	500probe	5.29	100.57	0.82	0.18	1.01E-02
	550probe	2.72	22.08	0.43	0.57	1.56E-02

The fitted values are shown in Table 6.1. In the table A1 and A2 are the percentages of the relative amplitudes a1 and a2. It has been shown in InGaN quantum wells that localization should lead to an increase of radiative recombination, but a stronger increase in Auger recombination [102]; this would lead to fast nonradiative recombination and a suppression of PL. Hence the observed dynamics in our samples indicates the possibility of rapid redistribution of carriers among localized states into dark states (i.e. states not coupled to the probe field).

6.3.3 Power dependence

Power scaling can show whether a sample is being damaged, if there is saturation, or if two-photon or Auger effects are occurring. Here the 550nm probe is kept at 300 mW, with a 1/e 2 spotsize radius of 55 um. The pump ranges from 0.5mW to 3 mW with 1/e 2 spotsize radius of 79 um. The fluence ranges from 10 μJ/cm^2 to 61 μJ/cm^2. This is a fairly lower fluence for a 250kHz system. This power scaling was collected for one of the patterns on the WL nanowire sample. The diameters are

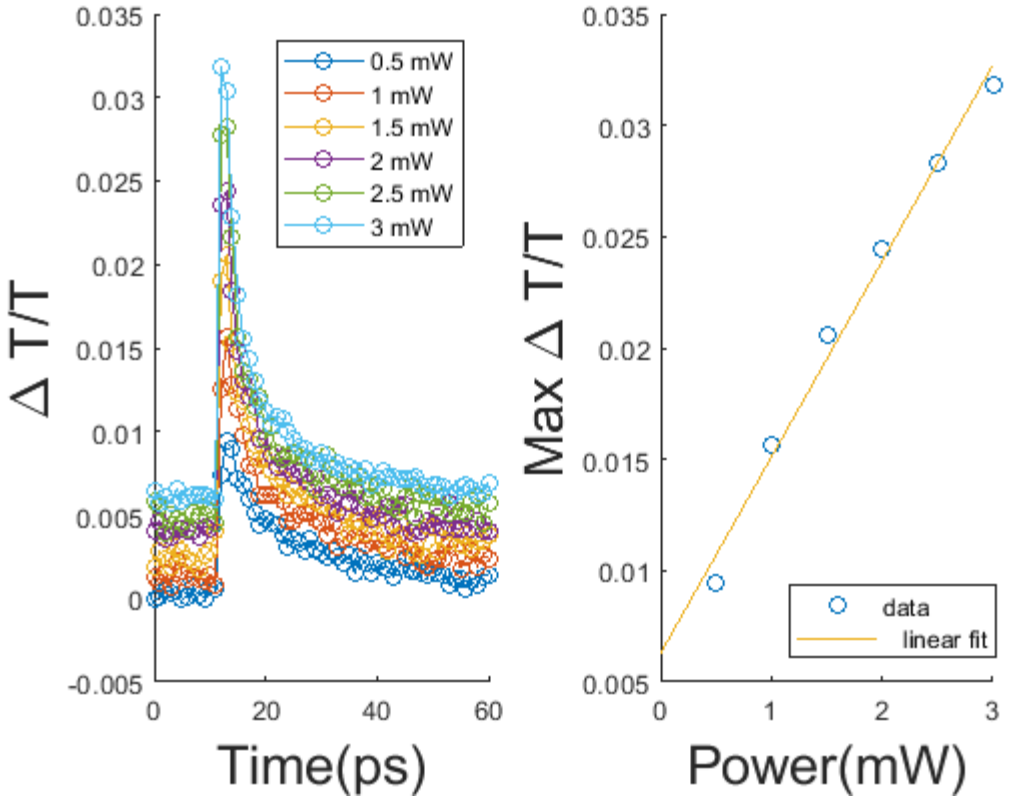

Figure 6.6: TRDT power scan. The nanowire pattern measured here, is one of the patterns on the white light nanowire sample, but is not the same diameter as the other patterns discussed so far. Thus it is not conclusive that this is the same scaling to be expected form the other patterns, but it is reasonable.

300nm, but this is a different pattern than the dynamics just discussed. The power scaling can potentially be different for each pattern set, so this is just discussed as an indication that most likely the other TRDT scans are in a linear regime. The power dependence within the scan range appears fairly linear, but a large scan range would be necessary to confirm. The most important conclusion is that there is not obvious damage or strong nonlinear effects over the fluence range relavant to this study (a more complete power dependence would be of interest for future work).

6.4 Time-resolved differential reflection of the green InGaN/Gan dot-in-nanowires

As was established in the last chapter, the green InGaN/GaN dot- in- nanowire sample has a CW PL with a FWHM of 15-20nm, centered at 500nm. In the TRDR measurements, the same WL pump and 400nm probe are used.

6.4.1 Capture times

As we discussed for the WL NW sample, the capture time can serve as an indicator of disorder in the system. From the narrow PL, it is expected that the green sample is more ordered than the WL sample. This is supported by the longer risetimes shown in Figure 6.7. The peaks are normalized so the risetime is visible, and only the stronger peaks are plotted in this graph. It is not that longer risetimes are better or even desirable, but in this case, they are an indication that electrons are being captured by the QDs which would take a finite time.

A selection of representative temporal scans for different probe wavelengths are plotted in Figure 6.8. This shows the relative amplitude of the different peaks. The scans have been shifted vertically, but that is the only post processing. The pump fluence is low, approximately 54 μJ/cm^2.

The first thing that is striking about this plot is the shift in time as the probe wavelength is changed. There are two possible reasons for the temporal shifts that will be discussed. The first is that this shift is due to a time delay for electrons relaxing into lower energy states. The second is that there is an artifact due to probe chirp. Several papers have been published that used a WL probe and show this shift in the data[25,103]. The ones cited here use a D_2O cell to generate a probe continuum that will generate as much chirp as sapphire, or any WL continuum source. They discuss the generation of the WL probe, but do not comment on whether it is chirped,

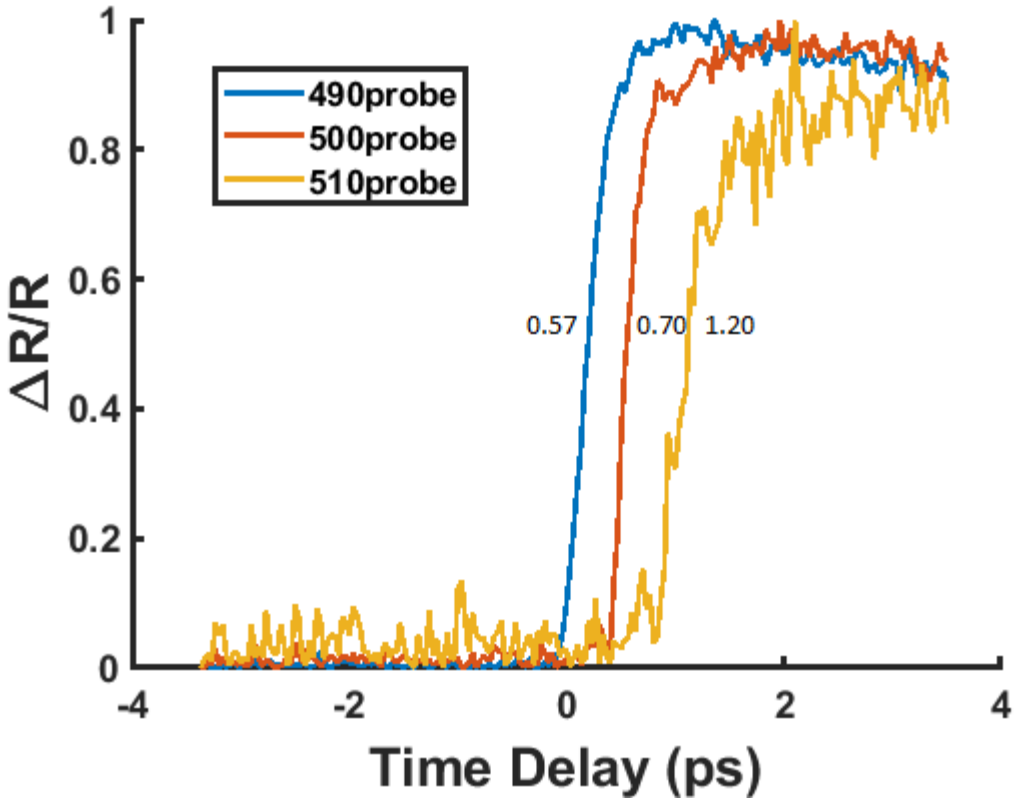

Figure 6.7: The initial peak of the TRDR data for the green dot-in-nanowire samples with 225nm diameters. The 10% - 90% risetime is displayed for each probe wavelength. These peaks are normalized and some wavelengths that showed very little signal are not shown in this plot, but are included in the next figure.

or whether the shifts in the data are real.

However, WL will inherently have a positive chirp, meaning that the longer wavelengths come first in time, and the short wavelengths come later. The relative time delay with respect for wavelength for a WL continuum generated in sapphire is shown in Figure 6.9. Two sources show a 2ps delay for WL sources between the wavelengths of 450 and 540nm; the exact chirp can be shifted for different parameters, but this is a reasonable estimate[23,104].

This may seem counter-intuitive, because we stated that the red wavelengths are arriving before the blue, in time, but the TRDT data is showing the response to the blue probe wavelengths before the red. This is a function of the pump-probe system.

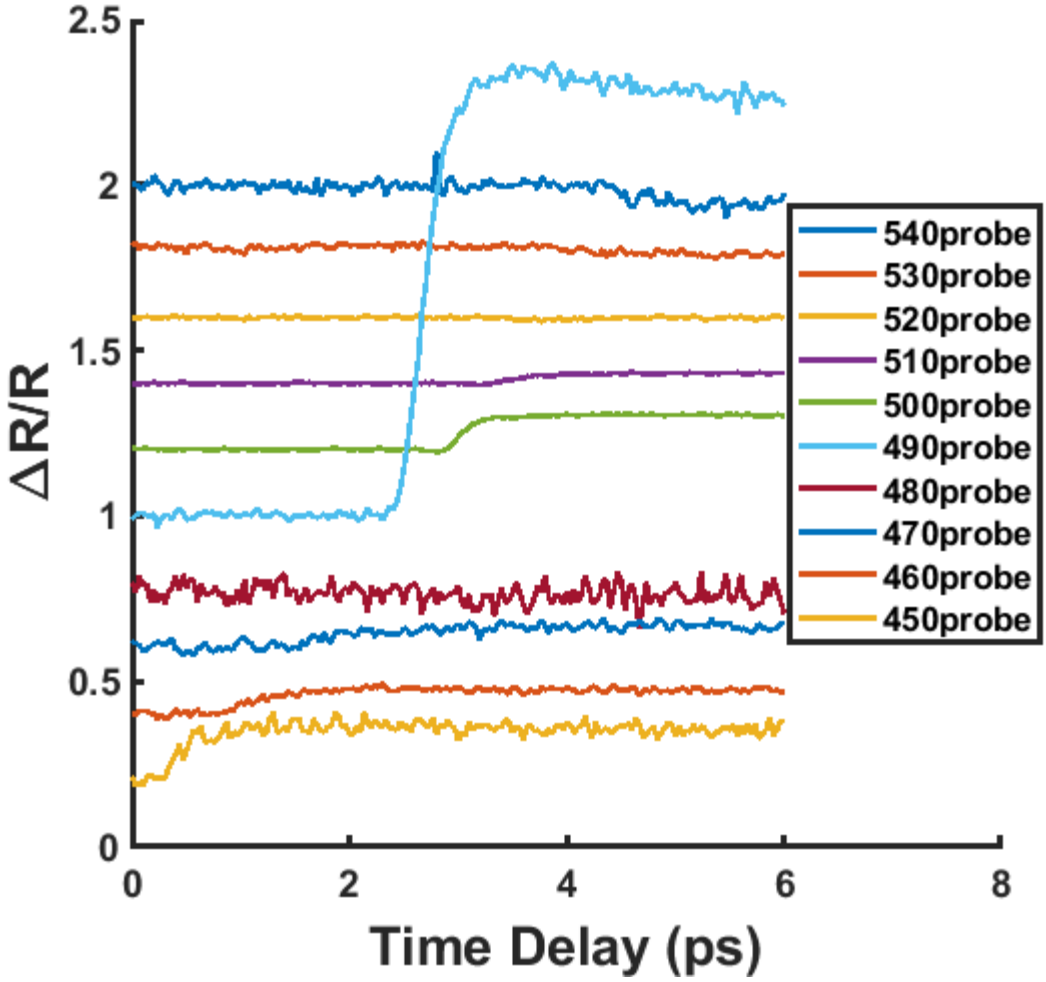

Figure 6.8: TRDR data for the green dot-in-nanowire samples with 225nm diameters. The scans are displaced vertically by 0.2. The shift in the timezero with probe wavelength is an artifact of the chirped WL probe.

Referring to Figure 6.1, the probe path stays stationary, and the delay is created by the pump path changing with the delay stage. The delay stage moving up vertically corresponds to the delay time on the x-axis of the TRDT data. So by moving the stage up and "forward in delay time", the optical path of the pump is shortened. Therefore, the probe wavelengths that see an interaction at that delay are actually ahead in time of the blue wavelengths. Thus, the shift seen in Figure 6.8, would correspond to a positively chirped probe.

Unfortunately, the chirp in the WL is not a trivial thing to remove. For nearly

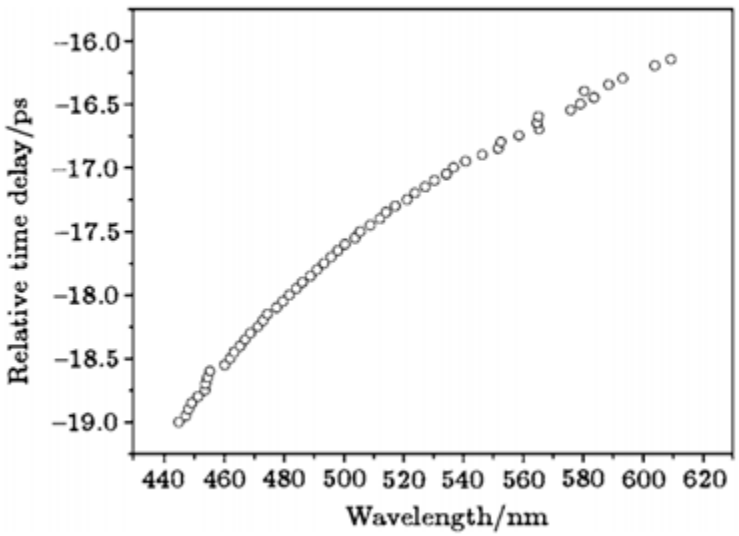

Figure 6.9: Plot of relative time delay vs the peak wavelength of the gated spectra of chirped WL from a sapphire crystal[23]. This shows that indeed the chirp of the WL can be on the order of what is seen in our TRDT measurements.

monochromatic sources, the chirp can be compensated using a pair of prisms; however, prisms cannot perfectly counterbalance the chirp of white light. Instead this would have to be done using post-processing in conjunction with calibrating the chirp of the WL[105]. One source did calibrate the timing shift of the WL and the data showed little to no shifting of the spectra with time[106]. Therefore, it is reasonable to conclude that the shifts seen in the data are due to the probe chirp and not an actual feature of the system. However, the relative time-zeros of the peaks were not shifted since the actual WL chirp was not monitored.

6.4.2 Relaxation lifetimes

Long scans were taken to capture the lifetimes of the states. A representative scan is shown in Figure 6.10. These scans were taken with an excitation fluence of 62 μJ/cm^2.

As can be seen, the bi-exponential decay captures the dynamics very well; the

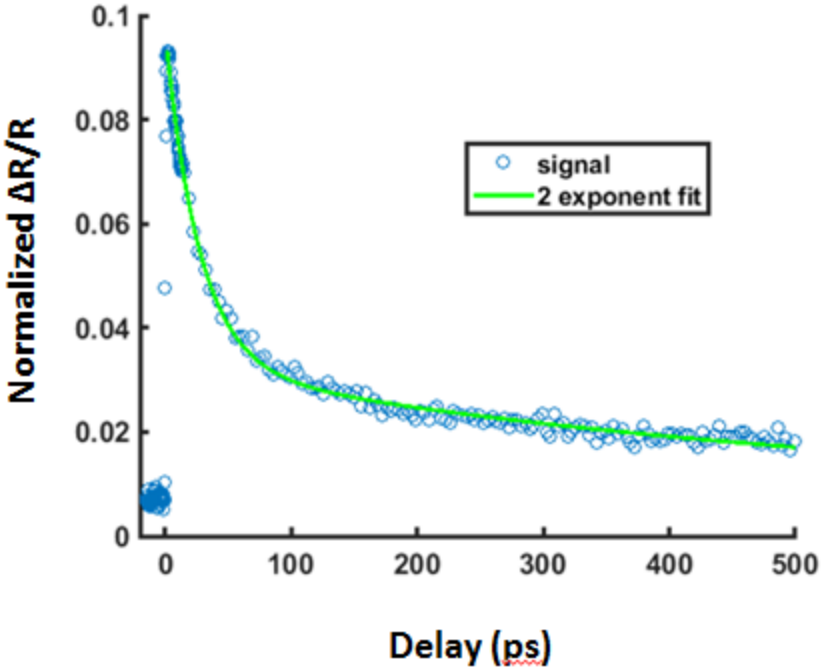

Figure 6.10: A representative plot of the TRDR with a bi-exponential fit.

values are shown in Table 6.2, with a fast initial decay of approximately 27 ps and a second longer lifetime approximately 330-830 ps. Scans were taken at probe wavelengths of 440 nm to 520 nm in increments of 10 nm; most had a very low signal. The amplitude of the shorter lifetime constant is double that of the contribution from the longer lifetime as is visually seen in 6.10. The largest change in reflection in the transient scans occurs at a probe wavelength of 490 nm, but as the spectral scans show, the peak is actually at approximately 495.

6.4.3 Spectral scans

Spectral scans that are stepped in time are plotted in Figure 6.11. These scans do not capture the fast time component. For that, please reference Figure 6.8. Each of these scans are taken with a monochromator and a motorized stage, so it would be very time consuming to take high resolution spectral and high resolution temporal

Table 6.2: The lifetimes of the green dot-in-nanowires samples, with two patterned diameters. Tau 1 is the fast decays and tau 2 is the slower decay. A1 and A2 are their respective amplitude ratios shown as a percentage.

Probe	(τ_1)	A1	(τ_2)	A2
Wire diameter ∼235nm				
490nm	31 ps	62%	354 ps	38%
500nm	23 ps	67%	705 ps	33%
Wire diameter ∼255nm				
490nm	35 ps	63%	328 ps	37%
500nm	27 ps	72%	531 ps	28%
510nm	23 ps	86%	829 ps	14%

scans. The purpose of this scan is to evaluate the peak location, and FWHM of the TRDR response. The peak is located at 495 nm, and it does not shift at longer times. The FWHM is comparable to the emission of the PL. It is common in pump-probe experiments to see a blueshift on the response due to the screening of the PZE field[25,107].

While the spectral scan peak at 495 nm is shifted from the CW PL, it matches the response seen in the pulsed PL, which supports the fact that the shift is due to the PZE field. Figure 6.12 shows the CW PL, pulsed PL, and differential reflection spectrum. The magnitude of the blueshift, should correspond to the extent that the PZE field is causing a change in the system. This shift is smaller than what has been observed previously for InGaN blue MQWs (approximately a 12nm shift). The smaller 5nm blueshift in the green dot-in-nanowire sample could be due to the enhanced confinement of the QDs when compared with the QWs.

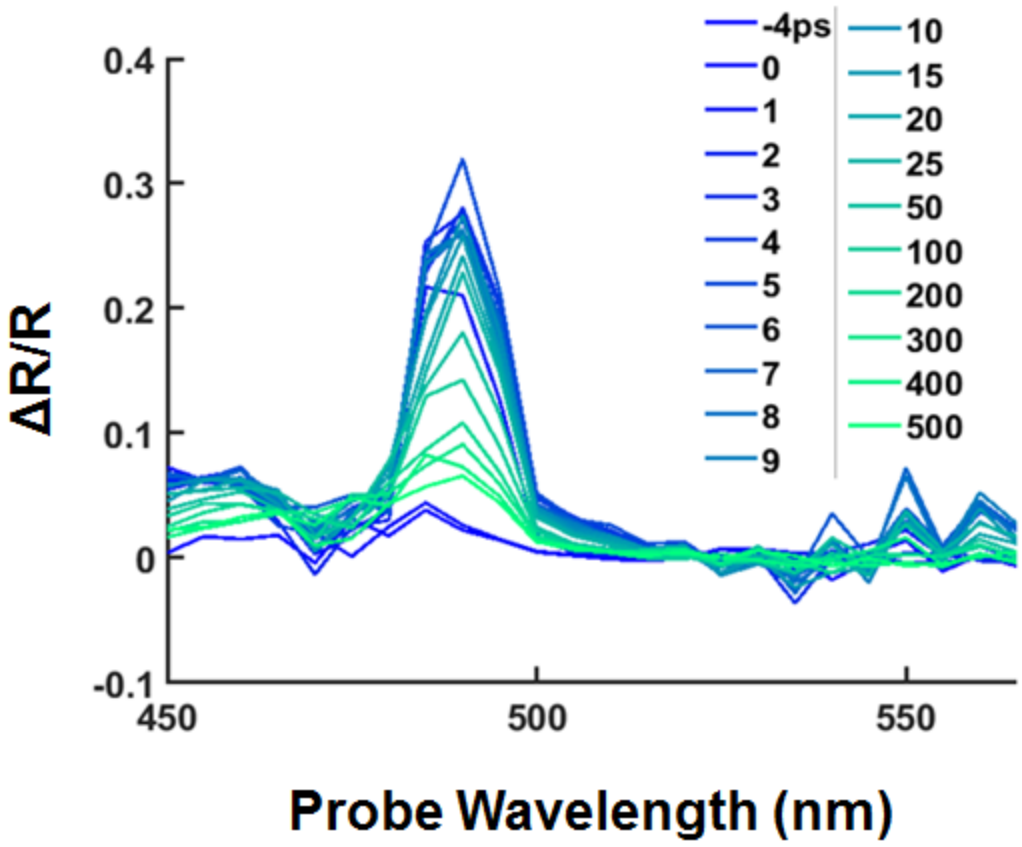

Figure 6.11: Spectra captured at different delay times. There is a response from the matrix states, but it is on a short timescale and is not captured.

6.5 Comparison to other current literature

It is important to put these experiments in context with other work in recent literature. Fan et al. measured the capture time of a blue InGaN MQW as a function of the pump fluence[24]. The fluences used in this work remained under 100 μJ/cm^2. The capture times for the WL NWs (330 fs -420 fs) was significantly faster than what is seen in Figure 6.13 in the low fluence regime. The green dot-in-nanowire samples showed similar or longer capture times (570 fs-1200 fs). This fits with the idea that disorder is causing fast capture times in the WL NWs, while the confinement in the green dot-in-nanowire samples would cause their risetimes to be slower than that of a QW. Many factors affect the capture rate, so it is difficult to compare data sets in

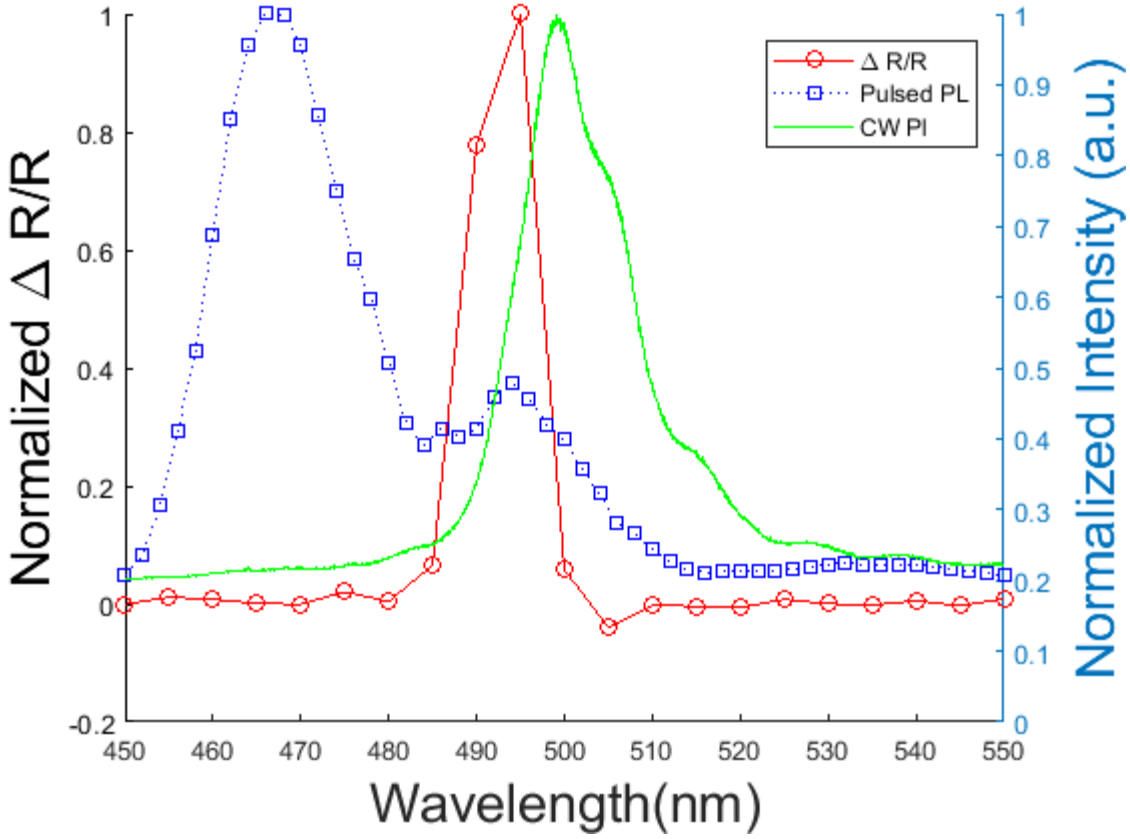

Figure 6.12: The differential reflection spectrum for a 1 ps delay is overlaid with the CW PL and the pulsed PL. The differential transmission spectral response corresponds to the pulsed PL. There is a response of the matrix states, but due to the probe chirp it does not show up in the differential reflection plotted, since this was chosen at the maximum of the QD response.

more than just a qualitative way. The probe wavelength for the data in Figure 6.13 is not explicitly stated, but the capture rate is a function of the state's energy; the blue probe will have a faster risetime than the red probe[25]. This is true for both of our samples. Ozgur and Everitt credit this to the carriers scattering into lower energy states[25].

The capture and relaxation rates have also been shown to be dependent on the pump power. Ozgur and Everitt explored the spontaneous emission (SPE) regime and the stimulated emission (SE) regime for a blue InGaN MQW sample[25]. As the pump power is raised and the number of carriers is increased, just like in a laser,

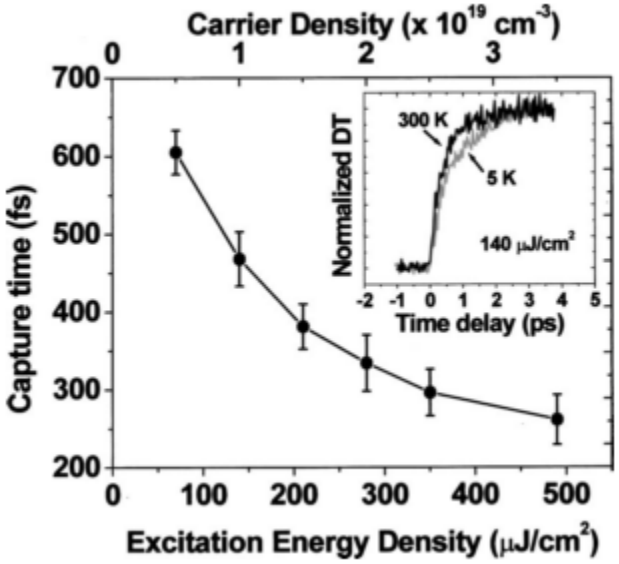

Figure 6.13: (Capture time for an InGaN MQW at 300 K with 260 nm pumping versus excitation energy density. The top axis gives the initial density in the barriers averaged over the MQW region. The inset compares the DT signals at 5 and 300 K for an excitation energy density of 140 μJ/cm^2[24].

the radiative recombination of one electron-hole pair can stimulate the recombination of other pairs. They found the threshold fluence to be 100 μJ/cm^2 in their system. Figure 6.14 shows the TRDT data for below the SE threshold (a) and above the SE threshold (b). The pump is at 385nm and the PL is centered at 410 nm and 408 nm, respectively. The system is a 1kHz rep rate, so the 100 μJ/cm^2 fluence actually carries 250 times as many photons per pulse as the same fluence from our system. The PL changes shape and they observe a much faster τ_1 in the SE regime. Under the conditions of SE, an initial decay time of <10 ps was observed, while below the SE threshold this time increased to 13.5 ps. The explanation is that the GaN 3D states are supplying carriers to the 2D QW states that are undergoing SE. Carrier recombination was observed to have a lifetime of < 1ns. In our work, the fluences were kept low, <65 μJ/cm^2, so it has been assumed that this is within the SPE regime. However, the threshold for QDs would ideally be lower than for QWs. The WL NWs showed a linear response in this regime; however, measurements on the

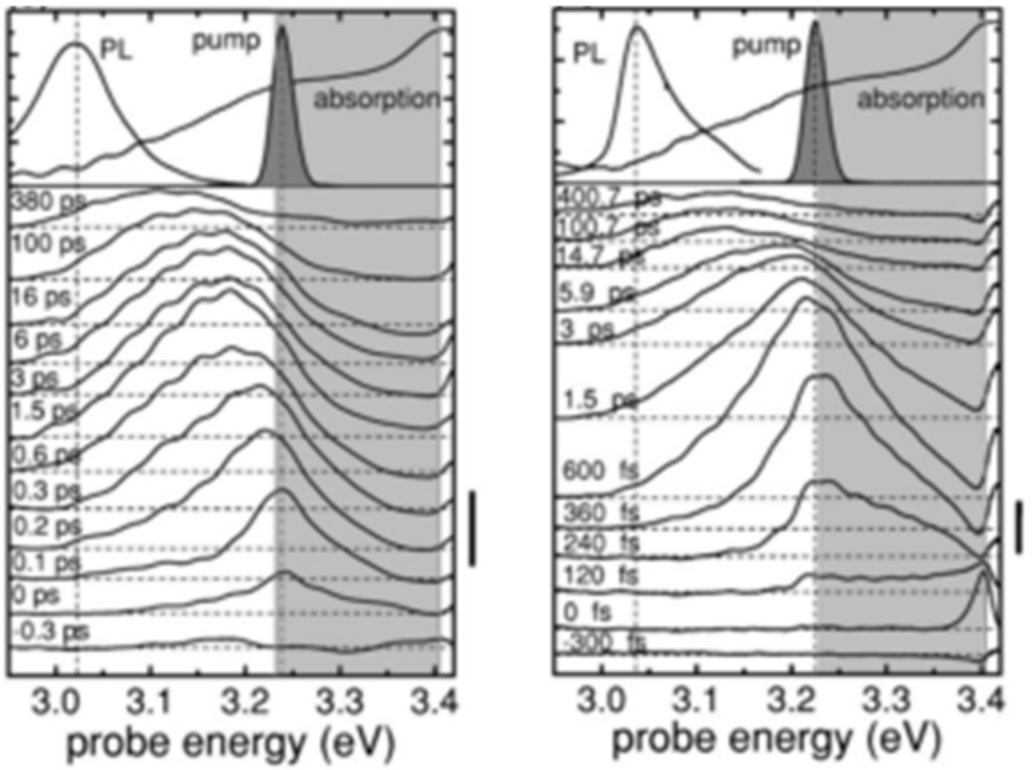

Figure 6.14: (a) Spectrally resolved TRDT for at barrier energy excitations at various delays for an excitation energy density of 300 μJ/cm^2. Pulsed absorption shows a clear absorption edge at 3.23 eV, and the shaded regions indicate the states between the barrier and the GaN band edges. (b) TRDT data for at-barrier excitation with a lower excitation density of 60 μJ/cm^2. The vertical bars on the sides indicate a DT magnitude of 0.2[25].

green dot-in-nanowire sample needs to be further developed. The fluence dependence and establishment of the SE regime will be discussed as future work.

Other relevant published lifetimes include the data from single InGaN/GaN MQW NWs. These wires were grown radially, so the growth plane is the non-polar m-plane, which should lead to a lower PZE field. The work described here was done by Boubanga-Tombet et al.[26].

The risetime getting shorter as the fluence increases is a function of the increased carrier-carrier scattering. It is not discussed in the paper, but the distinct change in slope around 100 μJ/cm^2 mimics the onset of SE described by Ozgur et al.[25].

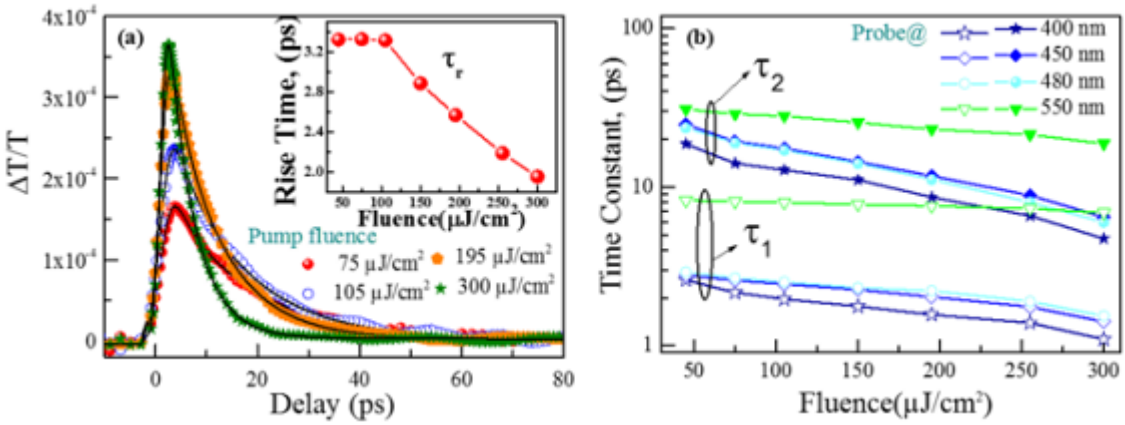

Figure 6.15: (a) Pump fluence-dependent differential transmission in the single MQW NW for pump and probe wavelengths of 266 and 400 nm, respectively. The solid lines represent double exponential fits to the data. The inset shows the pump fluence-dependent rise time, τ_r, extracted from these fits. (b) Pump fluence and probe wavelength-dependent relaxation time constants τ_1 (open shapes) and τ_2 (solid shapes), extracted from (a).[26].

The τ_1 and τ_2 in Figure 6.15b are smaller than the decays measured for the green dot-in-nanowire sample. This makes intuitive sense because QDs should have a longer lifetime than QWs. A single exciton in a QD has a radiative lifetime two orders of magnitude longer than a well[108]. However, the lifetimes are dependent on my factors, so this is not conclusive, but evidential.

6.6 Discussion

Table 6.3 shows a comparison of the key timescales for this work and other systems from literature. The lifetimes of the green sample are on the order of magnitude or longer than the other samples in the table, while the WL sample has lifetimes which are comparable or shorter.

6.6.1 White light samples

Four key data points indicate that the WL NW sample does not have QDs but instead is has more QW-like features, and most likely has a significant amount of

Table 6.3: Key lifetimes of the samples explored in this work, and other recent literature. Not all of the risetimes were measured in the same way, some fit with an exponential, others were a 10% - 90% measurement. Also, the values are very probe wavelength and intensity dependent, so this table only quotes ranges and should be used as a qualitative comparison.

Sample	Risetime	τ_1	τ_2	Reference
Green dot-in-nanowire	0.57-1.2 ps	20- 30 ps	330- 830 ps	This work
WL nanowires	0.33-0.42 ps	1-6 ps	5- 100 ps	This work
InGaN/GaN MQW	0.25- 0.6 ps	-	-	[24]
$In_{0.08}Ga_{0.92}N$/GaN MQW	-	2.6- 13.5 ps	660 ps	[25]
$In_{0.12}Ga_{0.88}N$/GaN MQW	-	1- 9 ps	5- 30 ps	[26]
InGaN/GaN MQW	0.5ps	6 ps		[98]

disorder.

1. Broad PL: The PL ranges from 490 to 650 nm, as was shown in Figure 5.4. As was discussed, this is very broad and most likely not from QDs but an inhomogenous mixture of alloy concentrations and structures.

2. Fast risetimes: The risetimes are not unreasonable for InGaN MQWs, but they nearly twice as fast as the green dot-in-nanowire samples.

3. Short lifetimes: The lifetimes are more than an order of magnitude shorter than those from the green dot-in-nanowire samples. They are reasonable for QW lifetimes.

4. Low CW PL signal when compared with the green dot-in-nanowire sample and other QD samples. This is not quantified precisely, but is a qualitative description by Yong-Ho. The CW PL of the WL sample and the green sample were taken under different conditions, so they are not directly comparable.

6.6.2 Green QD samples

To the best of our knowledge, no time-resolved pump probe experiments have been published for samples with emission in the green (500 nm). A time-resolved PL study on green self-asembled QDs was published by Weng et al.[109]. The papers for time-resolved pump probe measurements used as a comparison in Table 6.3 all have an emission peak centered at 400-415 nm. The indium concentrations range from $In_{0.08}Ga_{0.92}N$ to $In_{0.12}Ga_{0.88}N$[25,26]. The exact In concentration in our sample is unknown since the emission is dependent on the In concentration and the size of the dot; regardless, the longer wavelength emission in the desired green gap makes the characterization of this sample exciting. We attribute the measured lifetimes to:

1. fast (tau_1): decay into non-radiative states (e.g. trap states). We attribute the fact that this is slower than the WL sample and other samples in the table to a higher PL quantum efficiency.

2. slow (tau_2): recombination (mostly radiative) The next chapter will present a summary of the work as well as discuss future directions.

CHAPTER VII

Conclusions and future work

In this thesis, transient pump-probe measurements were used to investigate the electron capture and relaxation processes of TiN and InGaN/GaN dot-in-nanowires.

7.1 TiN electron dynamics

This work discussed TiN as a material of interest for its potential plasmonic applications; its dielectric functions', ϵ_1 and ϵ_2, resemble those of gold. TiN would be an attractive alternative to gold due to its higher melting point, higher damage threshold, low cost, and CMOS compatibility. Size and shape are particularly important for plasmonics, and TiN is easy to make in a thin film, patterned structure, or nanoparticles.

While TiN has many advantages, it is a complex system to characterize. The bandstructure looks like a mix between a metal and a semiconductor. The orbitals of the valance electrons from the Ti atoms and the N atoms mix; the complicated electronic bonding system includes metallic, covalent, and ionic bonds[55]. In addition, the sample variation is large, and often not well characterized in the literature.

7.1.1 Conclusions

Current state of knowledge before this work:

- TiN is an exciting material for potential plasmonic applications, such as hot carrier driven devices and thermalphotvoltaics.
- The fast time scale (less than 5 ps) electron relaxation processes had not been explored.
- The electron- phonon coupling, G, associated with the hot carrier cooling, was not present in the literature, either calculated or experimental.
- The electron- phonon coupling, λ, associated with superconductivity, had been measured through low temperature specific heat measurements for different TiN samples.
- The initial expectation was that the electron- phonon coupling would be similar to gold, or an order of magnitude lower since the carrier concentration in TiN is typically an order of magnitude lower. It was thought that the long-lived hot electrons would be useful in hot electron driven devices and processes.

Conclusions from this work:

- TiN still has exciting potential applications in plasmonics, but the substrate is going to play a very important role. Previous papers made devices that directly compared the responses of TiN and gold without accounting for the substrate. The heat transferred to TiN is not dissipated quickly and transfers in the substrate. This is manifested in very large and long-lived differential signals.
- TiN is a great candidate for plasmonic photothermal applications.
- The electron relaxation is very different than gold, which has a relaxation in a few ps. This is due to 1) gold having a thermal conductivity that is an order of magnitude larger than TiN and 2) gold having an electron-phonon coupling

three orders of magnitude lower than TiN. The hot electrons in gold reach much higher temperatures and do not transfer as much heat into the substrate.

- The electron- phonon coupling is very strong in TiN, G $\approx 10^{18}$ [W/m^{3}K]. This is supported by calculations of G from other material parameters as well as a fitting with the two temperature model. Only an order of magnitude is claimed due to the large variation in published material constants for TiN.

- The two temperature model is used to support the conclusions from the calculations, but cannot be calculated exactly since it is very dependent on the thermal conductivity of the material. Due to the large variation in TiN samples, without the measuring thermal conductivity directly for this sample, the value used is only an estimate. Also, the conductivity will change for very thin samples (30nm) and values for thin films were not explicitly available in the literature.

- Pump –probe is sometimes used to measure the thermal conductivities of materials, but the sample used in this work was too thin to not show a substrate effect. Other experiments would be required to carefully subtract out the substrate effect.

7.1.2 Future work

While it would be very interesting to see the electron dynamics of TiN nanoparticles, due to the complexity of modelling this material for a thin film, that experiment would not be useful without very careful characterization of the TiN material. In order for TiN to expand its prevalence in optoelectronics, the composition of the material has to be understood. More work is needed in characterizing the growth process of the material since samples are extremely varied.

A new interesting direction in TiN studies is the recently demonstrated semicon-

ducting titanium nitride structure, Ti_3N_4, that was reported in February 2018 and is claimed to have a bandgap of 0.8 - 0.9 eV[110].

7.2 InGaN/GaN dot-in-nanowire electron dynamics

This work examined two selective area growth InGaN/GaN nanowire samples. The first sample, WL NW sample, showed a lot of disorder, but had a broad emission at green-orange wavelengths, which is a spectral region of interest due to a lack of efficient emitters. The second sample, the green dot-in-nanowire sample demonstrated QD properties and also emits at a wavelength important for applications. This was the first reported TRDT measurement on a green InGaN/GaN QD.

7.2.1 Conclusions

Current state of knowledge before this work:

- HADDF and EELS maps showed dot formation in single wire selective-area growth NWs. PL emission was consistent with QD behavior
- TRDT and TRDR experiments on InGaN/GaN QW and MQW heterostructures showed the capture rate and relaxation dynamics of these systems. Both probe wavelength and carrier density measurements were demonstrated. The risetime of the TRDT signal was shown to increase as the probe wavelength was shifted red. This was attributed to the carriers scattering into the lower energy states at longer delay times.
- The LO phonon in InGaN has an energy of 90 meV and the electron- LO scattering rate is an order of magnitude larger than the scattering rate in GaAs.
- High carrier density experiments, intensity > 100 μJ/cm^2, show stimulated emission. The carrier-carrier scattering is dominant as carriers are moved from the 3D barrier states into the 2D QWs.

Conclusions from this work:

- Pulsed excitation PL experiments show a strong peak at 466 nm with a smaller peak at 494 nm. The 466 nm peak is from the recombination of the InGaN matrix states. When dots are formed in a self-assembled way on a roughened surface they form phase separated inhomogenous InGaN alloys outside of the dots called the matrix. These states are not visible in the CW PL so this is a carrier density effect.

- The blueshift in the QD emission with pulsed excitation vs CW was 5-6 nm, which is smaller than shifts seen in other systems (10-13 nm). This is attributed to the reduced PZE in the QDs.

- Time-resolved study of the room temperature ultrafast carrier dynamics of green InGaN/GaN dot-in-nanowires showed that the risetime shifted from 0.57-1.2 ps for a 490 nm probe-510 nm probe, respectively. This shows the carrier scattering into lower energy states at longer delay times.

- A small TRDT signal was observed at 450 nm (this is not a precise wavelength this set of time-resolved scans was only taken at 10 nm intervals) which is the signal from the matrix states.

- Initial characterization of the TRDR signal at the QD peak shows two decay times. The fast time decay, $\tau_1 \approx$ 20-35 ps, is attributed to electrons relaxing into dark states

- The second longer lifetime, $\tau_2 \approx$ 330- 830 ps, is attributed to the lifetime of the radiative states.

The physics from each of these experiments is summarized in Table 7.1. Wavelength dependence was shown for these interactions, but more intensity dependence experiments are required. The temperature column is also currently empty.

Table 7.1: Summary of the physics that can be explored using TRDT and PL measurements. The Green QD and WL NW sample are in the column where either spectral scans or power scans have been done on that sample. Further tests will be required to expand the range of some of the scans. The temperature column is left blank as those are a different set of experiments for the next researcher.

Physics	Experiments/ data	Density Dependence (Power and Wavelength)	Temperature Dependence
Capture	Risetime	Green QDNW	
Polarization fields, Carrier scattering	Fast decay (1) Pulsed PL	Green QD WL NW	
Lifetime, Trap states	Slow decay (2) Pulsed PL	Green QD WL NW	
Exciton, Band edge States	CW and Pulsed PL dR spectrum	Green QD WL NW	
Biexiton	Power scaling	WL NW	

7.2.2 Future work

The next step in the InGaN/GaN dot-in-nanowires is to continue the systematic study of how growth conditions, geometry, and other characteristics affect the lifetime and emission of the carriers. More intensity/carrier density dependent measurements are needed to characterize the scattering processes and the threshold of the stimulated emission regime. Temperature dependent studies would also realize valuable information about the scattering dynamics and the response of the phase separated matrix. Based on previous research, we would expect that the matrix would have a very strong effect at low temperature where the electrons cannot scatter to the QDs.

The next exciting step in this work will be to use a 3 pulse pump-probe experiment to characterize the gain. This experiment will lay the foundation for establishing QD laser.

The scattering rates and other parameters measured here are critical to under-

standing the processes which contribute to radiative and non-radiative states. This information is key to creating future efficient LEDs, single source emitters, QD lasers and many other exciting devices. I am excited to see where the field goes next.

BIBLIOGRAPHY

BIBLIOGRAPHY

[1] J. Hohlfeld, S.-S. Wellershoff, J. Güdde, U. Conrad, V. Jähnke, and E. Matthias, "Electron and lattice dynamics following optical excitation of metals," *Chemical Physics*, vol. 251, no. 1-3, pp. 237–258, 2000.

[2] D. J. Hilton, "Ultrafast Pump– Probe Spectroscopy," in *Optical Techniques for Soilid-State Materials Characterization*, R. P. Prasankumar and A. J. Taylor, Eds. Boca Raton, FL: CRC Press, 2012, ch. 9, pp. 330–365.

[3] F. Monticone and A. Alu, "Metamaterial, plasmonic and nanophotonic devices," *Reports on Progress in Physics*, vol. 80, no. 3, 2017.

[4] M. L. Brongersma, N. J. Halas, and P. Nordlander, "Plasmon-induced hot carrier science and technology," *Nature Nanotechnology*, vol. 10, no. 1, pp. 25–34, 2015. [Online]. Available: http://dx.doi.org/10.1038/nnano.2014.311

[5] H. George, J. Reed, M. Ferdinandus, C. DeVault, U. Guler, A. Lagutchev, A. . Urbas, V. M. Shalaev, A. Boltasseva, T. Norris, and N. Kinsey, "Nonlinearities and Carrier Dynamics in Refractory Plasmonic TiN Thin Films," 2018.

[6] P. B. Johnson and R. W. Christry, "Optical Constants of the Noble Metals," *Physical Review B*, vol. 6, no. 12, pp. 4370–4379, 1972.

[7] V. Ern and A. Switendick, "Electronic Band Structure of TiC, TiN, and TiO," *Physical Review*, vol. 137, no. 6A, pp. 1927–1935, 1965.

[8] C. Stampfl, W. Mannstadt, R. Asahi, and A. J. Freeman, "Electronic structure and physical properties of early transition metal mononitrides: Density-functional theory LDA, GGA, and screened-exchange LDA FLAPW calculations," *Physical Review B - Condensed Matter and Materials Physics*, vol. 63, no. 15, pp. 1–11, 2001.

[9] S. K. Gupta, S. D. Gupta, H. R. Soni, V. Mankad, and P. K. Jha, "First-principles studies of the superconductivity and vibrational properties of transition-metal nitrides TMN (TM = Ti, V, and Cr)," *Materials Chemistry and Physics*, vol. 143, no. 2, pp. 503–513, 2014. [Online]. Available: http://dx.doi.org/10.1016/j.matchemphys.2013.08.046

[10] S. Pimputkar, J. S. Speck, S. P. Denbaars, and S. Nakamura, "Prospects for LED lighting," *Nature Photonics*, vol. 3, no. 4, pp. 180–182, 2009.

[11] M. Auf Der Maur, A. Pecchia, G. Penazzi, W. Rodrigues, and A. Di Carlo, "Efficiency Drop in Green InGaN/GaN Light Emitting Diodes: The Role of Random Alloy Fluctuations," *Physical Review Letters*, vol. 116, no. 2, pp. 1–5, 2016.

[12] I. Vurgaftman and J. R. Meyer, "Band parameters for nitrogen-containing semiconductors," *Journal of Applied Physics*, vol. 94, no. 6, pp. 3675–3696, 2003.

[13] W. Bi, H.-C. Kuo, P.-c. Ku, and B. Shen, Eds., *Handbook of GaN Semiconductor Materials and Devices*. Boca Raton, FL: CRC Press, 2018.

[14] D. Bimberg and U. W. Pohl, "Quantum dots: Promises and accomplishments," *Materials Today*, vol. 14, no. 9, pp. 388–397, 2011. [Online]. Available: http://dx.doi.org/10.1016/S1369-7021(11)70183-3

[15] R. Wang, Y.-h. Ra, Y. Wu, H. P. T. Nguyen, R. Wang, Y.-h. Ra, Y. Wu, S. Zhao, and P. T. Hieu, "Tunable, Full-Color Nanowire Light Emitting Diode Arrays Monolithically Integrated on Si and Sapphire," in *SPIE*, no. February 2016, San Francisco, CA, 2016.

[16] I. Gan, H.-w. Lin, Y.-j. Lu, H.-y. Chen, H.-m. Lee, H.-w. Lin, Y.-j. Lu, and H.-y. Chen, "InGaN/GaN nanorod array white light-emitting diode," *Applied Physics Letters*, vol. 97, no. 7, p. 073101, 2010. [Online]. Available: http://aip.scitation.org/doi/10.1063/1.3478515

[17] Y. H. Ra, R. Wang, S. Y. Woo, M. Djavid, S. M. Sadaf, J. Lee, G. A. Botton, and Z. Mi, "Full-color single nanowire pixels for projection displays," *Nano Letters*, vol. 16, no. 7, pp. 4608–4615, 2016.

[18] X. Xu, Q. Wang, C. Li, Z. Ji, M. Xu, H. Yang, and X. Xu, "Enhanced localisation effect and reduced quantum-confined Stark effect of carriers in InGaN/GaN multiple quantum wells embedded in nanopillars," *Journal of Luminescence*, vol. 203, no. November 2017, pp. 216–221, 2018.

[19] I. K. Park, M. K. Kwon, S. H. Baek, Y. W. Ok, T. Y. Seong, S. J. Park, Y. S. Kim, Y. T. Moon, and D. J. Kim, "Enhancement of phase separation in the InGaN layer for self-assembled In-rich quantum dots," *Applied Physics Letters*, vol. 87, no. 6, 2005.

[20] H. Sun, Z. Ji, H. Wang, H. Xiao, S. Qu, X. Xu, A. Jin, and H. Yang, "Transfer and recombination mechanism of carriers in phase-separated InGaN quantum wells," *Journal of Applied Physics*, vol. 114, no. 9, 2013.

[21] N. Shimosako, Y. Inose, H. Satoh, K. Kinjo, T. Nakaoka, T. Oto, K. Kishino, and K. Ema, "Carrier-density dependence of photoluminescence from localized states in InGaN/GaN quantum wells in nanocolumns and a thin film," *Journal of Applied Physics*, vol. 118, no. 17, 2015.

[22] J. Demsar and T. Dekorsy, "Carrier Dyna mics in Bulk Semiconductors and Metals after Ultr ashort Pulse Excitation," in *Optical Techniques for Soilid-State Materials Characterization*, R. P. Prasankumar and A. J. Taylor, Eds. Boca Raton, FL: CRC Press, 2012, ch. 8.

[23] Q. Dong-Hui, L. Shi-Lin, Z. Lei, Y. Jian, W. Li, Y. Guo-Zhen, and W. Yu-Xiang, "Experimental study on the chirped structure of the white-light continuum generation by femtosecond laser spectroscopy," *China Physics*, vol. 12, 2003.

[24] W. H. Fan, S. M. Olaizola, J. P. Wells, A. M. Fox, T. Wang, P. J. Parbrook, D. J. Mowbray, and M. S. Skolnick, "Femtosecond studies of electron capture times in InGaNGaN multiple quantum wells (Applied Physics Letters (2004) 84 (3052))," *Applied Physics Letters*, vol. 91, no. 9, 2007.

[25] Ü. Özgür and H. O. Everitt, "Ultrafast carrier relaxation in GaN, In0.05Ga0.95N, and an In0.07Ga0.93NÕIn0.12Ga0.88N multiple quantum well," *Physical Review B*, vol. 67, no. 15, p. 155308, 2003. [Online]. Available: http://link.aps.org/doi/10.1103/PhysRevB.67.155308

[26] S. Boubanga-tombet, J. B. Wright, P. Lu, M. R. C. Williams, C. Li, G. T. Wang, and R. P. Prasankumar, "Ultrafast Carrier Capture and Auger Recombination in Single GaN/ InGaN Multiple Quantum Well Nanowires," *ACS Photonics*, vol. 3, 2016.

[27] C. Surez, W. E. Bron, and T. Juhasz, "Dynamics and transport of electronic carriers in thin gold films," *Physical Review Letters*, vol. 75, no. 24, pp. 4536–4539, 1995.

[28] R. H. Groeneveld, R. Sprik, and A. Lagendijk, "Effect of a nonthermal electron distribution on the electron-phonon energy relaxation process in noble metals," *Physical Review B*, vol. 45, no. 9, pp. 5079–5082, 1992.

[29] C. K. Sun, F. Vallée, L. H. Acioli, E. P. Ippen, and J. G. Fujimoto, "Femtosecond investigation of electron thermalization in gold," *Phys. Rev. B*, vol. 48, no. 16, pp. 365–368, 1993.

[30] ——, "Femtosecond-tunable measurement of electron thermalization in gold," *Physical Review B*, vol. 50, no. 20, pp. 15 337–15 348, 1994.

[31] R. W. Schoenlein, W. Z. Lin, J. G. Fujimoto, and G. L. Eesley, "Femtosecond studies of nonequilibrium electronic processes in metals," *Physical Review Letters*, vol. 58, no. 16, pp. 1680–1683, 1987.

[32] P. M. Norris, A. P. Caffrey, R. J. Stevens, J. M. Klopf, J. T. McLeskey, and A. N. Smith, "Femtosecond pump-probe nondestructive examination of materials (invited)," *Review of Scientific Instruments*, vol. 74, no. 1 II, pp. 400–406, 2003.

[33] S. A. Maier, *Plasmonics : Fundamentals and Applications*. New York, New York: Springer, 2007, vol. 677, no. 1. [Online]. Available: http://elib.tu-darmstadt.de/tocs/95069577.pdf

[34] M. Mayy, G. Zhu, A. D. Webb, H. Ferguson, T. Norris, V. A. Podolskiy, and M. A. Noginov, "Toward parametric amplification in plasmonic systems : Second harmonic generation enhanced by surface plasmon polaritons," vol. 22, no. 7, pp. 1110–1112, 2014.

[35] S. B. Hasan, C. Rockstuhl, T. Pertsch, and F. Lederer, "Second-order nonlinear frequency conversion processes in plasmonic slot waveguides," *Journal of the Optical Society of America B*, vol. 29, no. 7, p. 1606, jun 2012. [Online]. Available: http://www.opticsinfobase.org/abstract.cfm?URI=josab-29-7-1606

[36] I. Shadrivov, "Nonlinear plasmon-polaritons," *IEEE Photonic Society 24th Annual Meeting*, vol. 2, no. 2, pp. 379–380, oct 2011. [Online]. Available: http://ieeexplore.ieee.org/lpdocs/epic03/wrapper.htm?arnumber=6110586

[37] N. P. de Leon, M. D. Lukin, and H. Park, "Quantum Plasmonic Circuits," *IEEE Journal of Selected Topics in Quantum Electronics*, vol. 18, no. 6, pp. 1781–1791, nov 2012. [Online]. Available: http://ieeexplore.ieee.org/lpdocs/epic03/wrapper.htm?arnumber=6193116

[38] F. F. Lu, T. Li, J. Xu, Z. D. Xie, L. Li, S. N. Zhu, and Y. Y. Zhu, "Surface plasmon polariton enhanced by optical parametric amplification in nonlinear hybrid waveguide." *Optics express*, vol. 19, no. 4, pp. 2858–65, feb 2011. [Online]. Available: http://www.ncbi.nlm.nih.gov/pubmed/21369107

[39] M. Nezhad, K. Tetz, and Y. Fainman, "Gain assisted propagation of surface plasmon polaritons on planar metallic waveguides." *Optics express*, vol. 12, no. 17, pp. 4072–9, aug 2004. [Online]. Available: http://www.ncbi.nlm.nih.gov/pubmed/19483948

[40] J. A. Briggs, G. V. Naik, T. A. Petach, B. K. Baum, D. Goldhaber-Gordon, and J. A. Dionne, "Fully CMOS-compatible titanium nitride nanoantennas," *Applied Physics Letters*, vol. 108, no. 5, 2016.

[41] K. A. Willets and R. P. Van Duyne, "Localized Surface Plasmon Resonance Spectroscopy and Sensing," *Annual Review of Physical Chemistry*, vol. 58, no. 1, pp. 267–297, 2007. [Online]. Available: http://www.annualreviews.org/doi/10.1146/annurev.physchem.58.032806.104607

[42] W. Hou and S. B. Cronin, "A review of surface plasmon resonance-enhanced photocatalysis," *Advanced Functional Materials*, vol. 23, no. 13, pp. 1612–1619, 2013.

[43] E. Hutter and J. H. Fendler, "Exploitation of localized surface plasmon resonance," *Advanced Materials*, vol. 16, no. 19, pp. 1685–1706, 2004.

[44] M. L. Brongersma, J. W. Hartman, and H. H. Atwater, "Plasmonics: Electromagnetic Energy Transfer and Switching in Nanoparticle Chain-Arrays Below the Diffraction Limit," *MRS Proceedings*, vol. 582, no. 24, p. H10.5, 1999. [Online]. Available: http://journals.cambridge.org/abstract{_}S1946427400639556

[45] K. Aslan, J. R. Lakowicz, and C. D. Geddes, "Plasmon light scattering in biology and medicine: New sensing approaches, visions and perspectives," *Current Opinion in Chemical Biology*, vol. 9, no. 5, pp. 538–544, 2005.

[46] V. G. Veselago, "The Electromagnetics of Substances with Simultaneously Negative Values of $$ AND μ," *Soviet Physics Uspekhi*, vol. 10, no. 4, pp. 509–514, 1968. [Online]. Available: http://stacks.iop.org/0038-5670/10/i=4/a=R04?key=crossref.49e6b8a483029417bb518fd3889a3ed3

[47] S. Inasawa, M. Sugiyama, and Y. Yamaguchi, "Laser-induced shape transformation of gold nanoparticles below the melting point: The effect of surface melting," *Journal of Physical Chemistry B*, vol. 109, no. 8, pp. 3104–3111, 2005.

[48] W. Li, U. Guler, N. Kinsey, G. V. Naik, A. Boltasseva, J. Guan, V. M. Shalaev, and A. V. Kildishev, "Refractory Plasmonics with Titanium Nitride : Broadband Metamaterial Absorber," pp. 7959–7965, 2014.

[49] C. Clavero, "Plasmon-induced hot-electron generation at nanoparticle/metal-oxide interfaces for photovoltaic and photocatalytic devices," *Nature Photonics*, vol. 8, no. 2, pp. 95–103, 2014.

[50] S. Mukherjee, F. Libisch, N. Large, O. Neumann, L. V. Brown, J. Cheng, J. B. Lassiter, E. A. Carter, P. Nordlander, and N. J. Halas, "Hot electrons do the impossible: plasmon-induced dissociation of H2 on Au." *Nano letters*, vol. 13, no. 1, pp. 240–7, jan 2013. [Online]. Available: http://www.ncbi.nlm.nih.gov/pubmed/23194158

[51] A. Manjavacas, J. G. Liu, V. Kulkarni, and P. Nordlander, "Plasmon-induced hot carriers in metallic nanoparticles." *ACS nano*, vol. 8, no. 8, pp. 7630–8, aug 2014. [Online]. Available: http://www.ncbi.nlm.nih.gov/pubmed/24960573

[52] S. Ishii, S. L. Shinde, W. Jevasuwan, N. Fukata, and T. Nagao, "Hot Electron Excitation from Titanium Nitride Using Visible Light," pp. 3–8, 2016.

[53] H. Xia, X. Wen, Y. Feng, R. Patterson, S. Chung, N. Gupta, S. Shrestha, and G. Conibeer, "Hot carrier dynamics in HfN and ZrN measured by transient absorption spectroscopy," *Solar Energy Materials and Solar Cells*, vol. 150, pp. 51–56, 2016. [Online]. Available: http://dx.doi.org/10.1016/j.solmat.2016.01.026

[54] U. Guler, J. C. Ndukaife, G. V. Naik, A. G. A. Nnanna, A. V. Kildishev, V. M. Shalaev, and A. Boltasseva, "Local Heating with Lithographically Fabricated Plasmonic Titanium Nitride Nanoparticles," 2013.

[55] H. O. Pierson, *Handbook of Refractory Carbides and Nitrides*, 1st ed. Westwood, NJ: Noyes Publications, 1996. [Online]. Available: http://www.sciencedirect.com/science/article/pii/B9780815513926500027{%}5Cnhttp://linkinghub.elsevier.com/retrieve/pii/B9780815513926500027

[56] G. Naik, J. L. Schroeder, X. Ni, A. V. Kildishev, T. D. Sands, and A. Boltasseva, "Titanium nitride as a plasmonic material for visible and near-infrared wavelengths," *Optical Materials Express*, vol. 2, no. 4, p. 478, nov 2012. [Online]. Available: https://www.osapublishing.org/ome/fulltext.cfm?uri=ome-2-4-478{&}id=231559

[57] P. Patsalas, N. Kalfagiannis, and S. Kassavetis, "Optical properties and plasmonic performance of titanium nitride," *Materials*, vol. 8, no. 6, pp. 3128–3154, 2015.

[58] S. Logothetidis, I. Alexandrou, and A. Papadopoulos, "In situ spectroscopic ellipsometry to monitor the process of TiN _x thin films deposited by reactive sputtering," *Journal of Applied Physics*, vol. 77, no. 3, pp. 1043–1047, 1995. [Online]. Available: http://aip.scitation.org/doi/10.1063/1.358963

[59] P. Statham, "Limitations to accuracy in extracting characteristic line intensities from x-ray spectra," *Journal of Research of the National Institute of Standards and Technology*, vol. 107, no. 6, p. 531, 2002.

[60] A. Neckel, P. Rastl, R. Eibler, P. Weinberger, and K. Schwarz, "Results of self-consistent band-structure calculations for ScN, ScO, TiC, TiN, TiO, VC, VN and VO," *Journal of Physics C: Solid State Physics*, vol. 9, no. 4, pp. 579–592, 1975.

[61] J. S. Chawla, X. Y. Zhang, and D. Gall, "Effective electron mean free path in TiN(001)," *Journal of Applied Physics*, vol. 113, no. 6, 2013.

[62] A. B. Mei, "Lattice Dynamics and Electron/Phonon Interactions in Epitaxial Transition-Metal Nitrides," Doctoral, University of Illinois at Urbana-Champaign, 2015.

[63] P. Patsalas, C. Charitidis, S. Logothetidis, C. A. Dimitriadis, and O. Valassiades, "Combined electrical and mechanical properties of titanium nitride thin films as metallization materials," *Journal of Applied Physics*, vol. 86, no. 9, pp. 5296–5298, 1999.

[64] J. Cutnell and K. Johnson, *Physics*, ser. Physics. Wiley, 1998, no. v. 1. [Online]. Available: https://books.google.com/books?id=x6zvAAAAMAAJ

[65] S. Anisimov, B. Kapeliovich, and T. Perel-man, "Electron emission from metal surfaces exposed to ultrashort laser pulses," *Journal of Experimental and Theoretical Physics*, vol. 66, pp. 375–377, 1974.

[66] Y. Zhang, D. Y. Tzou, and J. K. Chen, "Micro- and Nanoscale Heat Transfer in Femtosecond Laser Processing of Metals," in *High-Power and Femtosecond Lasers: Properties, Materials and Applications*, P. Barret and M. Palmerm, Eds. Hauppauge, NY: Nova Science Publishers, 2009, ch. 5, pp. 159–206.

[67] W. M. Ibrahim, H. E. Elsayed-Ali, C. E. Bonner, and M. Shinn, "Ultrafast investigation of electron dynamics in multi-layer metals," *International Journal of Heat and Mass Transfer*, vol. 47, no. 10-11, pp. 2261–2268, 2004.

[68] J. Shackelford, Y.-H. Han, S. Kim, and S.-H. Kwon, *Materials Science and Engineering Handbook*. Boca Raton, FL: CRC Press, 2015.

[69] V. A. Lovchinov, H. Mädge, and N. A. Christensen, "Low Temperature Specific Heat of TiNx," *Physica Scripta*, vol. 25, pp. 649–650, 1982.

[70] D. Gray, New York.

[71] N. I. of Standards and Technology, *NIST Chemistry WebBook, SRD69*. U.S. Department of Commerce.

[72] S. D. Brorson, A. Kazeroonian, J. S. Moodera, D. W. Face, T. K. Cheng, E. P. Ippen, M. S. Dresselhaus, and G. Dresselhaus, "Femtosecond room-temperature measurement of the electron-phonon coupling constant in metallic superconductors," *Physical Review Letters*, vol. 64, no. 18, pp. 2172–2175, 1990.

[73] P. B. Allen, "The electron-phonon coupling constant," in *Handbook of Superconductivity*, C. Poole, Ed. New York: Academic Press, 2000, pp. 478–483.

[74] L. Toth, C. Wang, and C. Yen, "Superconducting critical temperature of nonstoichiometric transition metal carbides and nitrides," *Journal of Chemical Information and Modeling*, vol. 53, p. 160, 1989.

[75] P. B. Allen, "Theory of thermal relaxation of electrons in metals," *Physical Review Letters*, vol. 59, no. 13, pp. 1460–1463, 1987.

[76] W. L. McMillan, "Transition temperature of strong-coupled superconductors," *Physical Review*, vol. 167, no. 2, pp. 331–344, 1968.

[77] W. Spengler, R. Kaiser, A. Christensen, and G. Muller-Vogt, "Raman scattering, superconductivity, and phonon density of states of stoichiometric and nonstoichiometric TiN," *Phys. Rev. B*, vol. 17, no. 3, pp. 1095–1101, 1978.

[78] P. Roedhammer, W. Weber, E. Gmelin, and K. H. Rieder, "Low temperature specific heat and phonon anomalies in transition metal compounds," vol. 581, 1976.

[79] B. Altintas, "On the high pressure superconductivity of transition metal nitride: TiN," *Physica C: Superconductivity and its Applications*, vol. 487, pp. 37–41, 2013. [Online]. Available: http://dx.doi.org/10.1016/j.physc.2013.02.008

[80] E. I. Isaev, S. I. Simak, I. A. Abrikosov, R. Ahuja, Y. K. Vekilov, M. I. Katsnelson, and A. I. Lichtenstein, "Phonon related properties of transition metals , their carbides , and nitrides : A first- principles study Phonon related properties of transition metals , their carbides , and nitrides : A first-principles study," *Journal of Applied Physics*, vol. 123519, no. 2007, 2011.

[81] R. M. Costescu, M. A. Wall, and D. G. Cahill, "Thermal conductance of epitaxial interfaces," *Physical Review B - Condensed Matter and Materials Physics*, vol. 67, no. 5, pp. 1–5, 2003.

[82] H. K. Lyeo and D. G. Cahill, "Thermal conductance of interfaces between highly dissimilar materials," *Physical Review B - Condensed Matter and Materials Physics*, vol. 73, no. 14, pp. 1–6, 2006.

[83] J. M. Stern, J. Stanfield, W. Kabbani, J. T. Hsieh, and J. A. Cadeddu, "Selective prostate cancer thermal ablation with laser activated gold nanoshells," *Journal of Urology*, vol. 179, no. 2, pp. 748–753, 2008.

[84] DOE, "Energy Savings Forecast of Solid-State Lighting in General Illumination Applications," Tech. Rep. September, 2014.

[85] "Blue light has a dark side," 2018. [Online]. Available: https://www.health.harvard.edu/staying-healthy/blue-light-has-a-dark-side

[86] S. Zhao, H. P. Nguyen, M. G. Kibria, and Z. Mi, "III-Nitride nanowire optoelectronics," *Progress in Quantum Electronics*, vol. 44, pp. 14–68, 2015. [Online]. Available: http://dx.doi.org/10.1016/j.pquantelec.2015.11.001

[87] W. Guo, A. Banerjee, P. Bhattacharya, and B. S. Ooi, "InGaN/GaN disk-in-nanowire white light emitting diodes on (001) silicon," *Applied Physics Letters*, vol. 98, no. 19, pp. 1–4, 2011.

[88] S. M. Sadaf, Y.-H. Ra, H. P. T. Nguyen, M. Djavid, and Z. Mi, "Alternating-Current InGaN/GaN Tunnel Junction Nanowire White- Light Emitting Diodes," *Nano Letters*, no. 15, p. 66966701, 2015.

[89] H. Sekiguchi, K. Kishino, and A. Kikuchi, "Emission color control from blue to red with nanocolumn diameter of InGaN/GaN nanocolumn arrays grown on same substrate," *Applied Physics Letters*, vol. 96, no. 23, pp. 96–99, 2010.

[90] Q. Wang, C. Zhu, Y. Zhou, X. Wang, B. Liu, X. Wang, Y. Lv, Z. Feng, X. Xu, and Z. Ji, "Fabrication and photoluminescence of strong phase-separated InGaN based nanopillar LEDs," *Superlattices and Microstructures*, vol. 88, pp. 323–329, 2015. [Online]. Available: http://dx.doi.org/10.1016/j.spmi.2015.09.028

[91] C. Hums, T. Finger, T. Hempel, J. Christen, A. Dadgar, A. Hoffmann, and A. Krost, "Fabry-Perot effects in InGaNGaN heterostructures on Si-substrate," *Journal of Applied Physics*, vol. 101, no. 3, pp. 3–6, 2007.

[92] M. Vallone, M. Goano, F. Bertazzi, and G. Ghione, "Carrier capture in InGaN/GaN quantum wells: Role of electron-electron scattering," *Journal of Applied Physics*, vol. 121, no. 12, 2017.

[93] J. Singh, *Electronic and optoelectronic properties of semiconductor structures*, 2003. [Online]. Available: http://books.google.com/books?hl=en{&}lr={&}id=7n2CTG0m0{_}EC{&}oi=fnd{&}pg=PR1{&}dq=Electronic+and+Optoelectronic+Properties+of+Semiconductor+Structures{&}ots=lo0U48ht0X{&}sig=XzbGotn1lX77265Clh3tozmxj20

[94] J. Wang, K. W. Kim, and M. A. Littlejohn, "Carrier capture in pseudomorphically strained wurtzite GaN quantum-well lasers," *Applied Physics Letters*, vol. 71, no. 6, 1997.

[95] K. Kalna and M. Mosko, "Electron Capture into Quantum Wells via Scattering by Electrons, Holes, and Optical Phonons," vol. 54, no. 24, p. 10, 1996. [Online]. Available: http://arxiv.org/abs/cond-mat/9610110

[96] A. David, C. A. Hurni, N. G. Young, and M. D. Craven, "Carrier dynamics and Coulomb-enhanced capture in III-nitride quantum heterostructures," *Applied Physics Letters*, vol. 109, no. 3, 2016.

[97] Ü. Özgür, M. J. Bergmann, H. C. Casey, H. O. Everitt, A. C. Abare, S. Keller, and S. P. Denbaars, "Ultrafast optical characterization of carrier capture times in In x Ga 1 À x N multiple quantum wells," *Applied Physics Letters*, vol. 109, no. 2000, pp. 1–4, 2000.

[98] C.-K. Sun, F. Vallee, S. Keller, J. E. Bowers, and S. P. DenBaars, "Femtosecond studies of carrier dynamics in InGaN," *Applied Physics Letters*, vol. 70, no. 15, p. 2004, 1997. [Online]. Available: http://scitation.aip.org/content/aip/journal/apl/70/15/10.1063/1.118803

[99] K. T. Tsen, D. K. Ferry, A. Botchkarev, B. Sverdlov, A. Salvador, and H. Morkoç, "Direct measurements of electron-longitudinal optical phonon scattering rates in wurtzite GaN," *Applied Physics Letters*, vol. 71, no. 13, pp. 1852–1853, 1997.

[100] M. Takeshima, "Disorder-enhanced Auger recombination in 111-V alloys," *Journal of Applied Physics*, vol. 49, no. 12, 1978.

[101] H.-C. Wang, Y.-C. Lu, C.-Y. Chen, F.-Y. Jen, and C. C. Yang, "Ultrafast carrier dynamics in nano-clustered InGaN," in *SPIE*, K.-T. Tsen, J.-J. Song, and H. Jiang, Eds., vol. 6118, feb 2006, pp. 61 180B–61 180B–8. [Online]. Available: http://proceedings.spiedigitallibrary.org/proceeding.aspx?articleid=1275025

[102] C. M. Jones, C.-h. Teng, Q. Yan, P.-c. Ku, and E. Kioupakis, "Impact of Anderson localization on carrier recombination in InGaN quantum wells and the efficiency of nitride light-emitting diodes," *Applied Physics Letters*, vol. 113501, p. 1702.06009, 2017. [Online]. Available: https://aip.scitation.org/doi/full/10.1063/1.5002104

[103] K. Omae, Y. Kawakami, Y. Narukawa, and Y. Watanabe, "Nondegenerated Pump and Probe Spectroscopy in InGaN-Based Semiconductors," vol. 98, no. 1, pp. 93–98, 2002.

[104] L. Wang and X. Chen, "Experimental study on the chirp of the white-light continuum generation in Experimental study on the chirp of the white-light continuum generation in CaF 2 and sapphire," no. January, pp. 2–6, 2005.

[105] S. Yamaguchi and H.-o. Hamaguchi, "Convenient Method of Measuring the Chirp Structure of Femtosecond White-Light Continuum Pulses," vol. 49, no. 10, pp. 1513–1515, 1995.

[106] Y. Kawakami, K. Omae, A. Kaneta, K. Okamoto, Y. Narukawa, T. Mukai, and S. Fujita, "In inhomogeneity and emission characteristics of InGaN," *Journal of Physics: Condensed Matter*, vol. 13, pp. 6993–7010, 2001.

[107] C. Nelson, Y.-h. Ra, Z. Mi, and D. Steel, "Observation of Disorder State Coupling to Excitons in InGaN Disks in," 2017.

[108] E. Dekel, D. V. Regelman, D. Gershoni, E. Ehrenfreund, W. V. Schoenfeld, and P. M. Petroff, "Radiative lifetimes of single excitons in semiconductor quantum dots - manifestation of the spatial coherence effect," *Solid State Communications*, vol. 117, no. 7, pp. 395–400, 2001.

[109] G. E. Weng, W. R. Zhao, S. Q. Chen, H. Akiyama, Z. C. Li, J. P. Liu, and B. P. Zhang, "Strong localization effect and carrier relaxation dynamics in self-assembled InGaN quantum dots emitting in the green," *Nanoscale Research Letters*, vol. 10, no. 1, 2015.

[110] V. S. Bhadram, H. Liu, E. Xu, T. Li, V. B. Prakapenka, R. Hrubiak, S. Lany, and T. A. Strobel, "Semiconducting cubic titanium nitride in the Th3P4 structure," *Physical Review Materials*, vol. 2, no. 1, p. 011602, 2018. [Online]. Available: https://link.aps.org/doi/10.1103/PhysRevMaterials.2.011602